

# Investigations of the deep double donor magnesium in silicon

by

**Rohan Abraham**

M.Sc., Simon Fraser University, 2014

B.Sc., University of Victoria, 2012

Thesis Submitted in Partial Fulfillment of the  
Requirements for the Degree of  
Doctor of Philosophy

in the  
Department of Physics  
Faculty Science

© **Rohan Abraham 2019**  
**SIMON FRASER UNIVERSITY**  
**Spring 2019**

Copyright in this work rests with the author. Please ensure that any reproduction or re-use is done in accordance with the relevant national copyright legislation.

# Approval

**Name:** Rohan Abraham

**Degree:** Doctor of Philosophy (Physics)

**Title:** Investigations of the deep double donor magnesium in silicon

**Examining Committee:** **Chair:** Malcolm Kennett  
Associate Professor

**Michael Thewalt**  
Senior Supervisor  
Professor

**Stephanie Simmons**  
Supervisor  
Assistant Professor

**David Broun**  
Supervisor  
Associate Professor

**George Kirczenow**  
Internal Examiner  
Professor

**Ben Murdin**  
External Examiner  
Professor  
University of Surrey

**Date Defended:** January 28, 2019

# Abstract

The deep double donor levels of substitutional chalcogen impurities in silicon have unique optical properties which may enable a spin/photonic quantum technology. The interstitial magnesium impurity in silicon is also a deep double donor but has not yet been studied in the same detail as have the chalcogens. In this study we look at the neutral and singly ionized  $Mg_i$  absorption spectra in natural silicon and 28-silicon in more detail, looking in particular for the  $1s(A_1)$  to  $1s(T_2)$  transitions which are very strong for the chalcogens and are central to the proposed spin/photonic quantum technology. We further observe the presence of another donor ( $Mg_{i*}$ ) that may result from  $Mg_i$  in a reduced symmetry configuration, due to either complexing or the occupation of an interstitial site with symmetry lower than the usual tetrahedral site. The neutral species of  $Mg_{i*}$  reveal additional low lying ground state levels detected through temperature dependence studies. We also observe a new shallow donor which we identify as an Mg-B pair center. Additionally we present photoluminescence spectra that verify the existence of an Mg-Mg isoelectronic pair center through its isotopic fingerprint. We further include the results of a temperature dependence and photoluminescence lifetime study of this same center, revealing unusual behaviour of the main no-phonon line and associated phonon replicas.

**Keywords:** Simon Fraser University

# Acknowledgements

This work was supported by the Natural Sciences and Engineering Research Council of Canada (NSERC). This work has been partly supported by the Russian Foundation for Basic Research (RFBR Project No. 18-502-12077-DFG) and of the Deutsche Forschungsgemeinschaft (DFG No. 389056032). The  $^{28}\text{Si}$  samples used in this study were prepared from Avo28 crystal produced by the International Avogadro Coordination (IAC) Project (2004-2011) in cooperation among the BIPM, the INRIM (Italy), the IRMM (EU), the NMIA (Australia), the NMIJ (Japan), the NPL (UK), and the PTB (Germany).

Thank you to all members of the SQT research group at SFU, who have made the lab an informative and entertaining place to be for the last few years. These include Kevin Morse, Timothy Richards, Camille Bowness, Adam DeAbreu, Laurent Bergeron, Camille Chartrand, Alexander Kurkjian, Moein Kazemi, and Daniel Higginbottom. Thank you to my supervisors Dr. Michael Thewalt and Dr. Stephanie Simmons for their instruction and guidance throughout this project. Thanks to Nathan Smith for helpful discussions about physical applications of group theory. Thank you to my family for always being available and supportive. I hereby (unofficially) dub this thesis *The Spectronomicon*.

*“They don’t think it be like it is, but it do.”- Oscar Gamble*

# Contents

<b>Approval</b>	<b>ii</b>
<b>Abstract</b>	<b>iii</b>
<b>Acknowledgements</b>	<b>iv</b>
<b>Table of Contents</b>	<b>v</b>
<b>List of Tables</b>	<b>vii</b>
<b>List of Figures</b>	<b>viii</b>
<b>1 Introduction and background</b>	<b>1</b>
<b>2 Theory and Background</b>	<b>6</b>
2.1 Silicon . . . . .	6
2.2 Optical absorption . . . . .	8
2.3 Effective mass theory and donors in silicon . . . . .	9
2.3.1 Double donors in silicon . . . . .	17
2.4 Donor bound excitons . . . . .	19
2.4.1 Hayne’s Rule . . . . .	21
2.4.2 Donor-acceptor pair (DAP) bands . . . . .	23
2.5 Isoelectronic bound excitons . . . . .	24
2.5.1 IBE ground state electronic structure . . . . .	25
2.5.2 Isotope shifts of no-phonon lines . . . . .	26
2.6 Spectral broadening mechanisms . . . . .	28
2.6.1 Isotope broadening . . . . .	29
2.6.2 Stark broadening . . . . .	30
2.6.3 Concentration broadening . . . . .	33
2.6.4 Broadening due to strain generated by point defects . . . . .	34
<b>3 Samples and apparatus</b>	<b>36</b>
3.1 Fourier transform infra-red (FTIR) spectroscopy . . . . .	36

3.2	Magnesium diffusion in silicon . . . . .	41
3.3	Absorption . . . . .	43
3.4	Photoluminescence/Raman . . . . .	45
<b>4</b>	<b>Absorption results</b>	<b>46</b>
4.1	$\text{Mg}_i^0$ and $\text{Mg}_i^+$ donor spectra . . . . .	48
4.2	$\text{Mg}_{i^*}^0$ and $\text{Mg}_{i^*}^+$ donor spectra . . . . .	57
4.3	Thermal effects . . . . .	65
4.3.1	Anneal and Quench . . . . .	65
4.3.2	Thermalization of $\text{Mg}_{i^*}^0$ levels . . . . .	65
4.4	Mg-B shallow donor complex . . . . .	69
<b>5</b>	<b>Emission results</b>	<b>74</b>
5.1	Raman/donor-acceptor pair band . . . . .	74
5.2	Isoelectronic bound exciton . . . . .	76
5.3	IBE temperature dependence and PL lifetime . . . . .	78
5.4	Future work . . . . .	87
<b>6</b>	<b>Conclusions</b>	<b>89</b>
	<b>Bibliography</b>	<b>91</b>
	<b>Appendix A Relevant group theory</b>	<b>101</b>
A.1	Background . . . . .	101
A.2	Matrix representations . . . . .	105
A.3	Dipole allowed/forbidden transitions in $T_d$ . . . . .	107
A.3.1	From $A_1$ . . . . .	108
A.3.2	From $A_2$ . . . . .	108
A.3.3	From E . . . . .	108
A.3.4	From $T_1$ . . . . .	108
A.3.5	From $T_2$ . . . . .	108
A.4	Raman allowed/forbidden transitions in $T_d$ . . . . .	108
A.4.1	From $A_1$ . . . . .	109
A.4.2	From $A_2$ . . . . .	109
A.4.3	From E . . . . .	109
A.4.4	From $T_1$ . . . . .	109
A.4.5	From $T_2$ . . . . .	109
	<b>Appendix B Structure of hydrogenic orbitals</b>	<b>111</b>

# List of Tables

Table 2.1	Binding energies of 1s levels associated with neutral and singly ionized states of deep double donors. . . . .	18
Table 4.1	Peak spacings between $2p_0$ and higher excited states for $Mg_i^+$ and $Mg_i^0$ species in $^{28}Si$ . . . . .	56
Table 4.2	Observed and EMT predicted binding energies for transitions in $Mg_i^0$ and $Mg_i^+$ spectra in $^{28}Si$ . . . . .	56
Table 4.3	Peak positions of $Mg_i^0/Mg_{i*}^0$ transitions in $^{nat}Si$ and $^{28}Si$ . . . . .	60
Table 4.4	Parameters for mixed Gaussian-Lorentzian fits applied to $2p_0$ and $2p_{\pm}$ features in $Mg_i$ and $Mg_{i*}$ . . . . .	61
Table 4.5	Peak positions of $Mg_i^+/Mg_{i*}^+$ transitions in $^{nat}Si$ and $^{28}Si$ . . . . .	64
Table 4.6	Peak positions detailing fine structure of the thermally activated transitions labelled “1”, “3” and “5” arising from low lying excited states in $Mg_{i*}^0$ . . . . .	69
Table 4.7	Energies of donor transitions observed in the shallow donor region seen in Fig. 4.15. . . . .	71
Table 4.8	Ground state ionization energies and bound exciton localization energies of group-V shallow donors and Mg-B. . . . .	73
Table 5.1	Observed and predicted relative integrated intensities and energies for peaks corresponding to Mg-Mg pairs. . . . .	77
Table 5.2	Energy shifts below the $Mg_{NP}$ line of luminescence features believed to be related to the Mg-pair IBE. . . . .	80
Table 5.3	Values of $t_1$ and $t_2$ associated with the photoluminescence lifetime of the Mg-pair IBE. . . . .	85

# List of Figures

Figure 2.1	Constant energy surfaces. . . . .	7
Figure 2.2	Silicon lattice structure. . . . .	11
Figure 2.3	Wavefunction structure. . . . .	12
Figure 2.4	Silicon band-gap structure. . . . .	15
Figure 2.5	Donor and acceptor bound excitons. . . . .	20
Figure 2.6	Donor and acceptor-like isoelectronic bound excitons. . . . .	25
Figure 2.7	Stark shift as a function of ionized impurity concentration for $2p_0$ and $2p_{\pm}$ . . . . .	33
Figure 3.1	FTIR apparatus schematic. . . . .	37
Figure 3.2	Magnesium diffusion in silicon. . . . .	43
Figure 3.3	Impact of above band-gap illumination on shallow donor spectra. . . . .	44
Figure 4.1	Mixed Gaussian-Lorentzian line profiles. . . . .	48
Figure 4.2	$Mg_i^0$ spectra. . . . .	49
Figure 4.3	$Mg_i^+$ spectra. . . . .	51
Figure 4.4	Valley orientations of $p_{\pm}$ -states. . . . .	52
Figure 4.5	High excited states of $Mg_i^0$ and $Mg_i^+$ . . . . .	53
Figure 4.6	Overview of $Mg_i^+$ and $Mg_{i*}^+$ spectral regions. . . . .	54
Figure 4.7	Impact of isotopic effects in $^{nat}Si$ vs. $^{28}Si$ . . . . .	55
Figure 4.8	$Mg_{i*}^0$ spectra. . . . .	58
Figure 4.9	Structure of $2p_0$ in $Mg_i^0$ and $Mg_{i*}^0$ . . . . .	59
Figure 4.10	$Mg_{i*}^+$ spectra. . . . .	62
Figure 4.11	Structure of $2p_{\pm}$ in $Mg_i^+$ and $Mg_{i*}^+$ . . . . .	63
Figure 4.12	Spectra of $Mg_{i*}$ regions before and after anneal and quench procedure. . . . .	66
Figure 4.13	Low lying excited state structure in $Mg_{i*}^0$ . . . . .	67
Figure 4.14	Arrhenius relation associated with thermal activation to low lying excited states in $Mg_{i*}^0$ . . . . .	68
Figure 4.15	Shallow donor absorption spectra. . . . .	70
Figure 4.16	Structure of $2p_0$ in Mg-B. . . . .	71
Figure 4.17	Photoluminescence spectrum of $^{28}Si$ HB Mg-diffused sample. . . . .	72
Figure 4.18	Haynes' Rule. . . . .	73

Figure 5.1	Raman spectra for HB and LB $^{28}\text{Si}$ samples. . . . .	76
Figure 5.2	Isotopic fingerprint of the magnesium isoelectronic pair center. . . .	78
Figure 5.3	Waterfall plot and integrated intensities revealing temperature dependence of Mg-pair IBE. . . . .	80
Figure 5.4	Sample PL spectra showing temperature dependence of main Mg-pair IBE and nearby satellites. . . . .	81
Figure 5.5	Photoluminescence spectra revealing Mg-pair related features with similar temperature dependence to the main NP line of the IBE. . .	82
Figure 5.6	Shift of the main NP line of the IBE as a function of temperature.	83
Figure 5.7	Boron and lithium TO phonon replica and free-exciton (FE) temperature dependence. . . . .	84
Figure 5.8	Photoluminescence lifetime measurement sequence. . . . .	84
Figure 5.9	Photoluminescence lifetime of the Mg-pair IBE as a function of temperature. . . . .	85
Figure 5.10	Example data from photoluminescence lifetime studies in the two primary temperature regimes of the Mg-pair IBE. . . . .	86
Figure 5.11	Possible IBE triplet feature with similar temperature dependence to the Mg-pair IBE. . . . .	88

# Chapter 1

## Introduction and background

In this thesis I present work discussed in detail in recent publications by our research group that discuss the deep double donor impurity magnesium in silicon [1, 2]. A recent proposal by Morse *et al.* suggested the use of chalcogen deep double donors, such as selenium (Se) in silicon (Si), as the basis for a scalable qubit-photonic cavity technology [91]. Unlike the chalcogens, the Group-II impurity Magnesium is an interstitial ( $\text{Mg}_i$ ) rather than substitutional ( $\text{Mg}_s$ ) [39, 59] defect. Like them however, magnesium is a helium-like deep double donor in silicon, with two excess electrons relative to Si when occupying the interstitial site, as it predominantly does. Instead of replacing a silicon atom magnesium tends to sit in an interstitial position of equivalent symmetry to the substitutional sites, referred to the tetrahedral interstitial site, with four nearest neighbor Si atoms. Within Group-II this is unusual, with other impurities of that group, such as beryllium, forming substitutional double acceptors in silicon [19, 107, 27], although there is evidence that some magnesium may indeed become substitutional and act as a double acceptor [10]. Since magnesium is primarily incorporated into Si as an interstitial defect, the most relevant feature about its position in the periodic table is that it lies two atomic numbers from the filled shell of neon. When positioned interstitially, its two extra valence electrons relative to neon are not covalently bonded to anything. These valence electrons are then free to be compensated or not by the presence of acceptor species, giving rise to singly ionized and neutral charge states. Many absorption features of interstitial magnesium's neutral ( $\text{Mg}_i^0$ ) and ionized ( $\text{Mg}_i^+$ ) species have been uncovered in past investigations [39, 59, 58, 56, 57, 60, 61], although transitions from the  $1s(A_1)$  ground state to s-like excited states, which are quite strong for the chalcogens [43, 91] and central to their potential use as qubits, have never been observed for  $\text{Mg}_i$ . In selenium, the ground state  $1s(A_1)$  to first excited state  $1s(T_2)$ , is a doublet thanks to the strong zero-field hyperfine interaction in Se that splits the ground state into singlet and triplet levels [91].

Early optical and electrical studies of Mg-diffused Si established  $\text{Mg}_i$  as a double donor impurity [39]. The detailed absorption studies of Ho and Ramdas [59] established the tetrahedral interstitial site for both  $\text{Mg}_i^0$  and  $\text{Mg}_i^+$  through the piezospectroscopic effect, i.e.

the shifting of spectral features through application of uniaxial strains. They determined ionization energies of 107.50 and 256.47 meV for the neutral and singly ionized species respectively. In piezospectroscopic experiments, the conduction band minima of silicon are shifted relative to one another depending on the axis along which a stress is applied, leading to a reduction in symmetry and a corresponding splitting of spectral lines. The authors predicted and observed splitting consistent with an assignment of tetrahedral ( $T_d$ ) symmetry for interstitial magnesium. For instance, no splitting was observed with a uniaxial force applied along the  $\langle 111 \rangle$  crystal axis. For a  $T_d$  impurity such a perturbation would shift all the conduction band minima of silicon equally, giving no overall change in symmetry and therefore no additional splitting. Ho and Ramdas were also the first to comment on the absence of any visible  $1s(A_1)$  to  $1s(T_2)$  absorption for either  $Mg_i^0$  or  $Mg_i^+$ , and to identify a doublet splitting of the  $2p_{\pm}$  transition for  $Mg_i^+$  as resulting from a central-cell effect, i.e. wavefunction overlap of these excited states with the donor impurity potential.

In work by Pajot *et al.* [100] the authors made note of a center in Mg-diffused silicon and speculated that it might represent either a Mg-B or Mg-O pair. This center appearing as a single donor, seemed to have an ionization energy somewhat less than that of phosphorus. Later, in an electrical and optical study of Mg-diffused Si, Lin [86] detected a number of donor levels besides those of  $Mg_i^0$  and  $Mg_i^+$ , with ionization energies of 40, 55, 80, and 93 meV. They also made the prescient suggestions that some of these unidentified species could result from complexes of Mg with other rapidly diffusing impurities, such as transition metals, introduced during the Mg diffusion process, or from Mg in an interstitial site other than  $T_d$ . An earlier EPR study of Mg-diffused silicon by Baxter and Ascarelli had proposed that Mg might be photoconverted from the normal interstitial  $T_d$  site to a different interstitial site such as  $C_{3v}$  [15]. A study using photothermal ionization spectroscopy found the same unidentified donor species with ionization energies of 55 and 93 meV, in addition to  $Mg_i^0$  and  $Mg_i^+$  [79]. Baxter and Ascarelli's EPR paper suggested that only a few milliwatts of IR laser power should be necessary to photoionize  $T_d$  interstitial  $Mg_i^+$  impurities to  $Mg_i^{++}$  wherein they would be free to inhabit either the  $T_d$  or  $C_{3v}$  interstitial site. Recapture of the photoionized electrons would then lead to  $Mg_i^+$  in either site with those interstitials inhabiting the  $C_{3v}$  position having a decay rate back to the  $T_d$  configuration characterized by second order kinetics [15]. Calculations by Weiser [137] demonstrated that the probability of occupying one site or the other depends strongly on the size of the impurity, with  $C_{3v}$  having a slightly smaller volume than  $T_d$ . Baxter and Ascarelli [15] speculate that  $Mg_i^+$  has a 'critical' ionic radius that makes occupation of either site possible. Their data further suggested a rapid increase in the rate of decay from  $C_{3v}$  to  $T_d$  above 14 K, offering a testable parameter in our observation of these features.

The symmetry of most substitutional and interstitial defects in Si corresponds to the tetrahedral, or  $T_d$ , point group. This has a set of allowed symmetry operations, detailed in the appendices, that conserve the symmetry of the system Hamiltonian for defects in

Si. Subject to this symmetry, the electronic states of these defects can be described in terms of the symmetry representations of the  $T_d$  group, of which there are five:  $A_1$ ,  $A_2$ ,  $E$ ,  $T_1$ , and  $T_2$ . For  $T_d$  symmetry, the  $2p_{\pm}$  excited state for instance has the representation  $2T_1+2T_2$ . Transitions from  $1s(A_1)$  to  $T_2$  states are dipole-allowed, while those to  $T_1$  levels are forbidden [59]. Zeeman studies of  $Mg_i^+$  excited states, in particular of the  $p_{\pm}$  levels, were performed by Thilderkvist *et al.* [129]. Their results allowed a discussion of the nature of splitting into doublets observed most strongly for the  $2p_{\pm}$  level. They attributed this to central cell splitting of  $p_{\pm}$  levels and further discussed the relative intensities of the doublet components as a function of their valley composition. This central cell interaction is caused by some non-zero overlap of the p-state wavefunctions with the donor impurity. While not as significant an overlap as the ground state wavefunction, which has a maximum at the origin, this interaction is significant enough to lift degeneracy between the two degenerate triplet levels with  $T_2$  symmetry, to which transitions are allowed from the  $A_1$  ground state.

Later studies undertaken by the Ho group [58, 56, 57, 60, 61] have included observations of a wider range of excited states for  $Mg_i^0$  and  $Mg_i^+$ , resulting in estimates of the ionization energies of  $Mg_i^0$  and  $Mg_i^+$  of 107.50 meV and 256.49 meV, respectively, in good agreement with those of Ho and Ramdas [59]. They also observed a small splitting of the  $3p_{\pm}$  line, and ascribed it to a central cell splitting, as for  $2p_{\pm}$  [58]. These authors also demonstrated that weak absorption lines observed in some of the earlier studies resulted from the neutral and singly ionized charge states of a double donor resulting from a  $Mg_i$ -O complex, with ionization energies of 124.66 and 274.90 meV, respectively [56, 57]. The formation of such complexes is a familiar theme for rapidly diffusing interstitial species. The  $Mg_i$ -O double donor for instance has similarities to the  $Li_i$ -O shallow donor which, as for the  $Mg_i$  case, has a larger ionization energy than does the isolated interstitial Li shallow donor [101].

A number of previously reported, relatively weak donor-like absorption transitions lying just below the dominant  $Mg_i^0$  and  $Mg_i^+$  features are a particular focus of this study. Lin [86] first reported a series of features interpreted as the  $2p_0$ ,  $2p_{\pm}$ ,  $3p_0$ ,  $3p_{\pm}$  and  $4p_{\pm}$  transitions of a shallow donor they labelled  $X_4$ , with ionization energy  $\sim 93$  meV. Ho [57, 61] further studied this center, labelling the  $2p_0$ ,  $2p_{\pm}$ , and  $3p_{\pm}$  transitions as lines “1”, “3” and “5” and determining an ionization energy of 93.57 meV. Ho [57, 61] also reported the  $2p_0$ ,  $2p_{\pm}$ , and  $3p_{\pm}$  of what was interpreted as a different shallow donor with an ionization energy 94.36 meV. These were labelled lines “2”, “4”, and “6”. Ho [61] further reported a doublet absorption feature labelled line “a”, and a singlet labelled line “b”, which were interpreted as the  $2p_{\pm}$  and  $3p_{\pm}$  transitions of an unknown singly-ionized double donor with ionization energy 213.53 meV.

We will retain the “1” through “6” and “a” and “b” labels for these transitions, but will instead show that they all arise from the neutral and singly ionized states of a single perturbed  $Mg_i$  donor with symmetry reduced below  $T_d$ . This is likely a consequence of either  $Mg_i$  inhabiting an alternate interstitial site, as suggested by Baxter and Ascarelli, [15] or

Mg<sub>i</sub> complexing with other species. We denote these centers as Mg<sub>i\*</sub><sup>0</sup> (including lines “1”-“6”) and Mg<sub>i\*</sub><sup>+</sup> (including lines “a” and “b”) for the neutral and singly-ionized charged states of the double donor. We will show that Mg<sub>i\*</sub><sup>0</sup> is unusual in that even though the ground state binding energy is larger than that of normal shallow donors, it has very low-lying excited state components which can be thermally populated at relatively low temperatures. As will be detailed later, this gives rise to lines “1”, “3”, and “5”. For normal shallow donors having T<sub>d</sub> symmetry, the 1s(A<sub>1</sub>) singlet ground state is much further separated from the 1s(E) and 1s(T<sub>2</sub>) valley-orbit excited states.

Given the large number of as yet unidentified absorption transitions reported in Mg-diffused Si, one of the goals of this study was to identify species which were intrinsic to Mg<sub>i</sub>, and not complexes with other impurities. This was achieved by using well-characterized, high purity, float-zone Si starting material, and high purity Mg as the diffusion source. As a result, absorption from Mg-O complexes [56, 57] was either unobservable or very weak. A second goal was to investigate the possible spectral linewidth improvements in isotopically enriched 28-silicon (<sup>28</sup>Si), which, by eliminating inhomogeneous isotope broadening, produces remarkable improvements in linewidth for some transitions of both shallow donors and deep chalcogen donors [91, 72, 18, 117, 116]. The final goal was to search for the as yet undetected 1s(A<sub>1</sub>) to 1s(T<sub>2</sub>) absorption transition, which is forbidden under the effective mass approximation, but symmetry allowed, and very strong for the deep chalcogen double donors.

No evidence for the 1s(A<sub>1</sub>) to 1s(T<sub>2</sub>) absorption transition could be observed for either Mg<sub>i</sub><sup>0</sup> or Mg<sub>i</sub><sup>+</sup>, but the expected location for these transitions suffers from overlap with other relatively strong spectral features. Attempts to observe the 1s(A<sub>1</sub>) to 1s(E) transition for either charge state of Mg<sub>i</sub> using electronic Raman scattering were also unsuccessful. The Mg<sub>i\*</sub> counterparts of Mg<sub>i</sub> likewise revealed no sign of the s-like excited states in their absorption spectra. Some spectral lines revealed small energy shifts and linewidth improvements in <sup>28</sup>Si, although not as dramatic as that seen for shallow impurities or the deep chalcogen double donors.

Even though our goal was to investigate transitions intrinsic to Mg<sub>i</sub> impurities, the acceptor boron (B) is an omnipresent impurity in silicon, and higher B concentrations were intentionally used to create higher concentrations of Mg<sub>i</sub><sup>+</sup>. This resulted in the discovery of absorption related to a new shallow donor impurity which we ascribe to an interstitial magnesium-substitutional boron pair. Like many shallow donors, this new Mg<sub>i</sub>-B<sub>s</sub> shallow donor can bind Coulomb-coupled electron hole pairs called excitons and this is observed in the photoluminescence spectra of these samples. In these spectra the donor binding energy and exciton localization energy are found to follow Hayne’s Rule [49] for Si, a semi-empirical formula predicting a linear relationship between the two quantities.

Deep-level transient spectroscopy (DLTS) performed by Baber *et al.* on Mg diffused samples [10] suggests that magnesium may also incorporate substitutionally as a double

acceptor  $\text{Mg}_s$ , as one might expect given its position two periodic groups behind silicon. In DLTS, the sample region consists of a reverse biased  $p - n$  diode with impurities located in the depletion zone. A voltage pulse that shifts towards a forward bias allows charges to penetrate the depletion zone and be captured by charge carriers. After the pulse the system returns to steady state and defects become ionized again in a temperature dependent way. Ionization of defects changes the charge density of the depletion region resulting in a change in capacitance that is detected by DLTS equipment, such as the apparatus proposed by Jansson *et al.* [67]. The work of Baber *et al.* showed hole-emission dominated by an acceptor level they assigned to the substitutional double acceptor species  $\text{Mg}_s$  [10]. An energy of  $E_v + 0.34 \text{ eV}$  for this level was inferred from their measurements.

The dual character of magnesium as a substitutional double acceptor and an interstitial double donor implies the potential for formation of an isoelectronic bound exciton (IBE) center comprised of an  $\text{Mg}_i\text{-Mg}_s$  pair. IBE centers are able to localize excitons much more tightly than shallow donor bound excitons such as those that occur for group V elements. In addition, thanks to their lack of Auger decay, a mechanism common in donor and acceptor bound excitons in which the energy of exciton recombination promotes the extra charge carrier to the conduction band (electron) or valence band (hole), these centers are in general very bright. This makes their identification by isotopic fingerprinting [117] relatively straightforward, and has generated interest in these centers as efficient near IR emitters [101]. Impurities of the same group as silicon such as carbon are not known to form IBEs as single impurities. Complexes of multiple impurities are however known to form these centers in silicon [117]. For instance, an analogous center to the possible  $\text{Mg}_i\text{-Mg}_s$  pair is known to form for beryllium with  $\langle 001 \rangle$  axially symmetric  $\text{Be}_i\text{-Be}_s$  pairs. This was first identified by Henry *et al.* [52, 53] at 1.077 eV along with associated phonon replicas through photoluminescence and Zeeman measurements. Observation of these features by Henry *et al.* confirmed the calculations of Tarnow *et al.* [126], which predicted the  $\langle 111 \rangle$  oriented  $\text{Be}_i\text{-Be}_s$  defect as the lowest energy configuration for such a pair. Tarnow *et al.* also accurately predicted the presence of a local mode replica of the main NP line at the energy observed by Henry *et al.* [53]. The photoluminescence results presented in this work follow the results of Steinman and Grimmeiss [120], who proposed that an  $\text{Mg}_i\text{-Mg}_s$  pair center might be responsible for a feature observed in PL at  $\sim 1.017 \text{ eV}$ . Here we confirm this assignment through high resolution scans seen in Fig. 5.2. These reveal five distinct peaks with integrated intensities matching those anticipated for an  $\text{Mg}_i\text{-Mg}_s$  pair center given three stable Mg isotopes (78.99(4)%  $^{24}\text{Mg}$ , 10.00(1)%  $^{25}\text{Mg}$  and 11.01(3)%  $^{26}\text{Mg}$ ) [50]. Further study of this center is included in the form of temperature dependence, photoluminescence and photoluminescence lifetime measurements that reveal unusual behaviour of the main no phonon line and associated local vibrational mode (LVM) and phonon replicas.

## Chapter 2

# Theory and Background

### 2.1 Silicon

In isotopically enriched 28-silicon ( $^{28}\text{Si}$ ), there are a number of advantages for spectroscopy over  $^{\text{nat}}\text{Si}$ .  $^{28}\text{Si}$  is a nuclear-spin free environment, providing an excellent platform in which to characterize and control impurity based qubits without a major source of decoherence. The presence of nuclear spins in  $^{\text{nat}}\text{Si}$  present a source of magnetic field inhomogeneity that limits coherence times in such systems. Also important in  $^{28}\text{Si}$  is the lack of isotopic broadening. The random placement of  $^{29}\text{Si}$  and  $^{30}\text{Si}$  isotopes in  $^{\text{nat}}\text{Si}$  result in broadened optical lines that often obscure fine structure. In this thesis the term fine structure is used to discuss a range of small spectroscopic splittings and should not be taken to imply a relationship to spin-orbit coupling. In this work we study Mg-diffused samples in both  $^{28}\text{Si}$  and  $^{\text{nat}}\text{Si}$ . Though in most of our Mg-related spectra we do not observe the dramatic difference in linewidths seen in some other deep donor systems [91, 43], there is in general more fine structure to be seen in  $^{28}\text{Si}$  samples.

We work primarily with float-zone (FZ) grown silicon as opposed to the Czochralski grown material more commonly used in industry. Czochralski silicon is relatively easy to manufacture and can yield large diameter wafers, however it suffers from higher concentrations of impurities such as carbon and especially oxygen. These can have significant broadening effects on spectral features that obscure fine structure. The FZ growth procedure purifies silicon by passing RF coils up the length of a polycrystalline Si rod, liquefying the sections covered by the coil. As the crystal re-solidifies following the RF coil passing by, it re-forms as a single crystal. Most impurities have a greater affinity for remaining in the liquid phase and are removed in this manner as the molten zone passes up the length of the rod. Common impurities like carbon, and oxygen among others are removed from the crystal to the desired extent by successive FZ passes. Boron, another common impurity, is difficult to remove by this method since it has a segregation coefficient near unity. The Avogadro project material, produced in an effort to redefine the kilogram in terms of a unit number of Si atoms [32], is purified by this process and is used to make many of our samples.

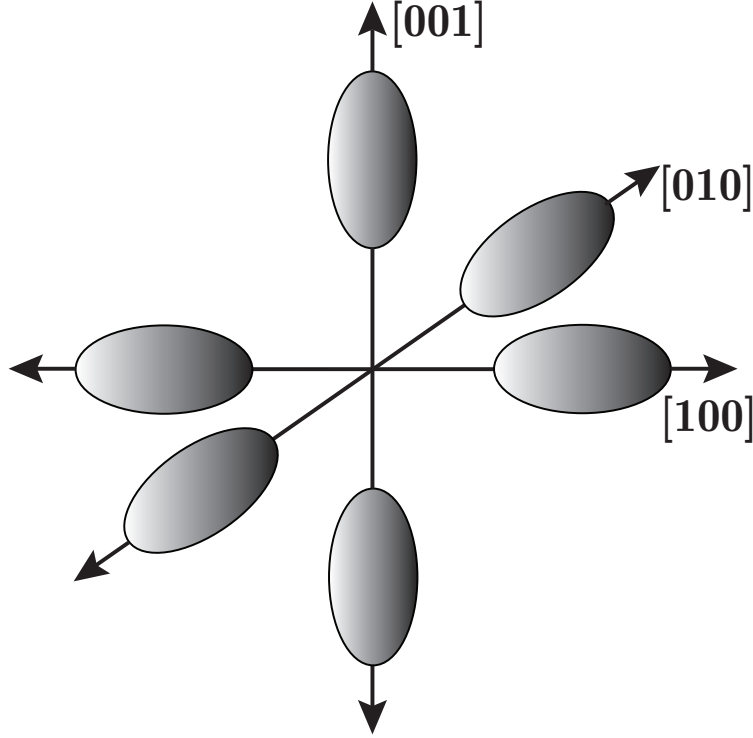


Figure 2.1: Here we see ellipsoids representing the constant energy surfaces near each of the six equivalent minima in the silicon conduction band.

The band structure of silicon includes six identical minima in the conduction band along the  $\langle 100 \rangle$  axis and equivalent directions. As silicon is an indirect band-gap semiconductor, these are separated in  $k$ -space from the corresponding valence band maxima which occur at  $k = 0$ , the Brillouin-zone center. The difference between the  $k = 0$  maxima and the conduction band minima is given by  $k_0 = 2\pi/a(0.85, 0, 0)$  for  $\langle 100 \rangle$  and equivalents for the other minima [127]. Wavefunctions of donor impurities, are constructed from a superposition of these six equivalent minima. Near the conduction band minima, constant energy surfaces are given by ellipsoids with long axes aligned with  $\langle 100 \rangle$  equivalent axes and centered at  $k_0$ , 85% of the way to the zone boundary from the Brillouin-zone center at  $k = 0$ . This gives rise to the multi-valley behaviour of deep donors in silicon discussed in the next section. If we consider the minima oriented along the  $z$  axis, we can describe the constant energy surfaces near the conduction band minima in terms of  $k$ -vector components as,

$$E = \frac{\hbar^2}{2} \left[ (k_z - k_0)^2/m_1 + (k_x^2 + k_y^2)/m_2 \right]. \quad (2.1)$$

Here the effective masses  $m_1$  and  $m_2$  are  $0.98m_0$  and  $0.19m_0$  in silicon respectively [33, 81], and the energy origin is taken to be at the conduction band minimum.

## 2.2 Optical absorption

In general, for a beam of light propagating along the  $x$  axis, absorption through a length of one of our silicon samples may be written as,

$$I(x) = I_0 \exp(-\alpha x), \quad (2.2)$$

with  $x$  the depth in cm to which light has passed through the sample,  $I(x)$  the intensity at depth  $x$ ,  $I_0$  the initial intensity of light incident on the sample, and  $\alpha$  the absorption coefficient in units of  $\text{cm}^{-1}$ . Most spectra in this work are presented in these absorption coefficient units. To convert a raw absorption spectrum, in which signal intensity depends on the amount of silicon passed through, to one in units of absorption coefficient, one simply applies the conversion,

$$\alpha = \frac{1}{L} \ln \left( \frac{I(L)}{I_0} \right), \quad (2.3)$$

with the spectrum of light passed through a sample of length  $L$  given as  $I(L)$ .

Hillborn [55] presents a discussion of optical absorption in a two level system in terms of Einstein coefficients describing rates of spontaneous emission  $W_{21}^s$ , induced emission  $W_{21}^i$ , and induced absorption  $W_{12}^i$ . These are written as,

$$W_{21}^s = A_{12}N_1, \quad W_{21}^i = B_{12}pN_2, \quad W_{12}^i = B_{21}pN_2. \quad (2.4)$$

Here  $N_1$  and  $N_2$  are the number of atoms in states 1 and 2, and  $p$  the energy density per unit angular frequency. The coefficients  $A_{12}$ ,  $B_{12}$ , and  $B_{21}$  are related via,

$$B_{21} = \frac{\pi^2 c^3}{\hbar \omega_{21}^3} A_{21}, \quad B_{21} = \frac{g_1}{g_2} B_{12}. \quad (2.5)$$

Here,  $g_1$  and  $g_2$  are the degeneracy of levels 1 and 2, and  $\omega_{21}$  is the frequency of the transition between the two levels. Derivations detailed by Corney and Ditchburn [26, 34] have shown that  $A_{12}$  may be written as,

$$A_{21} = \frac{2\omega_{21}^3 e^2}{3\epsilon_0 \hbar c^3} |\langle 1|r|2 \rangle|^2, \quad (2.6)$$

describing transitions between levels 1 and 2. For a non-degenerate two level system, the quantity,

$$\mu_{21}^2 = e^2 |\langle 1|r|2 \rangle|^2, \quad (2.7)$$

defines the transition dipole moment  $\mu_{21}$ , a measure of the probability of a transition occurring under illumination at frequency  $\omega_{21}$ . As discussed by Morse *et al.* [91], this may be related back to measurable quantities through,

$$\mu_{21} = \sqrt{\frac{3\epsilon h(c/n)^3}{2\omega_{21}^3 \tau}}. \quad (2.8)$$

The lifetime  $\tau$  can be calculated in terms of the average absorption coefficient  $\alpha$  [55] as,

$$\tau = \frac{g_2}{g_1} \frac{\lambda^2}{8\pi n^2 \int \alpha d\nu}. \quad (2.9)$$

Here  $n$  represents the index of refraction at wavelength  $\lambda$ , and  $\int \alpha d\nu$  the integrated absorption cross section. Explicit calculation of the matrix element  $\mu_{21}$  is not necessary in this work. We will instead restrict our discussions of these matrix elements simply to whether or not they are zero or non-zero, i.e. allowed or forbidden respectively. This may be determined through group theory arguments by examining the symmetry of the initial and final states and of the dipole operator  $r$  that couples the transition between 1 and 2. A detailed description of which transitions are allowed and forbidden according to such symmetry arguments is provided in the appendices and discussed further in the results.

### 2.3 Effective mass theory and donors in silicon

Effective mass theory (EMT) is the theoretical framework used to predict electronic excited state energies for impurities in many materials. It relies primarily on the assumption that the effective mass of an impurity bound electron/hole is equal to that of the free electrons/holes in the conduction and valence bands respectively [101]. In the context of donors in silicon, this is an assumption that is most valid when the wavefunction describing a state extends over a large crystal volume and is large relative to the central cell potential. This tends to be true of excited states beyond the ‘1s’ ground state levels, and as such those higher levels are well approximated by EMT. The ‘1s’ levels by contrast, are more tightly localized, with the result that short range interactions with the central cell potential become important. Since EMT does not account for these, it is rarely sufficient to describe the ground states of even shallow donors.

The so-called deep donors in silicon have been a subject of recent interest [91] in the development of a new cavity-qubit technology. The ground states of these donors exist far below the conduction band edge, often rendering them poorly approximated by EMT. In these cases the ground state wavefunction is not so diffuse over many unit cells as it is for shallower donors and is instead tightly localized at the site of the impurity. The resulting large central cell interaction leads to a large donor-dependent chemical shift that drives the ground state far into the band gap. For sufficiently deep donors such as the chalcogens of group-VI, this can lead to the possibility of allowed transitions between their valley-orbit/spin valley interaction split ‘s’ states that would otherwise be forbidden for shallower donors such as those found in group-V. The large energy gap between the ground state and first excited states of these transitions in the chalcogens also leads to these transitions

being optically accessible in the relatively convenient mid-IR regime. By contrast, shallow donors like phosphorus require frequencies in the THz range to drive transitions from the ground state to the orbital excited states. Magnesium is a deep double donor intermediate between the extremely deep chalcogens of Group-VI and the shallow donors of Group-V. Even so, transitions between ‘s’ levels have never been observed for Mg in either the neutral or singly ionized charge state. As with shallower donors it may simply be that for Mg, the transitions from the 1s(A) ground state to other ‘s’ states such as 1s(T<sub>2</sub>) are too strongly forbidden by EMT to be observed directly in low temperature absorption measurements. Alternatively these states could have very short lifetimes, leading to broad transitions that would be difficult to observe.

Unlike many deep and shallow donor/acceptor impurities, magnesium does not incorporate primarily as a substitutional center. Instead it is largely known to inhabit the interstitial site that has the same T<sub>d</sub> symmetry as the lattice. As evidenced by Baber *et al.* [10], it may also inhabit a substitutional position, behaving as a double acceptor. According to theoretical predications made by Froyen and Zunger [40], Mg is more likely to inhabit an interstitial position in n-type Si and more likely to inhabit the substitutional site in p-type Si. If a complex is formed between the substitutional double acceptor and interstitial double donor species, this behaviour may give rise to a center that is isoelectronic in Si, as seen in Fig. 2.2.

As detailed by Kohn and Luttinger [81], six-fold degeneracy of the silicon conduction band due to identical minima located along  $\langle 100 \rangle$  and its equivalents leads to six degenerate solutions to Schroedinger’s equation of the form:

$$\Psi_i(\mathbf{r}) = \sum_{j=1}^6 \alpha_j^{(i)} F_j(\mathbf{r}) \phi_j(\mathbf{r}). \quad (2.10)$$

Here  $\phi_j(\mathbf{r})$  is the periodic Bloch function at the j-th conduction band minimum,  $F_j(\mathbf{r})$  are the hydrogen-like envelope functions which are solutions to the effective mass equation and coefficients  $\alpha_j$  correspond to the different irreducible representations. Single valley EMT is generally sufficient to describe higher excited states of hydrogenic donors in Si. For the valley orbit excited states, however, it is necessary to consider superpositions of different valleys. The six conduction band minima form a coordinate basis which we use to describe structure of the s-level wavefunctions. The  $\alpha_j$  coefficients, for each of the singlet ( $A_1$ ), doublet ( $E$ ), and triplet ( $T_2$ ) representations of the T<sub>d</sub> symmetry group are given as,

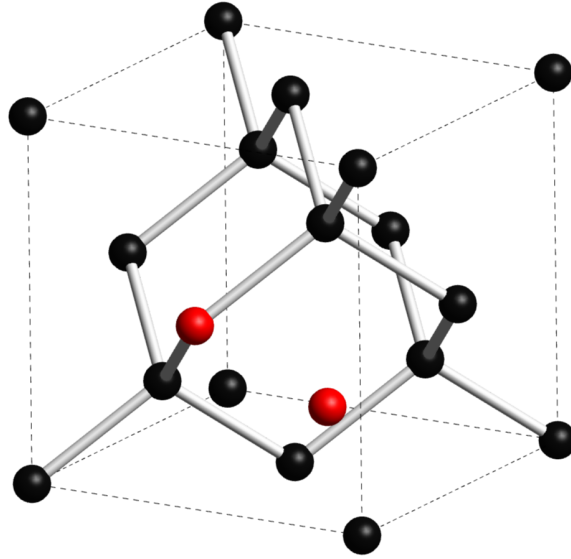


Figure 2.2: Here we show a schematic of the silicon lattice with magnesium inhabiting the interstitial and substitutional sites. Silicon atoms are indicated in black, and the interstitial and substitutional magnesium impurities are shown in red. Both sites possess the same  $T_d$  symmetry with four nearest neighbours. When found in the configuration seen in this figure, this may give rise an  $Mg_s$ - $Mg_i$  isoelectronic center.

$$\begin{aligned}
 (A_1) \quad a_j^{(1)} &= \frac{1}{\sqrt{6}}(1, 1, 1, 1, 1, 1) \\
 (E) \quad a_j^{(2)} &= \frac{1}{2}(1, 1, -1, -1, 0, 0) \\
 a_j^{(3)} &= \frac{1}{\sqrt{12}}(1, 1, 1, 1, -2, -2) \\
 (T_2) \quad a_j^{(4)} &= \frac{1}{\sqrt{2}}(1, -1, 0, 0, 0, 0) \\
 a_j^{(5)} &= \frac{1}{\sqrt{2}}(0, 0, 1, -1, 0, 0) \\
 a_j^{(6)} &= \frac{1}{\sqrt{2}}(0, 0, 0, 0, 1, -1)
 \end{aligned}$$

The splitting between the s-levels that arises from different superpositions of valleys is known as the valley-orbit interaction. From these coefficients it is clear that the  $A_1$  representation is perfectly spherically symmetric, making it ‘s-like’ both in valley character and wavefunction envelope. The  $E$  states are comprised of even combinations of valley states and as such are parity forbidden transitions from the  $A_1$  ground state in absorption though potentially

visible in Raman. Transitions to the  $T_2$  triplet states can however be symmetry allowed in absorption given that they comprise odd combinations of opposing valley states, making them ‘p-like’ in valley character while still maintaining an ‘s-like’ wavefunction envelope. This basic structure is plotted in Fig.2.3. For simplicity, in Fig.2.3 we treat the conduction band minima as single points rather than a range of values taken on by constant energy surface ellipsoids centered about  $k_0$ . If one were to take a more realistic view and include all these values, then instead of the simple damped cosine shown for schematic purposes here, we would see a sum of many frequency components yielding complex periodic structure.

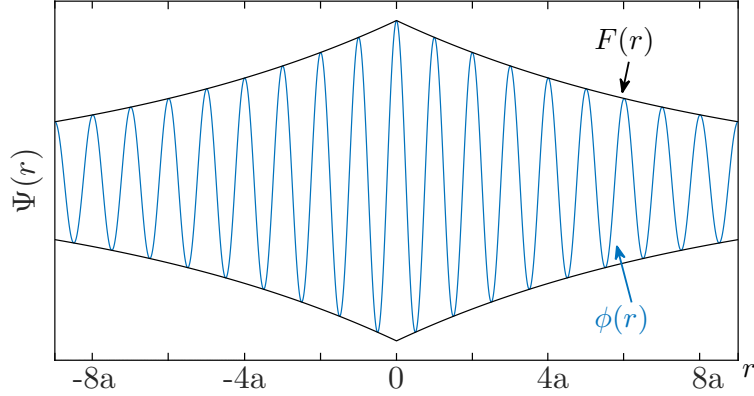


Figure 2.3: A simplified schematic of the fine structure given by the periodic Bloch functions  $\phi_j(\mathbf{r})$  damped by the exponential decay of the hydrogen-like wavefunction envelope  $F_j(\mathbf{r})$ . For the ground state,  $1s(A_1)$  wavefunction, there is a maximum at  $r = 0$  leading to the possibility of strong overlap with the central cell.

In the absence of central cell interaction, the ground state ‘1s’ level is six-fold degenerate. Thanks to the s-like hydrogenic envelope having strong overlap with the central cell, this degeneracy is lifted, splitting into singlet ( $A_1$ ), doublet ( $E$ ), and triplet ( $T_2$ ) levels. Of these, only the ground state  $A_1$  is expected to have fine structure that has a maximum at the origin, overlapping with the central cell, as illustrated in Fig. 2.3. Once electron spin is included the  $\alpha_j^{(i)}$  coefficients no longer form an eigenbasis for the Hamiltonian, since there are then twelve solutions, with two-fold degenerate  $1s(A_1)$ , four-fold  $1s(E)$  and  $1s(T_2)$  six-fold. The triplet level is split into  $1s(T_2)\Gamma_7$  (two-fold degenerate) and  $1s(T_2)\Gamma_8$  (four-fold degenerate). This additional splitting of the triplet representation is caused by the spin-orbit interaction. Because of the valley superposition nature of impurity wavefunctions in Si, spin-orbit is often used interchangeably with the term spin-valley interaction in this context. For impurities with nuclear spins the overlap  $1s(A_1)$  has with the central cell can further lead to a hyperfine interaction, lifting electron spin degeneracy between those levels, as seen for some deep donors like selenium. Thanks to this hyperfine interaction, the  $1s(T_2)\Gamma_7$  level forms a lambda transition that is the basis of a newly proposed deep-donor qubit in silicon [91].

While symmetry allowed by valley parity, the  $1s(A_1)$  to  $1s(T_2)$  transitions are not seen in shallow donor systems since these are well approximated by EMT which forbids them by symmetry of the wavefunction envelopes. Conversely donors like the chalcogens, with their more tightly localized  $1s(A_1)$  ground states, experience a large chemical shift pushing their ground states deep into the band gap. This leads to them being poorly approximated by EMT and correspondingly allowed through valley parity. Magnesium, the primary focus of this work, is somewhat intermediate between the chalcogens and shallow donors of group-V.

Energy levels of the system are determined by solving the Schrödinger equation. For example for a conduction band minimum along  $\langle 001 \rangle$  (i.e. the z-axis) we would seek solutions to:

$$\left[ \frac{-\hbar^2}{2m_l} \frac{\partial^2}{\partial z^2} - \frac{-\hbar^2}{2m_2} \left( \frac{\partial^2}{\partial x^2} + \frac{\partial^2}{\partial y^2} \right) - U \right] F(r) = EF(r). \quad (2.11)$$

Here  $U = e^2/\epsilon_r r$  is the screened Coulomb interaction modified by the relative permittivity ( $\epsilon_r \sim 11.7$  in silicon [36]), which accurately describes the impact of the impurity potential at long ranges but breaks down at close range. The eigenvalues  $E$ , analogous to those of the hydrogen atom are given for a hydrogenic impurity with as,

$$E_n = \frac{Z^2 m^* e^4}{2(4\pi\epsilon_r\epsilon_0\hbar)^2}, \quad (2.12)$$

where  $m^*$  is the electron effective mass,  $\epsilon_r$  the relative permittivity of the crystal,  $\epsilon_0$  the permittivity of free space, and  $Z$  the effective nuclear charge. The effective mass  $m^*$  is an average between  $m_1$  and  $m_2$ . Kohn and Luttinger cite a value of  $m^* = 0.31m_0$  since it yields the same ground state energy as the effective masses  $m_1$  and  $m_2$  would [81]. Likewise analogous to the ground state hydrogen atom solution, the lowest eigenstate is given by,

$$F(r) = \frac{1}{(\pi a^*{}^3)^{\frac{1}{2}}} e^{-r/a^*}, \quad (2.13)$$

where the effective Bohr-radius  $a^*$  in terms of the standard Bohr radius  $a_0$  is,

$$a^* = \frac{4\pi\epsilon_r\epsilon_0\hbar^2}{m^*e^2} = a_0 \frac{\epsilon_r}{m^*/m_0} \sim 20 \text{ \AA}. \quad (2.14)$$

Here for silicon we take  $\epsilon_r \sim 11.7$ ,  $m^* = 0.31m_0$ , and the hydrogen atom Bohr-radius  $a_0 = 0.53 \text{ \AA}$ . This implies an effective Bohr-radius for this lowest state spread over many unit cells. This assessment is fairly accurate where shallow donors are concerned and the donor electron is relatively weakly bound. For deep donors this breaks down, with the ground state being much more tightly localized to the donor impurity than EMT is able to predict. This leads to a large chemical shift that, for deep donors, plunges the ground state level deep into the band gap and separates the  $1s(A_1)$ ,  $1s(E)$ , and  $1s(T_2)$  valley orbit states. As detailed by Castner [20], further splitting between the  $1s(T_2)\Gamma_7$  and

1s(T<sub>2</sub>)Γ<sub>8</sub> components of 1s(T<sub>2</sub>) is governed by spin-orbit effects. For the 1s levels this may be incorporated by the Hamiltonian contribution,

$$H_{so} = \frac{\hbar^2}{2m^*c^2} \frac{1}{r} \frac{dU}{dr} \mathbf{L} \cdot \mathbf{S}, \quad (2.15)$$

with  $U$  the impurity potential and  $\mathbf{L}$  and  $\mathbf{S}$  the electron orbital and spin angular momentum respectively. Normally, one would expect Eq. 2.15 to give a result of zero for 1s levels. The fact that it does not for 1s(T<sub>2</sub>), arises from the spin-valley nature of the Γ<sub>7</sub> and Γ<sub>8</sub> levels, as detailed by Castner [20].

By contrast to the ground state levels, excited states 2p<sub>0</sub> and higher are very well described by EMT and the spacings between such higher excited levels are generally consistent between different donor systems. This makes it easy to recognize when a donor/acceptor impurity is present, even if its precise nature is not known. A plot of the silicon band structure, alongside a schematic of the same, including the ‘hydrogenic’ level structure of a donor is seen in Fig. 2.4. The calculated band structure is provided based on the empirical pseudopotential calculations of Cohen *et al.* [22] using code adapted from resources provided online by Dragica Vasileska and written originally by Santhosh Krishnan [131]. The only level to have large overlap with the central cell, namely the ground state ‘s’ level, is shown far below the conduction band edge, characteristic of a deep donor.

In the absence of spin-orbit interaction, the valence band at  $k = 0$  is sixfold degenerate. With the inclusion of spin-orbit coupling, this is split into levels with hole states that have total angular momentum  $j_h = 3/2$  and  $j_h = 1/2$ . The light hole and heavy hole bands, labelled in Fig. 2.4, have a total angular momentum  $j_h = 3/2$  and are fourfold degenerate at  $k = 0$ . The twofold degenerate  $j_h = 1/2$  band is split from the  $j_h = 3/2$  bands by the spin-orbit interaction and is commonly referred to as the split-off band.

Some corrections have been applied to EMT in terms of calculation of valley-orbit states in the form of intervalley interactions discussed by Altarelli [5, 6, 4]. These include so-called Umklapp interactions which are scattering processes that produce wave-vectors outside the first Brillouin Zone (BZ). This can occur for large enough wavevectors whose sum produces a vector pointing outside the BZ. This is equivalent to a process inside the first BZ that does not conserve phonon momentum. Altarelli’s calculations provide a more accurate estimate of the 1s(T<sub>2</sub>) levels than standard effective mass theory for deep donors such as the chalcogens, though calculation of the ground state 1s(A) level is still outside the scope of his work. Nonetheless, Altarelli’s predictions placed the binding energies of 1s(E) and 1s(T<sub>2</sub>) levels at 130 and 155 meV respectively for singly ionized helium-like donors, significantly deeper than the value of 125 meV calculated from single valley EMT for both levels. It should be noted that these values were calculated for substitutional singly ionized double donor defects like Se<sup>+</sup>, S<sup>+</sup>, and Te<sup>+</sup>. Since it is an interstitial double donor, Altarelli’s binding energy calculations may not apply as well to Mg<sup>+</sup>.

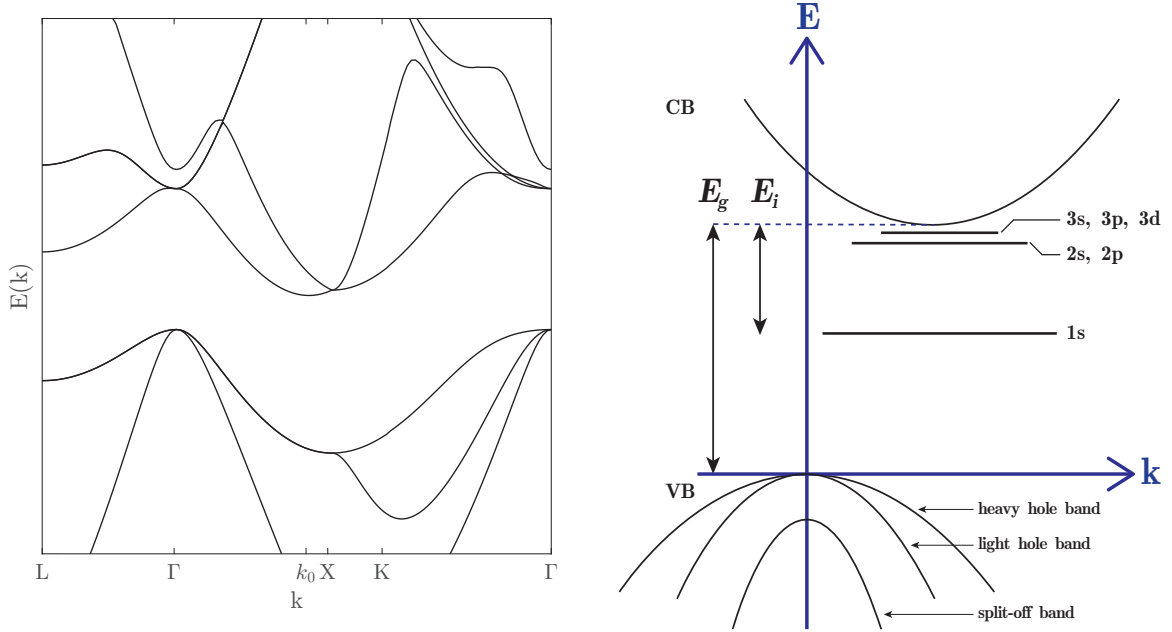


Figure 2.4: On the left we show the calculated structure of the silicon indirect band-gap [22, 131]. These are separated by  $k_0$  85% of the way along the  $\langle 100 \rangle$  axis to the zone boundary at  $X$ . Other commonly labelled points of symmetry in the first Brillouin zone are also indicated, including  $\Gamma$ ,  $L$ , and  $K$ . On the right in a simplified schematic of this same band structure, the hydrogenic level structure characteristic of a donor impurity is labelled between the two extrema, with splitting  $E_g$  between the conduction band (CB) maximum and valence band (VB) minimum. The  $n = 1$  ‘s’ level, thanks to a large chemical shift [129], is driven far into the bandgap for relatively deep donors like Mg, giving them a large ground state ionization energy  $E_i$ . The  $n = 2$  and  $n = 3$  levels are also indicated. States of higher  $n$  are progressively closer to the conduction band edge. Higher excited states have a progressively smaller extent in  $k$ -space, corresponding to a wavefunctions that are more extended in real space. Valence band structure, including the light and heavy hole bands degenerate at  $k = 0$  ( $j_h = 3/2$ ), and the split-off band ( $j_h = 1/2$ ) energetically shifted by the spin-orbit interaction, are also indicated.

The tetrahedral symmetry possessed by most interstitials in silicon and all substitutional impurities implies the possibility of fine structure in some hydrogenic excited states. As discussed in the introduction this is most notable in the  $p_{\pm}$  states which appear as doublets thanks to a lifting of degeneracy between the two allowed transitions that comprise these states in  $T_d$ . Many centers in silicon form complexes, however, and there are other interstitial sites beyond the standard  $T_d$ , such as  $C_{3v}$  along the  $\langle 111 \rangle$  axis. In either case the symmetry of the alternate site or of the complex is reduced relative to  $T_d$ . If the new symmetry is known, it is possible through group theory arguments, discussed in detail in the appendices, to predict how the representations of  $T_d$  are split into new representations in the reduced symmetry. An extension of the same group theory discussion demonstrates how this leads to the possibility of new allowed transitions. Allowed transitions are those for which the

condition  $\int \Psi_i \hat{O} \Psi_j \neq 0$  is satisfied, with initial and final states  $\Psi_i$  and  $\Psi_j$  coupled by the operator  $\hat{O}$ . This condition can be evaluated by checking the symmetry of the initial and final states of that transition and that of the dipole operator that couples them for transitions in absorption as seen in Eq. 2.7. This can lead to additional allowed transitions in the reduced symmetry configuration relative to  $T_d$ . Degeneracy between these additional levels can be lifted by central cell interaction or other perturbations, resulting in potentially complex fine structure. The state  $2p_0$  for instance is a singlet in  $T_d$  symmetry, while in a reduced symmetry like  $C_{3v}$ , we expect as many as four components.

The donors best described by EMT are unsurprisingly the shallow donors. Lithium, the shallowest of these, has a ground state ionization energy of 33.999 meV [101]. The measured binding energy is a relatively close match to the predicted value using single-valley EMT for hydrogen-like centers, which is determined to be 31.26 meV. Lithium, like magnesium, is known to incorporate interstitially in Si, and inhabits the  $T_d$  interstitial site. As a donor with an especially small ionic radius, there was initially some speculation that lithium might just as easily inhabit alternate interstitial sites. Unlike most donors, Li does not have  $1s(A_1)$  as its ground state. In this case, as determined by ESR measurements carried out by Watkins *et al.*  $1s(E)$  and  $1s(T_2)$  are nearly degenerate and sit  $\sim 1.8$  meV below  $1s(A_1)$  [134].  $1s(E)$  and  $1s(T_2)$  have only a small response to the central cell, leading to minimal deviation from the EMT predicted ground state ionization energy. At slightly elevated temperatures relative to LHe (liquid  $H_2$ , 20.28 K), Aggarwal *et al.* also collected data demonstrating that the  $1s(A_1)$  level could be thermally populated, leading to the observation of a transition to  $2p_0$  from this level displaced down in energy from the true ground state to  $2p_0$  transition by  $\sim 1.8$  meV [3], consistent with the measurements of Watkins *et al.* Fine structure observed in some features of the Li excited state spectrum [108], including an apparent triplet in  $2p_0$  and doublets in  $2p_{\pm}$  and  $4p_{\pm}$ , is a consequence of this near degenerate ground state. A slight splitting between  $1s(E)$  and  $1s(T_2)$  may be what gives rise to the splitting between the doublet components of  $2p_{\pm}$  and  $4p_{\pm}$ . The triplet of  $2p_0$  can be described in terms of the valley orbit splitting of that level.  $2p_0$  has the representation  $A_1+E+T_2$  in the  $T_d$  group. Normally, when  $1s(A_1)$  is the ground state, only transitions to levels with  $T_2$  symmetry are allowed, leaving  $2p_0$  a singlet, since  $1s(E)$  and  $1s(T_2)$  are not populated at the low temperatures typically employed for this spectroscopy. Since the ground state of Li consists of near-degenerate  $1s(E)$  and  $1s(T_2)$  levels however, it can be shown (see appendices), that transitions to states with any of the irreducible representations  $A_1$ ,  $E$ , and  $T_2$  are allowed.

In valley-space,  $p_0$  states, i.e. with quantum number  $m = 0$ , are those which are aligned along the axis of the constant energy surface ellipsoid. The  $p_{\pm}$  states, i.e.  $m = \pm 1$  are orthogonal to this axis.

### 2.3.1 Double donors in silicon

Double donors in silicon, such as interstitial Mg and the substitutional chalcogens all possess two extra valence electrons relative to Si. These impurities are often thought of as solid state analogues of the helium atom. Many detailed studies of the chalcogens in particular have been made [68, 44, 122, 119, 76, 77]. Magnesium, while less well understood, has likewise been the object of several investigations [39, 59, 58, 56, 57, 60, 61]. Grossman *et al.* [47] provide a review of various spectroscopic studies of all these centers. Excited states of the neutral double donor centers are noted to agree well both with energies observed empirically and those predicted by EMT for the hydrogenic group-V shallow donors. This is thanks to screening of the nucleus by the unexcited valence electron, leaving the excited valence electron to experience a relatively hydrogen-like nuclear charge of approximately  $Z = 1$ . By contrast in the singly-ionized, helium-like spectrum, the more tightly bound remaining electron sees an effective nuclear charge  $Z = 2$ . As implied by Eq. 2.12, this gives rise to bound states with spacings a factor of  $Z^2 = 4$  different between hydrogen-like and helium-like spectra.

The hydrogen-like ground state binding energies of group-V donors are calculated to be 31.262 meV in EMT [68]. Lithium, as previously discussed, is closest to this value, with an ionization energy of 33.999 meV [101]. The position of the ground state diverges further for other impurities in group-V. For helium like centers, such as the double donor systems discussed here, the single-valley EMT calculated values are 56.52 meV and 125 meV for the neutral and singly ionized species respectively [101]. The former value is determined by scaling the EMT predicted value for hydrogen by the ratio of the ground state binding energies for hydrogen and helium. As detailed earlier, further calculations by Altarelli [5], which incorporate intra-valley scattering effects, place the binding energy of the valley orbit excited states at 130 and 155 meV for  $1s(E)$  and  $1s(T_2)$  respectively. As with the shallow donors of group-V, Mg and the chalcogens show increasing deviation from EMT predicted values with increasing binding energy for both the hydrogen-like neutral and helium-like singly ionized donor spectra.

The spin-orbit interaction, which splits the  $1s(T_2)$  representation into  $\Gamma_7$  and  $\Gamma_8$  states is cited by Grossman *et al.* as particularly important to an understanding of double donor electronic structure. Spin-orbit coupling in Si is small, and as such the magnitude of the  $\Gamma_7$  to  $\Gamma_8$  splitting is to first order determined by the impurity. This is most true of the heavier chalcogens Se and Te, in which spin-orbit coupling is strongest. In sulfur spin-orbit coupling remains relatively weak [43]. The exchange interaction between the two electrons of a neutral double donor influences the strength of this spin orbit coupling. As discussed by Grossman *et al.* [47], the neutral charge species of a double donor impurity will see this splitting reduced relative to the singly ionized species.

As a somewhat shallower donor relative to the chalcogens, Mg may not have a sufficiently strong central cell interaction to enable transitions between the  $1s(A_1)$  ground state and valley-orbit split excited s-states. It is also possible that these features are simply too broad to observe if the lifetimes associated with those transitions are sufficiently short. In either case this may explain why such transitions, along with the presumably weak spin-orbit coupling splitting for the relatively light Mg impurity, have never been observed. As the shallowest known isolated double donor, magnesium is predicted to be more helium-like than its other double donor counterparts, in that, like helium its excited states are expected to diverge less from predicted EMT values. Theoretical studies [136, 87, 17, 16] have also shown that defects like magnesium that inhabit interstitial sites are less effectively screened by valence electrons than those occupying substitutional sites. This means that one can expect some overall deviation from the screened Coulomb potential  $U = e^2/\epsilon_r r$  behaviour of the central cell. For the neutral species, screening of the excited valence electron by the other is still very effective. This has been seen in past investigations [129] in which excited states of  $Mg_i^0$  are noted to show the expected excellent agreement with EMT, barring some relatively large deviations for the lowest lying excited states like  $2p_0$ . This deviation of the relatively tightly bound lower excited states is best understood as a consequence of the less localized inner electron leading to imperfect screening of the nucleus. Imperfect screening of the remaining valence electron in  $Mg_i^+$  by the core electrons may also explain why we see central cell splitting of the  $p_{\pm}$  levels as high as  $6p_{\pm}$  as shown later in the results section. In Tab. 2.1 we include energies for the ground states and valley orbit excited states of the chalcogen double donors and magnesium as detailed by Grossman *et al.*

Label	S <sup>0</sup>	Se <sup>0</sup>	Te <sup>0</sup>	Mg <sup>0</sup>	D <sup>0</sup> <sub>EMT</sub>	S <sup>+</sup>	Se <sup>+</sup>	Te <sup>+</sup>	Mg <sup>+</sup>	D <sup>+</sup> <sub>EMT</sub>
1s(A <sub>1</sub> )	318.3	306.6	198.8	107.5	-	613.5	593.3	410.8	256.5	-
1s(T <sub>2</sub> ) $\Gamma_7$	34.6	34.4	39.1	-	56.52	183.9	163.7	171.0	-	155
$\Gamma_8$						184.3	166.0	176.4		
1s(E)	31.6	31.2	31.6	-	56.52	-	-	-	-	130

Table 2.1: Binding energies in meV for ground state and valley orbit excited states of a number of known double donors in Si for both neutral and singly ionized charge states, as compiled in [47]. Binding energies for EMT predicted 1s levels are as given by Pajot [101] for the neutral species D<sup>0</sup><sub>EMT</sub>, and Altarelli’s multi-valley EMT calculations for the ionized species D<sup>+</sup><sub>EMT</sub> [5].

Investigations by Grimmeiss *et al.* and Kleverman *et al.* discuss capture processes at the sites of double donor defects in silicon [46, 45, 80] for electrons and holes. Electron capture, studied for singly ionized selenium and sulfur defects by Grimmeiss *et al.* [46, 45] was reported to be consistent with a cascade capture process via excited states of the defects. In this model electrons are captured by an excited state near the conduction band and subsequently travel down the ladder of progressively lower energy states, emitting phonon(s)

at each step in the ladder as described by Lax [85]. Grimmeiss *et al.* performed DLTS measurements using p-n junctions doped with Se and S to study thermal emission rates of electrons as a function of temperature for the different centers. Temperature dependence measurements of capture cross section were made using current transient techniques. As described by Grimmeiss [42], voltage pulses applied to the p-n junction under reverse bias allowed current to penetrate the depletion zone for a short time during which carriers would recombine with defects creating a change in capacitance related to the amount of charge captured.

The capture of holes by double donors is detailed by Kleverman *et al.* [80] in Se, S, and Te doped samples using DLTS techniques. Kleverman *et al.* observe rates of thermal emission in both singly ionized and neutral donors. Their results demonstrate that the capture of holes by neutral donors occurs through Auger processes, wherein the capture of a hole by a neutral donor  $D^0$  releases enough energy to excite the second electron to the conduction band. Capture cross sections of holes for the singly ionized  $D^+$  centers  $\sigma_{pD^+}$  were noted to be three orders of magnitude smaller than those for neutral equivalents  $\sigma_{pD^0}$ . For ionized defects, hole capture cannot be described by an Auger process, and instead is expected to obey either radiative capture or a multiphonon emission (MPE) process, or some combination of the two. The authors also note that, in agreement with theoretical predictions for Auger recombination processes [9, 97, 69, 106]  $\sigma_{pD^0}$  increases with increasing binding energy of the donor, with S having the largest capture cross section and Te the smallest. Only  $S^+$  reveals significant temperature dependence. Kleverman *et al.* [80] describe the capture process at this center with an MPE model discussed by Englman *et al.* [37] which matches their observations.

Investigations by Pavlov *et al.* [103], have included experimental studies of electron relaxation associated with the neutral charge state  $Mg_i^0$  of magnesium. The authors employed a free-electron laser, tunable to resonance with transitions of interest. In particular they examined relaxation processes originating from the relatively low lying hydrogenic excited states  $2p_0$  and  $2p_{\pm}$  in addition to relaxation from the conduction band. These were modelled as cascade processes through the ladder of available hydrogenic levels and valley orbit excited states, which gave reasonably good agreement with their observations.

## 2.4 Donor bound excitons

Excitons are weakly Coulomb coupled electron-hole pairs. The strength of the interaction between an electron and hole separated by distance  $r$  is given according to,

$$U = -\frac{e^2}{4\pi\epsilon_0\epsilon_r r}. \quad (2.16)$$

Where the Coulomb interaction is modified by the relative permittivity  $\epsilon_r$  of the crystal. Excitons can be free to propagate through a crystal in which case they are known as free

excitons (FE) or they can be bound to a neutral impurity, in which case they are called bound excitons (BE). A BE may be associated with donor or acceptor impurities. In the case of acceptors, a negatively charged core and positively charged hole form the neutral center. For neutral donor centers there is a positively charged core and negatively charged electron. Bound excitons are seen in this thesis for a range of shallow donors, all of which comply with Haynes' Rule, an semi-empirical relation stating that  $E_{ex} = 0.1E_I$ , i.e. that the localization energy of the bound exciton ( $E_{ex}$ ) is approximately one-tenth that of the ground state ionization energy of the donor ( $E_I$ ). A theoretical basis for this rule is discussed in the next section.

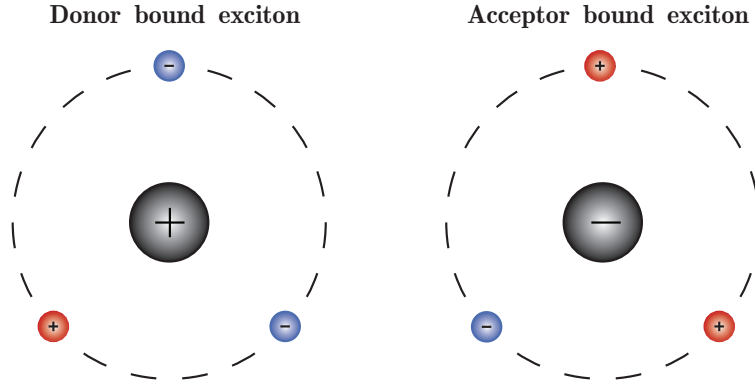


Figure 2.5: Here we show a cartoon depicting donor and acceptor bound excitons. These consist of two electrons and a hole bound to a net-positive core (donor) and two holes and an electron bound to a net negative core (acceptor).

Excitons bound to a donor may recombine radiatively, yielding a detectable photoluminescence (PL) signal at a photon energy given by  $E_g - E_{ex} - E_{FE}$ , with the impurity specific localization energy of the exciton  $E_{ex}$  and free exciton binding energy  $E_{FE} \sim 14.7$  meV [25] subtracted from the bandgap energy  $E_g$ . Non-radiative effects, through Auger recombination, are also possible. In this case exciton recombination provides energy for the remaining electron or hole to be excited to the conduction or valence band. This greatly impacts the efficiency of photon emission from these centers. In fact the process of Auger recombination in group-V shallow centers has near unit efficiency, opening up the possibility of an efficient means of electrical detection that has been exploited in studying donor bound exciton transitions in these systems [92].

Silicon has an indirect bandgap and as such recombination of the electron-hole pair implies the involvement of wvector-conserving phonons, meaning that we actually expect emission at an energy  $E_g - E_{ex} - E_{ph}$  with  $E_{ph}$  the relevant phonon energy [101]. This leads to strong transitions in PL called phonon replicas, of which we most clearly observe the transverse optical (TO) and transverse acoustic (TA) modes. It is also possible for these PL transitions to occur without the assistance of phonons, though for bound excitons corresponding to relatively shallow impurities this is a rarer process. This is because such

no-phonon (NP) processes are enabled by the short range interactions generated by the donor impurity known as the central-cell potential which are responsible for scattering the electron to the Brillouin-Zone center, thereby overcoming the indirect Si bandgap. For shallow impurities the no-phonon (NP) transitions are thus usually correspondingly weaker than the TA/TO replicas.

In general phonon-replicas are much broader than their no-phonon counterparts. They experience broadening both as a consequence of finite lifetime and because the momentum conserving process of exciton recombination implies a spread in crystal momenta. This means that they effectively sample from a range of phonon wave-vectors which leads to broadening that is proportional to the slope of the phonon branch in question at/near  $k_0$ . Near  $k_0$  the gradient of the TA and TO branches along  $\langle 001 \rangle$  and equivalent axes produces a symmetrical broadening. The second derivative, in directions perpendicular to these high symmetry directions, produces a positive result. This implies asymmetric broadening to low energy, leading to the low energy tails visible in the TO and particularly pronounced in TA phonon replicas [127]. In general, one anticipates increased symmetric and asymmetric broadening for deeper bound excitons. This is because their larger binding energy, corresponding to a more spatially localized electron-hole pair, implies an increased spread in  $k$  [127]. It is also true however that sufficiently deep impurities may not require wave-vector conserving phonon replicas at all.

BE localization energies of most impurities are sufficiently distinct to allow use of BE emission for characterizing chemical impurities in Si. Those with similar binding energies such as Sb and P [30] can be distinguished by other means, such as the ratio of intensities of their NP and TO phonon replica lines.

### 2.4.1 Hayne's Rule

Hayne's Rule, a semi-empirical relation first discussed by Haynes [49] describes a linear relation between the ground state ionization energy  $E_I$  of an impurity and the donor or acceptor bound exciton localization energy ( $E_{ex}$ ) of that same impurity. Haynes found that many donors followed the relation  $E_{ex} = 0.1E_I$ . This is Haynes Rule in its simplest form. H. Atzmüller and U. Schröder [8], describe general forms of this relation,

$$E_{ex} = A + BE_I, \tag{2.17}$$

The authors also discuss an alternative form of Eq. 2.17, describing Hayne's rule in terms of the donor specific splitting between the 1s and 2p levels. As the first hydrogenic excited state beyond the 1s level transitions, the  $2p_0$  level is still often found somewhat lower in energy than its EMT predicted value, particularly for deep donors. The authors discuss Eq. 2.17 in terms of first order perturbation theory and ultimately find good agreement for

their predicted values of  $A$  and  $B$  with experimental values. In their treatment, Atzmüller and Schröder split the system Hamiltonian into two components,

$$H = H^0 + H^{cs}. \quad (2.18)$$

Here  $H^0$  contains contributions of the host lattice and treatment of the impurity as a Coulomb potential. The second term,  $H^{cs} = p_{cs}W$ , carries the impurity specific central cell interaction with  $p_{cs}$  a constant coefficient that is impurity specific, and  $W$  a general potential that is impurity agnostic.

For the case of an exciton bound to a neutral donor we have the following, neglecting central cell interaction:

$$H_C^0 \psi_c^0 = E_C^0 \psi_c^0, \quad (2.19)$$

$$H_I^0 \psi_{1s}^0 = E_{1s}^0 \psi_{1s}^0. \quad (2.20)$$

Here  $H_C^0$  is the Hamiltonian of the donor-exciton complex and  $H_I^0$  that of the neutral impurity. Including the central cell perturbation, we have to first order in perturbation theory:

$$E_c = E_c^0 + p_{cs} \langle \psi_c^0 | W(\mathbf{r}_1) | \psi_c^0 \rangle, \quad (2.21)$$

$$E_{1s} = E_I = E_{1s}^0 + p_{cs} \langle \psi_{1s}^0 | W(\mathbf{r}_1) | \psi_{1s}^0 \rangle. \quad (2.22)$$

Here  $\mathbf{r}_1$  is the coordinate of the electron. Localization energy of the exciton  $E_{ex}$  is given as,

$$E_{ex} = E_c - E_{FE} - E_I. \quad (2.23)$$

Here  $E_c$  is the energy of the complex,  $E_x$  the energy of the free exciton, and  $E_I$  the ionization energy of the impurity. For a neutral donor, there are two electrons associated with the donor-exciton complex, and the perturbation takes the form  $H^{cs} = p_{cs}(W(\mathbf{r}_1) + W(\mathbf{r}_2))$ . To first order in perturbation theory we write,

$$E_c = E_c^0 + 2p_{cs} \langle \psi_c^0 | W(\mathbf{r}_1) | \psi_c^0 \rangle. \quad (2.24)$$

Combining Eq. 2.23 with Eqs. 2.21 and 2.22 we have,

$$E_{ex} = A + BE_I, \quad (2.25)$$

with,

$$A = E_c^0 - E_{FE} - (B + 1)E_I^0 = E_{ex}^0 - BE_I^0, \quad (2.26)$$

and

$$B = 2 \frac{\langle \psi_c^0 | W(\mathbf{r}_1) | \psi_c^0 \rangle}{\langle \psi_{1s}^0 | W(\mathbf{r}_1) | \psi_{1s}^0 \rangle} - 1. \quad (2.27)$$

With a form for the potential  $W(\mathbf{r}_1) = \delta(\mathbf{r}_1)$  and a trial wavefunction  $\psi_c^0$  specified by Atzmüller and Schröder, the authors determine values for the coefficients  $A$  and  $B$ . For silicon these are calculated to be  $B = 0.081$  and  $A/E_I = 0.02$ . The value of  $B$  in particular is in good agreement with the observed value of  $\sim 0.1$ .

### 2.4.2 Donor-acceptor pair (DAP) bands

Donor-acceptor pair luminescence is a well known phenomenon in many relatively heavily compensated semiconductors [35]. In this thesis, donor-acceptor pair bands are observed as broad phonon assisted features in samples containing large concentrations of both donor and acceptor species. These represent the recombination of electrons and holes associated with spatially nearby donors and acceptors respectively. The resulting emitted photon has an energy dependent on the relative separation of the post-recombination donor-acceptor pair. A closely spaced pair will yield emission towards the higher energy edge of a DAP band, whereas those spaced further apart result in emission towards the low energy edge. As silicon is an indirect bandgap semiconductor, recombination of electrons captured through the conduction band and holes captured through the valence band is often a phonon mediated process. While no-phonon transitions are possible through central-cell effects, as they are for bound exciton transitions, in this work we only make note of the transverse acoustic and optical (TA and TO) phonon assisted bands. Since in any heavily doped semiconductor there will be a continuum of possible separations, this gives rise to the following relation,

$$E(r) = E_g - (E_A + E_D) + E_C - E_{vdw} - E_{ph}. \quad (2.28)$$

Here  $E_C = e^2/4\pi\epsilon_0\epsilon_r r$  and  $E_{vdw} = \alpha/r^6$  are Coulomb and Van-der Waals terms,  $E_g$  is the silicon bandgap energy and  $E_A, E_D$  are the ionization energies of the donor and acceptor species respectively. The value  $\alpha$  in the Van-der Waals term is a constant specific to an individual donor-acceptor pair. Since it drops off as  $r^6$  these interactions are only considered relevant in the limit of small separations. With the energy of the emitted photon dependent on the Coulomb interaction as indicated, it is clear that higher energy DAP luminescence represents physically closer donor-acceptor pairs. From Eq.2.28 it is possible to infer a rough estimate of the ionization energy of an unknown donor or acceptor species if the other counterpart is known by looking for the cutoff of either the TA or TO bands and subtracting the appropriate energies.

For particularly nearby donors and acceptors, photon emission at discrete spacings of the crystal lattice can often be resolved. These spacings can be written as a function of the lattice constant  $a$  in two distinct ways. Silicon is comprised of two FCC sub-lattices

offset by  $(a/4, a/4, a/4)$ . For a given impurity defined to be at the origin, its corresponding donor or acceptor counterpart will be located at position  $r = n_1 a_1 + n_2 a_2 + n_3 a_3$ . Here  $n_1, n_2, n_3$  are integers and  $a_1, a_2, a_3$  are basis vectors with magnitude  $a/2$  or  $a/4$ , depending on whether they correspond to defects from the same sub-lattice (type I) or two different sub-lattices (type II). Based on this the set of allowed DAP separations can be calculated [138]. Depending on whether the impurities undergoing DAP recombination correspond to type I or II geometries, these separations can be written in terms of shell spacings as,

$$r_m = \left(\frac{1}{2}m\right)^{\frac{1}{2}} a_0, \quad (2.29)$$

or

$$r_m = \left(\frac{1}{2}m - \frac{5}{16}\right)^{\frac{1}{2}} a_0, \quad (2.30)$$

respectively. Here the indices  $m$  denote the shell spacings, with  $m = 1$  being the closest donor-acceptor pair,  $m = 2$  the second, etc. [141]. Luminescence at these discrete values has been detailed by a number of authors studying a range of semiconductors [35, 109, 123, 124, 140, 141].

## 2.5 Isoelectronic bound excitons

In this study we also discuss observation of a so-called isoelectronic bound exciton (IBE). Isoelectronic centers occur for impurities/complexes that are electronically neutral with respect to the host medium. Through distortion of the crystal lattice and central cell attraction from the impurity/complex itself, IBE's are capable of forming attractive potentials for electrons or holes that result in bound excitons with much larger localization energies than normal BE centers. As a consequence they also generally lack, or have relatively weak wave-vector conserving phonon replicas. Depending on which particle an isoelectronic center forms an attractive potential for, hole or electron, it is referred to as donor-like or acceptor-like respectively [62]. The complementary particle, electron or hole is then bound by the Coulomb field of the first. Determining whether an IBE is donor or acceptor-like requires study of their excited state spectrum, for which a series of donor/acceptor like effective mass states would be expected.

These centers do not require an additional electron or hole to have net neutral charge, meaning their PL emissions are often not as impacted by Auger recombination as donor and acceptor BE emission is [133, 96]. As a consequence IBE centers are generally characterized by long lifetimes and strong NP PL lines. Their potentially high quantum efficiency has also made them a subject of interest as near-IR emitters [101]. While replacement of a silicon atom by a different atom from column IV of the periodic table does form an isoelectronic impurity, none of the simple substitutional replacements produces an IBE [12, 101]. IBE's

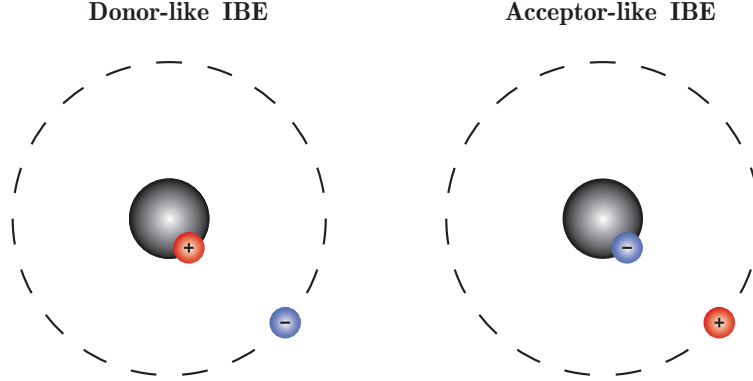


Figure 2.6: Here we show a cartoon depicting donor (left) and acceptor-like (right) isoelectronic bound excitons. One particle is bound tightly by the central cell potential of the neutral impurity and the second particle is localized by the Coulomb field of the first.

are however known to form for complexes in Si [54]. Beryllium for instance, which acts dominantly as a substitutional double acceptor and to a lesser degree as an interstitial double donor, is known to form substitutional-interstitial isoelectronic pair centers that can bind excitons [52, 53]. Analogous to this, complexing of interstitial magnesium double donors with substitutional magnesium, which likely forms a double acceptor [10] is thought to result in the IBE we observe in this work.

Despite being such deep binding centers that do not in general have strong wave-vector conserving phonon replicas, not all PL associated with an IBE is necessarily confined to the no-phonon line. In addition to a broad band related to the phonon density-of-states in Si, most IBE systems are known to display local vibrational mode (LVM) phonon replicas near the main no-phonon transitions [25]. These represent vibrational modes of the defect centers themselves, rather than excitations of the lattice. To be truly isolated from the phonon density of states in Si such modes are expected to occur at energies greater than  $\sim 65$  meV. Such modes have been observed by Henry *et al.* [53] in association with the Be IBE pair center, including one at 104.7 meV. The presence of these features can play a key role in identification of the responsible center. This is demonstrated in particular by the observations of Henry *et al.* [53] which included identification of a Be LVM matching closely with calculated predications of Tarnow *et al.* [126].

Common to many IBE centers are a series of low lying local modes that are neither wavevector conserving replicas of the no-phonon line nor are they beyond the  $\sim 65$  meV limit. We see evidence of several such local modes in our studies of the Mg isoelectronic pair center.

### 2.5.1 IBE ground state electronic structure

The electronic structure of an IBE ground state is determined by electron-hole coupling or potential lack thereof. In the case of an acceptor-like IBE with diamagnetic unexcited ground

state, one expects coupling between spin 1/2 electrons and spin 3/2 holes. Coulomb coupling of these particles produces a threefold degenerate  $J = 1$  branch and a fivefold degenerate  $J = 2$  branch through  $j$ - $j$  coupling [90]. Defects in silicon introduce strain through distortion of the lattice. This results in a lifting of degeneracy between  $m_h = \pm 3/2$  and  $m_h = \pm 1/2$  hole states leading to a total of five possible levels the ground state can split into. Written as  $|J, M\rangle$ , with  $M$  the projection onto the z-axis of  $J$ , these states are as follows,

$$|1, 0\rangle, |1, \pm 1\rangle \quad (2.31)$$

$$|2, 0\rangle, |2, \pm 1\rangle, |2, \pm 2\rangle \quad (2.32)$$

The  $J = 1$  branch lies below  $J = 2$ , separated by the exchange energy which may be found experimentally [90]. Remaining degeneracy between these levels can be lifted through external strain and magnetic fields. Because of their many possible ground state components, bound exciton no-phonon lines can have complex behaviour as a function of temperature due to the potential for thermalization between nearby states. In the case of an acceptor-like IBE with a paramagnetic unexcited ground state, there would be no electron-hole coupling at all, since pairing of the ground state electron with the one tightly localized by the IBE leaves no spin to couple to the hole.

For a donor-like IBE, one anticipates coupling between the Coulomb coupled spin 1/2 electron and tightly bound hole, which has spin 1/2. The difference between the effective spin of the donor-like IBE hole and that of the Coulomb coupled hole in the acceptor-like IBE is a consequence of degeneracy being lifted between the  $j = \pm 3/2$  and  $j = \pm 1/2$  branches by the central cell potential. Coupling between the two spin 1/2 particles of the donor-like IBE yields  $J = 0$  and  $J = 1$  branches with the different possible  $|J, M\rangle$  states written as,

$$|0, 0\rangle \quad (2.33)$$

$$|1, 0\rangle, |1, \pm 1\rangle \quad (2.34)$$

Thus for this case we have a total of three possible states, barring further lifting of degeneracy through external perturbations.

### 2.5.2 Isotope shifts of no-phonon lines

In the no-phonon (NP) lines of shallow donor BE centers, isotopic shifts are generally very hard to resolve. In deeper centers, like IBE's, these shifts are significantly larger and in  $^{28}\text{Si}$  are relatively easy to observe, leading to a powerful tool for identifying these centers through their isotopic fingerprints [117]. The initial and final states of NP transitions by definition do not involve any phonon modes, but both initial and final states do contain the zero-point energy  $E_0 = \sum_i \frac{1}{2} \hbar \omega_i$ . 'Mode softening' of this quantity, caused by the weakening

of covalent bonds in the presence of charge carriers that change force constants between nearest neighbours are thus not directly observable. Likewise the mass difference between two isotopes of a defect generate a shift in  $E_0$  and are similarly not seen directly. Heine and Henry demonstrate that a cross term between these two effects is ultimately responsible for generating the observable shift. The authors [51] describe a simple model detailing the anticipated shifts due to isotope effects, which can be derived by consideration of the following harmonic oscillator model for an impurity of mass  $M$  oscillating at frequency  $\omega$  with force constant  $\Lambda$ ,

$$M\omega^2 = \Lambda(1 - \gamma_c P). \quad (2.35)$$

Having a charge carrier bound to the impurity lowers the force constant by a fraction  $\gamma_c$  through the electron-phonon interaction. Here  $P$  represents the probability that the bound carrier is localized on the atom in question and its bonds.  $P$  varies from 1, representing a charge carrier completely localized on an impurity, to near 0 if the carrier probability density for the BE is diffuse over a large crystal volume. If we imagine substituting a heavier isotope of our defect, we make the substitution  $M = M + \Delta M$ . Expanding and keeping only lowest powers of  $\Delta M$  and  $\Delta\omega$  we can write,

$$\omega^2 + 2\omega\Delta\omega = \frac{\Lambda}{M} \left[ 1 - \gamma_c P - \frac{\Delta M}{M} + \gamma_c P \frac{\Delta M}{M} \right]. \quad (2.36)$$

Here we see the ‘mode softening’ term  $\gamma_c P$ , the isotopic substitution  $\frac{\Delta M}{M}$  and a cross term  $\gamma_c P \frac{\Delta M}{M}$ . As discussed, these first two terms are not directly observable, and so the cross term must be responsible for the isotopic shift. The shift  $S$  can be written as,

$$S = \frac{3}{2}\hbar\Delta\omega = \frac{3}{4}\frac{\hbar}{\omega}\frac{\Lambda}{M}\frac{\Delta M}{M}\gamma_c P \approx \frac{3}{4}\hbar\omega\frac{\Delta M}{M}\gamma_c P. \quad (2.37)$$

With  $S \approx \frac{3}{4}\hbar\omega\frac{\Delta M}{M}\gamma_c P$  true for  $\gamma_c P \ll 1$ . From this we see that the shift is not only inversely proportional to the mass  $M$  of the impurity but is also dependent on the probability  $P$  that the charge carrier becomes bound to it. This value is small for shallow donors with their relatively weak central cell effects, such as boron and phosphorus. For deeper donors like IBE’s  $P$  is much larger and we are able to see large isotope shifts that allow identification of these centers by their isotopic fingerprints. The mass of IBE constituents also is known to have an impact on the low lying satellite mode replicas characteristic of many IBE spectra. The energy of such modes for different isotope masses  $M$  is proportional to  $1/\sqrt{M}$ . This can be a helpful tool in determining the composition of an unknown center and in demonstrating that such modes are related to the main NP line. It is also clear however, from the  $1/\sqrt{M}$  dependence, that heavier impurities will see a smaller relative shift in positions of local mode replicas than lighter ones.

In some larger isoelectronic complexes, such as the isoelectronic Cu<sub>4</sub> defect [117, 118, 128], the relative position of different isotopes in the defect creates additional complexity in the isotopic fingerprint. In such cases energies of lines in the fine structure determined both by the position and isotopic mass of constituents in the complex. The feature ultimately identified as Cu<sub>4</sub> by Steger *et al.*, was first observed by Minaev *et al.* [89]. Piezospectroscopic studies performed by Minaev *et al.* suggested a defect with  $\langle 111 \rangle$  axial symmetry. Subsequent investigations by Weber *et al.* [135] verified this symmetry and identified the PL from the NP line as coming from an IBE. Weber *et al.* further made note of shifts in the main NP line characteristic of copper isotopes, demonstrating that the center was Cu-related. Like Mg, Cu in silicon is known to occupy both substitutional and interstitial sites. Weber *et al.* suggested a Cu<sub>i</sub>-Cu<sub>s</sub> pair center as the responsible defect based on an observed quadratic dependence of PL intensity on Cu concentration. Work by Istratov *et al.* [63] studying dissociation of the center, established that it was bound by more than just Coulomb interaction, requiring covalent bonds to match the observed binding energy. This eliminated the possibility that the center represented donor-acceptor pair.

Different models were proposed for the formation of the Cu defect [112, 95, 93, 94]. These include models with single-Cu and bond centered Cu with three bound Cu<sub>i</sub> impurities by Nakamura *et al.* An alternative proposed by Shirai *et al.* predicted three interstitial Cu<sub>i</sub> defects grouped in C<sub>3v</sub> symmetry about a single Cu<sub>s</sub> center. In addition Carvalho *et al.* proposed a formation pathway for this center via the capture of positively charged Cu<sub>i</sub> by the negatively charged Cu<sub>s</sub>. Later work by Steger *et al.* and Thewalt *et al.* [117, 118, 128] in isotopically enriched silicon firmly established the nature of this center as a Cu<sub>4</sub> defect. The IBE structure they observed included two primary ground state components  $\Gamma_4$  and  $\Gamma_3$ . Each of these contained complex fine structure of their own that was explained by different combinations of the two naturally occurring isotopes <sup>63</sup>Cu and <sup>65</sup>Cu in a Cu<sub>4</sub> complex.

In this work, we note that the fine structure of the isoelectronic Mg-pair center can be explained fully by grouping combinations of isotopes that have the same total atomic mass. This indicates that the positions of lines in its fine structure are determined only by isotope mass.

## 2.6 Spectral broadening mechanisms

Spectral lines resulting from defects in silicon are generally both homogeneously and inhomogeneously broadened. Homogeneous broadening commonly refers to the finite linewidth of spectral features determined by the lifetime of an excited state. In this case all defects contribute the same linewidth and center frequency, giving rise to a Lorentzian line-shape. By contrast, inhomogeneous broadening effects cause individual defects to contribute a range of peak frequencies and is often associated with a Gaussian line-shape [121]. There have however been cases in which a Lorentzian line-shape was observed for an inhomogeneously

broadened feature, as seen for the  $1s(A_1)$  to  $1s(T_2)\Gamma_7$  transition for Se in Si [91]. There are many sources of inhomogeneous broadening, including strain, electric and magnetic fields. The impact of those most relevant to our samples will be discussed here.

### 2.6.1 Isotope broadening

In their papers on isotope broadening in silicon, Karaiskaj *et al.* [74, 72] demonstrated a remarkable narrowing of spectral features for impurities like phosphorus, boron and lithium when diffused in isotopically enriched  $^{28}\text{Si}$ . Prior to this work, the relatively broad linewidths of transitions in  $^{\text{nat}}\text{Si}$  were considered consistent with the calculated predictions of Barrie and Nishikawa [98, 14]. Their work had suggested that the observed broadening was a consequence of phonon assisted transitions from higher excited states as they decayed to lower levels. Until the dramatic narrowing of spectral linewidths in  $^{28}\text{Si}$  was observed, it was therefore assumed that in high quality  $^{\text{nat}}\text{Si}$  samples all sources of inhomogeneous broadening had been largely eliminated. Purely lifetime limited, or homogeneously broadened features, generally have Lorentzian profiles with linewidth bounded by the uncertainty principle. This is given according to  $\tau\Delta E = \hbar/2$ , where longer lifetimes  $\tau$  imply a smaller uncertainty  $\Delta E$  and thus smaller linewidth for the feature. In practice of course there are always some sources of inhomogeneous broadening that prevent observation of this narrowest possible linewidth. Previous work had eliminated various sources of inhomogeneous broadening as the primary culprits, including electric field broadening, broadening due to strain generated by impurities and dislocations, and concentration broadening [65, 99, 105]. Ultimately Karaiskaj *et al.* [72] were able to show that thanks to the ground state wavefunction being relatively localized at the site of the impurity, the ground states of impurities in  $^{\text{nat}}\text{Si}$  are potentially very sensitive to changes in local environment. This means that, because any given impurity may have nearest neighbours that are  $^{28}\text{Si}$ ,  $^{29}\text{Si}$ , and  $^{30}\text{Si}$ , the ground state is broadened and shifted in  $^{\text{nat}}\text{Si}$  by  $\sim 0.01$  meV as is noted later experimentally. Higher excited states by contrast are much more diffuse, experiencing an environment comprising many unit cells across a much larger spatial extent of the crystal. These states thereby effectively see an isotopic composition much closer to the average, which for  $^{\text{nat}}\text{Si}$  is mostly  $^{28}\text{Si}$ . This means that the shift observed between sets of spectral lines in  $^{\text{nat}}\text{Si}$  and  $^{28}\text{Si}$  is consistent through all excited states.

Isotopic randomness in  $^{\text{nat}}\text{Si}$  was also shown by Karaisaj *et al.* [73] to account for the doublet splitting of the ground states of neutral acceptors in Si. This effect arose thanks to a partial lifting of degeneracy between the fourfold degenerate levels of the hole angular momentum  $j_h = 3/2$  ground state in the presence of random isotopic composition. This effect was notably absent, leading to singlets for the acceptor ground states in  $^{28}\text{Si}$ .

Since the inhomogeneous broadening generated by isotopic randomness depends on how tightly localized the ground state wavefunction is to an impurity, deeper centers, like magnesium and the chalcogens, are anticipated to be even more sensitive to host isotope broad-

ening effects than shallow donors like phosphorus. For centers like selenium and sulfur this narrowing of optical lines is a particularly dramatic effect, with for instance selenium in  $^{28}\text{Si}$  revealing fine structure sufficient to resolve hyperfine splitting of the  $1s(\text{A})$  to  $1s\text{T}_2$  transition [119, 91]. In magnesium as we will see, this narrowing is not so drastic, possibly as a consequence of its capacity to incorporate both interstitially as a double donor and substitutionally as a double acceptor. This gives rise to inhomogeneous broadening effects prevalent even in otherwise very pure samples.

## 2.6.2 Stark broadening

In many spectra presented in this work, we note that spectral lines in heavily compensated samples are much broader than in their lightly doped counterparts. This is a consequence of both linear and quadratic Stark broadening of spectral features. As detailed by [83, 64, 105, 101], potential energy  $V(r)$  for all ionized impurities throughout a crystal relative to a position  $r$  near a neutral donor, is given by,

$$V(r) = \frac{1}{4\pi\epsilon_0} \sum_i \frac{e_i}{\epsilon|R_i - r|} = \frac{1}{\epsilon_0} \sum_i \frac{e_i}{\epsilon R_i} \sum_{l=0}^{\infty} \sum_{m=-l}^l \frac{1}{2l+1} \left(\frac{r}{R_i}\right)^l Y_{lm}^*(\theta_i, \phi_i) Y_{lm}(\theta, \phi), \quad (2.38)$$

where  $e_i$  denotes the elementary charge of the  $i$ th ionized defect in a material of permittivity  $\epsilon$ . The  $i$ th center is located in spherical coordinates at  $R_i, \theta_i, \phi_i$  with coordinates of position  $r$  given by  $r, \theta, \phi$ . Taking just the  $l = 0$  term collapses this expansion to a simple shift of all energy levels by an amount  $4\pi \sum_i \frac{e_i}{\epsilon R_i}$ . The  $l = 1$  terms yield,

$$V(r) = -E(0)r, \quad (2.39)$$

with  $E(0)$  representing the electric field associated with  $V(r)$  evaluated at  $r = 0$ . Landau and Lifshitz [82] derive an expression for the linear and quadratic Stark shifts experienced by hydrogenic spectral lines in response to this field. This is written as,

$$\Delta = -\frac{R_y}{2n^2} + \frac{3}{2}n[n_1 - n_2]eEa^* - \frac{1}{16}n^4 [17n^2 - 3(n_1 - n_2) - 9m^2 + 19] (8\pi\epsilon)a^{*3}E^2. \quad (2.40)$$

The first term represents the unperturbed hydrogenic energy levels, the second, proportional to  $E$  represents the linear Stark effect and the third, proportional to  $E^2$  gives the quadratic shift. Integers  $n$  and  $m$  are the principal and magnetic quantum numbers respectively. Together with integers  $n_1$  and  $n_2$ , constrained to be greater than or equal to zero, and defined in relation to the principal and magnetic quantum numbers, the following relation is satisfied [82]

$$n = n_1 + n_2 + |m| + 1. \quad (2.41)$$

If we consider the case for  $2p_{\pm}$  which has a quadratic Stark shift, and no linear shift as seen from Eqs. 2.41 and 2.40, then we evaluate the above expression for  $n = n_1 + n_2 + |m| + 1 = 2 = 0 + 0 + |\pm 1| + 1$ . From this we find an anticipated Stark shift of,

$$- 78(8\pi\epsilon)a^{*3}E^2. \quad (2.42)$$

It is immediately apparent that this expression is always negative, and so will contribute only to shifts down in energy. This leads to a characteristic asymmetric broadening of the  $2p_{\pm}$  levels notable in the more heavily compensated samples discussed in this work. If by contrast we look at the  $m = 0$  state for  $n = 2$ , i.e.  $2p_0$  we find  $n = n_1 + n_2 + |m| + 1 = 2 = (1 \text{ or } 0) + (0 \text{ or } 1) + |0| + 1$ . This gives the following linear Stark shift experienced by this level,

$$\pm 3eEa^*. \quad (2.43)$$

Here it is clear that the linear broadening effect is symmetric, as indeed  $2p_0$  appears to be in the spectral lines we observe corresponding our low boron content (LB) samples. The  $2p_0$  transition does also have a quadratic Stark component, given as,

$$- 84(8\pi\epsilon)a^{*3}E^2. \quad (2.44)$$

While in LB samples this quadratic broadening may be small relative to the linear component, HB spectra containing the  $2p_0$  transition do reveal its impact. In these samples, the combination of linear and quadratic Stark effects are likely responsible for the observed symmetric broadening and slight asymmetric tail to low energy respectively. A number of studies [105, 101, 64] cite an average electric field  $\langle E \rangle$  at any substitutional site of,

$$\langle E \rangle \sim \frac{e}{\epsilon \langle r \rangle^2} \sim \frac{e}{\epsilon} N_I^{2/3}, \quad (2.45)$$

with  $\langle r \rangle$  the average distance between ionized impurities. It is also apparent from Eqs. 2.40 and 2.41 why we anticipate, and observe a lack of high excited states in heavily compensated samples. Both linear and quadratic Stark effects increase in strength with increasing  $n$ , leading to these levels becoming broadened to the point that they are no longer visible.

Higher order terms of Eq.2.38 give rise to further broadening effects, such as  $l = 2$  terms, which are responsible for field gradient broadening. This impact of this effect is discussed in detail by Larsen [84]. The contribution of  $l = 2$  terms is determined to be proportional to  $N_I$ . From Eqs. 2.45 and 2.40 it is seen that the linear and quadratic Stark shifts are proportional to  $N_I^{2/3}$  and  $N_I^{4/3}$  respectively. A quantitative assessment of the inhomogeneous line profiles

anticipated for the 1s-np transitions for donors in GaAs is also provided by Larsen [84]. The author assumes a random distribution of impurities, with resulting probability distribution for the electric field strength seen by any given neutral donor given by,

$$p(\epsilon) = \frac{2}{\pi} \epsilon \int_0^\infty dx [x e^{-\beta x^{3/2}} \sin(\epsilon x)]. \quad (2.46)$$

Here  $\beta = \frac{4}{15}(2\pi)^{3/2}$  and with  $\epsilon$  the electric field in units of  $en_I^{2/3}/\epsilon_0$ . The results of his analysis ultimately suggested that not all the observed broadening could be accounted for by a fully random distribution of impurities [83]. The discussion above has assumed such an uncorrelated distribution of ionized impurities. Naturally if our samples contain clusters of impurities the impact of Stark broadening on any given impurity from the surrounding random electric fields could be significantly greater. As discussed by Kal'fa *et al.* and Pajot [71, 101] the presence of both neutral and ionized charge species helps form a correlated distribution. Thanks to the tendency of neutral and ionized species to form pairs, the mean distance between charged and neutral impurities is reduced. In the case of an uncorrelated distribution this distance is  $N_I^{-1/3}$  while in a correlated distribution with both neutral and ionized charge species present it is given by  $(N_0/N_I^2)^{-1/3}$ .

In Fig. 2.7, we show how Stark broadening for dopant concentrations such as those seen in our experiments ( $\sim 10^{15}$  in our more heavily compensated samples) scales for the  $2p_0$  and  $2p_\pm$  transitions.

Naturally all these estimates represent an upper bound on the observable Stark shifts and broadening effects, since none of the information presented here accounts for the impact of the central cell potential. This will act to localize the valence electron more tightly than is accounted for by a simple Coulomb potential, resulting in decreased electric field sensitivity. Thanks to partial screening of the excited electron by the other, an excited valence electron in neutral magnesium will experience a greater electric field sensitivity than the single electron of the singly ionized species. According to Fig. 2.7, we predict a quadratic Stark shift of up to  $\sim 0.25$  meV for  $2p_0$  and  $2p_\pm$  at a dopant concentration of  $1 \times 10^{15} \text{ cm}^{-3}$ . Differences in peak positions of  $2p_0$  and  $2p_\pm$  features in HB samples relative to equivalents in LB samples, can be seen later in the Results sections. For  $\text{Mg}_i^0$ , the observed shifts between these features in HB vs. LB samples are closer to  $0.01 - 0.02$  meV.

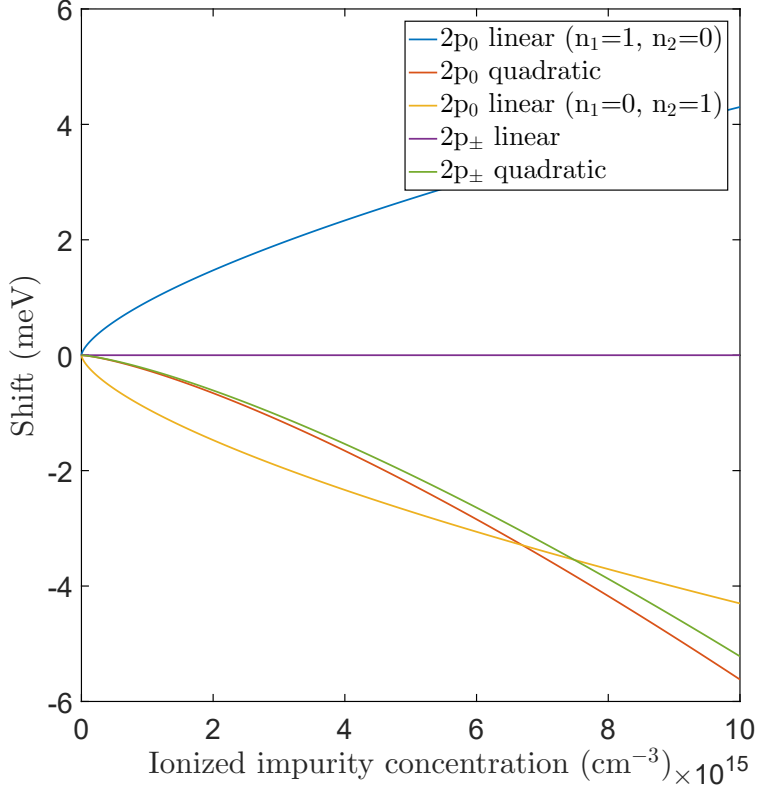


Figure 2.7: Anticipated Stark shifts for  $2p_0$  and  $2p_{\pm}$  as a function of ionized impurity concentration for an average electric field given by Eq.2.45.

### 2.6.3 Concentration broadening

Concentration broadening here refers to overlap of impurity ground and excited state wavefunctions in heavily doped materials. Calculations by Baltensperger [13] gave the following threshold defining where this effect becomes relevant, namely at a separation  $r_s$  given by,

$$r_s \sim 6na^*. \quad (2.47)$$

Here  $n$  is the principle quantum number,  $a^*$  the effective Bohr radius of the impurity, and  $r_s$  written in terms of,

$$\frac{4\pi r_s^3}{3} = \frac{1}{N_I} \quad (2.48)$$

for impurity concentration  $N_I$ . Our most heavily doped samples contain of order  $1 \times 10^{15} \text{ cm}^{-3}$  of boron and in theory up to as much singly ionized magnesium, though in practice since we see  $\text{Mg}_i^0$  in our spectra, it is clear not all the boron is compensating magnesium. As an approximation we can substitute value  $a^*$  as the effective Bohr radius cited by Kohn and Luttinger,  $a^* = a_0 \frac{\epsilon_r}{m^*/m_0} \sim 20 \text{ \AA}$ . For the excited state  $2p_{\pm}$ , for example, this implies that  $6na^* \sim 120 \text{ \AA}$ .

In turn this leads us to anticipate that the concentration broadening threshold lies at  $N_I \sim 1 \times 10^{17} \text{cm}^{-3}$ . Baltensperger's results would therefore lead us to conclude that we are well outside the regime in which concentration broadening has any impact. However as noted by Colbow [23], concentration broadening inconsistent with Baltensperger's calculations, which assume a regular lattice of impurities as opposed to a random distribution, has been seen in boron compensated silicon. Colbow's modifications to Baltensperger's theory were twofold. The first was to replace  $r_s$  with a term  $Xr_s$ , where  $X$  is a factor accounting for the reduced separation experienced on average thanks to a random, rather than regular distribution of impurities. Colbow's calculations determined this factor to be  $\sim 0.7$ . Second, the author notes that the effective Bohr radius  $a^*$  is poorly approximated by  $a^* = a_0 \frac{\epsilon_r}{m^*/m_0}$  for higher excited states. Based on experimentally determined energies of excited states, like the 2p levels, Colbow calculated larger effective Bohr radii using Eq. 2.12. Following these modifications Colbow found that concentration broadening could begin to be seen at a threshold of  $N_I \sim 3 \times 10^{15} \text{cm}^{-3}$  in boron doped silicon, much closer to the ranges seen in our HB samples.

#### 2.6.4 Broadening due to strain generated by point defects

Strain caused by point defects may also be relevant in our samples. This effect occurs for impurities that have atomic radii that are much larger or smaller than those of the atoms they replace [101]. Here I provide an overview of the impact this can have on spectral lines for some common and well studied contaminants in silicon like carbon and oxygen, which for our purposes are undesirable impurities. Discussions by Safonov *et al.* [110] and Davies *et al.* [30] treat the presence of carbon impurities in Si as a spherically symmetric perturbation written as,

$$u = \frac{A}{r^2}. \quad (2.49)$$

Here  $r$  is distance from the point defect and  $A$  is a constant describing the elastic mismatch between the impurity and the lattice. X-ray diffraction measurements carried out by Baker *et al.* [11] established that the fractional change in the silicon lattice constant,  $\Delta a/a$ , is correlated with the substitutional carbon concentration as,

$$\frac{\Delta a}{a} = -6.5 \times 10^{-24} [\text{C}]. \quad (2.50)$$

Here [C] is given in units of  $\text{cm}^{-3}$ . From this we see that the lattice parameter decreases with increasing carbon concentration. Similarly work by Takano *et al.* [125] demonstrated that the presence of the interstitial oxygen increases the lattice parameter according to,

$$\frac{\Delta a}{a} = 1.04 \times 10^{-24} [\text{O}], \quad (2.51)$$

with [O] given in units of  $\text{cm}^{-3}$ . For a perturbation with the form of  $u$ , each defect changes the crystal volume by an amount  $4\pi A$ . Additionally, Safonov *et al.* note that the change in crystal volume is further influenced by the presence of image forces [110]. These are effects that occur because the size of the crystal is finite and at the surface, positive charges are induced by the presence of negatively charged electrons. This additional change in volume is written by Safonov as,

$$\Delta V = 8\pi A(1 - 2\sigma)/(1 + \sigma). \quad (2.52)$$

Here  $\sigma$  is Poisson's ratio, which may be estimated based on the average ratio of perpendicular to parallel uniaxial strain components for each of the different crystal directions. With all effects included, the total measured  $\Delta a/a$  can then be written as,

$$\frac{\Delta a}{a} = 4\pi A[C](1 - \sigma)/(1 + \sigma). \quad (2.53)$$

This combined with the known scaling of  $\Delta a/a$  with impurity concentration allows the parameter  $A$  to be determined.  $A$  is then incorporated into the strain calculation, with the stress tensor having components given by,

$$e_{ij} = \frac{A}{r^3} \left( \delta_{ij} - 3 \frac{(x_i - p_i)(x_j - p_j)}{r^2} \right), \quad (2.54)$$

where an impurity at point  $(x_1, x_2, x_3)$  exerts a strain at point  $(p_1, p_2, p_3)$ . From this, as outlined by Stoneham [121] and later by Davies [28], one can determine a strain-broadened linewidth. Davies assumes a random distribution of Si isotopes and calculates a broadening of  $\sim 0.018 \text{ meV}$  for a silicon luminescence feature called the 'G-line' which occurs at  $969 \text{ meV}$  with  $[\text{O}] \sim 10^{18} \text{ cm}^{-3}$ . This calculated broadening is somewhat lower than the experimentally observed value of  $\sim 0.03 \text{ meV}$  seen for this feature. The discrepancy is likely a consequence of a correlated, rather than truly random distribution of oxygen impurities [28]. Similarly for carbon, Safonov *et al.* [110] calculate strain broadened line-shapes for the no-phonon bound exciton transition of phosphorus. The authors perform these computations for several samples with a range of carbon concentrations. The lowest, with  $[\text{C}] < 10^{16} \text{ cm}^{-3}$  leads to a  $6.2 \mu\text{eV}$  broadening. Two others with  $[\text{C}] = 5 \times 10^{17}$  and  $[\text{C}] = 7 \times 10^{17} \text{ cm}^{-3}$  correspond to a broadening of  $15 \mu\text{eV}$  and  $20 \mu\text{eV}$  respectively. While our samples are expected to contain relatively little carbon or oxygen, strain broadening may still have an appreciable impact, in particular through the presence of boron in our more heavily compensated samples.

## Chapter 3

# Samples and apparatus

### 3.1 Fourier transform infra-red (FTIR) spectroscopy

Most data seen in this work was collected using an FTIR spectrometer. This device is comprised of a Michelson interferometer with one mobile and one stationary mirror arm. Light, whether from a broadband IR source or PL from a sample, is split between the two mirror arms by a beamsplitter before being passed down each arm and travelling back to recombine at the beamsplitter. In absorption measurements, light is then passed through a sample and falls onto a detector. In PL measurements, light is passed directly to the detector after the beamsplitter. In Fig. 3.1 we include a basic schematic that details the important features of our FTIR spectrometer.

At the zero-path length difference (ZPD) between the two mirror arms all wavelengths from the broadband source are in phase and we see a maximum in signal intensity commonly referred to as the centerburst. At each position of the mobile mirror arm away from the ZPD additional components are collected with different wavelengths in and out of phase, yielding frequency contributions that do not all constructively interfere as at the centerburst. This scanning of the mobile arm can be done with greater or lesser resolution by stepping the mirror a greater or lesser distance down its path. The data for one full scan of the mobile mirror arm comprises the interferogram which is converted to a spectrum via Fourier transform. By this method all wavelength components are effectively measured together rather than scanning over them individually. This leads to a large speedup in measurement time as well as increased sensitivity due to the additional averaging that takes place over other devices such as grating spectrometers. Additionally, an FTIR spectrometer is generally very internally consistent, with positioning of the mobile mirror arm determined with high precision based on counting fringes of a frequency stabilized laser. This calibration laser passes through the interferometer and is directed to a dedicated detector. The resulting sinusoid is a very accurate measure of the difference in optical path length between the two interferometer arms.

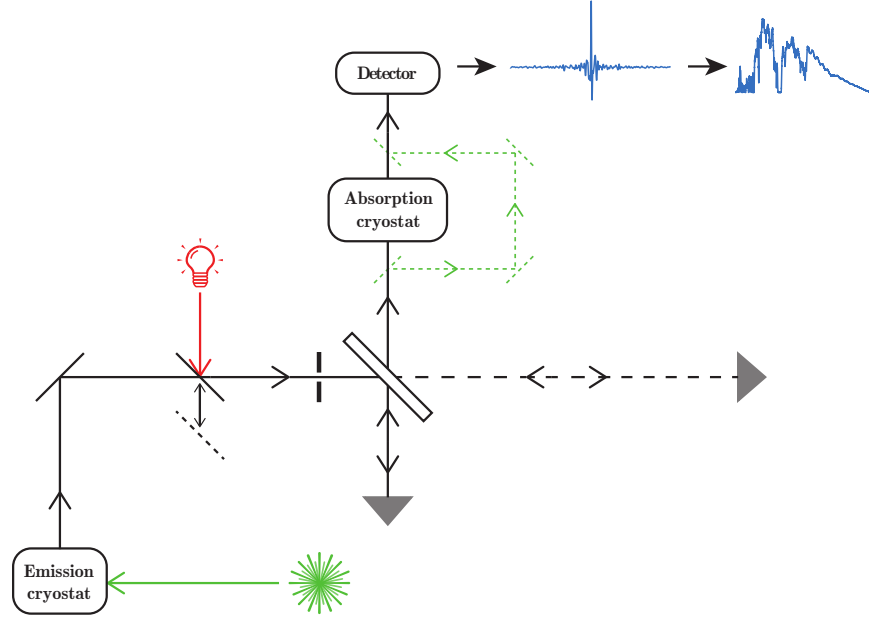


Figure 3.1: Here we show a schematic diagram for our Bruker FTIR spectrometer. For absorption measurements, which make use of a broadband IR source such as a quartz lamp, light is split down two mirror arms by a 50-50 beamsplitter and travels back along the same path to subsequently recombine at the beamsplitter. The beam then passes through a sample and onto a detector. The resulting interferogram undergoes a Fourier transform and other processing steps to be turned into a spectrum. For PL measurements, an external pump laser is used to excite the sample, which effectively then becomes the IR source. The spot size of the beam is limited by an aperture wheel with a range of circular openings varying in size from 0.5 to 12.5 mm. This is indicated as a broken line perpendicular to the optical axis, prior to the beamsplitter.

Broadly, there are two kinds of experiment we perform with the instrument, absorption and emission. In absorption measurements, the broadband IR source indicated by the red light-bulb in Fig. 3.1 is coupled into the instrument and passed through the sample. In emission, an external excitation source, usually one of a variety of lasers, is used to excite the sample. The sample then luminesces, and that light is coupled into the instrument, effectively becoming the source for the interferometer.

Data processing intrinsic to the instrument/FTIR measurement technique involves several steps, including correction of phase error, zero-padding, apodization and accounting for non-linearity in detector response. In an ideal interferometer all mirrors and beam splitters send precisely equal amounts of power down each arm. In practice this is of course not true and these imperfections, leading to phase errors, must be accommodated in the instruments' interferogram to spectrum calculation, accomplished via the Fast Fourier Transform (FFT) algorithm.

Consider beams of monochromatic light  $E_1 = E_0 \exp(2\pi i\nu t)$  and  $E_2 = E_0 \exp(2\pi i\nu(t + \delta))$  propagating down two arms of an interferometer. Here a path length difference  $x = c\delta/2$

introduces a delay between the arms, where the factor of two accounts for travel of the beam in both directions prior to recombining at the beamsplitter. The quantities  $\nu$  and  $E_0$  represent frequency and the initial intensity incident on the beamsplitter respectively. Interference between these two beams means that the intensity of the EM field present seen at the detector,  $I = |E|^2 = |E_1/2 + E_2/2|^2$ , will have the following form.

$$I = \frac{1}{2}I_0(1 + \cos(2\pi\nu\delta)). \quad (3.1)$$

This is readily extended to an infinite series of monochromatic sources, i.e. a broadband source by integrating over all frequencies  $\nu$ , such that,

$$I = \frac{1}{2} \int_0^\infty S(\nu)(1 + \cos(2\pi\nu\delta)) d\nu, \quad (3.2)$$

where  $S(\nu)$  is the power spectrum of the source. This represents the ideal case for an interferometer with perfect optical components and subsequently no phase error. As detailed by Porter *et al.* [104], the interferogram itself is then calculated as the difference between the intensity  $I(\delta)$  at any time delay  $\delta$ , and the quantity  $I(\infty)$ , the signal intensity at large path length difference. This quantity is normalized by the intensity at zero delay, i.e. at the ZPD.

$$\gamma(\delta) = (I(\delta) - I(\infty)) / I(0). \quad (3.3)$$

Through the inverse cosine Fourier Transform (FT) of  $\gamma(\delta)$  we can then determine the normalized power spectrum  $P(\nu) = S(\nu)/I(0)$ .

$$P(\nu) = 2 \int_0^\infty \gamma(\delta) \cos(2\pi\nu\delta) d\delta. \quad (3.4)$$

The ideal interferogram is a symmetric quantity, i.e.  $\gamma(\delta) = \gamma(-\delta)$ , so we can extend the integral across negative frequencies and the full complex inverse FT and achieve the same result, i.e.,

$$P(\nu) = \int_{-\infty}^\infty \gamma(\delta) \exp(-2\pi i\nu\delta) d\delta. \quad (3.5)$$

In practice, for a real interferometer, there is some phase difference between the two arms due to imperfect optical components etc. that must be accounted for. The true signal at the detector is in this case written as [104],

$$I = \frac{1}{2} \int_0^\infty S(\nu)(1 + \cos(2\pi\nu\delta + \phi(\nu))) d\nu, \quad (3.6)$$

with  $\phi(\nu)$  the  $\nu$ -dependent difference in phase between the interferometer arms. In this case the power spectrum  $P(\nu)$  is extracted by inverse FT as,

$$P(\nu) \exp(i\phi(\nu)) = \int_{-\infty}^{\infty} \gamma(\delta) \exp(-2\pi i\nu\delta) d\delta. \quad (3.7)$$

There are a number of ways to account for phase error. The first, known as the Mertz phase correction algorithm [88], is achieved by multiplying by the factor  $\exp(-i\phi(\nu))$ . This relies on the assumption that the phase factor  $\phi(\nu)$ , which is calculated by a short scan to either side of the ZPD, is relatively slowly varying. The interferogram is also multiplied by a ramp function with values between 0 and 1 with magnitude 0.5 at the ZPD. This is used to prevent double counting of data on either side of the centerburst [21] and intrinsically assumes a fully symmetric interferogram. An alternative method, discussed by Forman *et al.* [38], eliminates phase error by convolving the FT of  $\exp(-i\phi(\nu))$  with the interferogram after  $\phi(\nu)$  is determined by the same short scan about the ZPD. Of these two methods, a review conducted by Chase [21] determined that the convolution method yields more accurate phase correction, however Chase also notes that the Mertz algorithm is faster. For our purposes, Mertz phase correction is sufficient, and the phase of our interferometer is noted to be very constant as a function of frequency.

A third method [24] eliminates the phase by calculating the magnitude  $|P(\nu) \exp(i\phi(\nu))|$  to determine the power spectrum. This becomes the sum in quadrature of real  $P(\nu) \cos(\phi(\nu))$  and imaginary  $P(\nu) \sin(\phi(\nu))$  components. This method utilises an equal scan to either side of the ZPD to obtain the full double sided interferogram.

Phase resolution on the interferometer is limited by the amount of room the mobile mirror arm has to scan in equal increments in both directions past the ZPD. For our instrument, this distance is  $\sim 35$  cm, giving us a maximum attainable phase resolution of  $\sim 0.017 \text{ cm}^{-1}$ .

Limits on the spectral resolution of the interferometer are imposed by the length of the mobile-mirror path interferometer arm in one direction past the ZPD. This determines how much of the interferogram is effectively measured, with longer travel distances sampling more information and giving higher resolution. Even a spectral feature of infinitesimally small width must have a non-zero FWHM since it is convolved with the instrument response. The finite distance traversed by the mobile mirror is equivalent to multiplying the interferogram by a square wave. The smallest possible linewidth for a delta-function like feature, and thus the resolution of the spectrometer, is seen for this so-called boxcar apodization. Taking the Fourier transform of a boxcar function yields a sinc function. The result is a spectrum, as detailed by Kauppinen *et al.* [75], in which a delta-function like feature appears as a sinc function with FWHM given by,

$$\text{FWHM} = \frac{1.207}{2\Delta}. \quad (3.8)$$

Here,  $\Delta$  is the maximum path length difference of the instrument. For our apparatus this path length is in excess of 3.5 m, giving our instrument a theoretical maximum resolution of

0.001 65  $\text{cm}^{-1}$ . Because of the shape of the sinc function, boxcar apodization also introduces fringes around sharp spectral lines. These can be suppressed by use of other apodization functions, such as the Blackman-Harris window, which is a sum of multiple cosine terms. This sacrifices minimum linewidth in favour of eliminating fringing. We use a three-term Blackman-Harris apodization function since in our case none of the spectral features of magnesium are expected to come close to challenging the resolution of our interferometer.

In practice of course, one cannot extend the resolution of an FTIR instrument indefinitely simply by extending the path of the mirror arm. Larger apertures limit resolution by allowing through a greater proportion of light rays that travel off the main axis. Higher resolution scans necessitate smaller and smaller apertures, meaning that were we to extend the mirror arm out indefinitely the aperture to accommodate scans of arbitrarily high resolution would be arbitrarily small.

Implementing the FFT algorithm requires that the number of data points in the interferogram be a power of two. To this end we set a zero-filling factor that pads the number of data points in the interferogram to a specified order of two. This has the effect of making the transformed spectrum look smoother and can make fitting easier, though it of course has no impact on resolution, which is set primarily by how far the mirror arm scans down the mobile path.

Post-processing of data, external to the instrument, is also usually performed. This can include background subtraction, removal of fringes caused by internal reflections in samples or dewar windows. Conversion factors are often applied to account for sample thickness and generate spectra in units of absorption coefficient ( $\text{cm}^{-1}$ ). Removal of background and fringing effects is generally done by fitting. However in extreme cases, non-critical sections of the interferogram that display obvious extraneous frequency components can be removed directly by linear interpolation between two points on either side of the feature in question. Relatively fringe-free spectra can then be recovered by re-transforming the processed interferogram. While this procedure generally removes the majority of fringing, some ringing effects, particularly near sharp features, are inevitable.

Our Bruker IFS 125HR Fourier transform infrared (FTIR) spectrometer makes use of three different IR sources with wavelength ranges in the near (NIR,  $\sim 4000\text{-}10000 \text{ cm}^{-1}$ ), mid (MIR,  $\sim 400\text{-}4000 \text{ cm}^{-1}$ ) and far infra-red (FIR,  $< 400 \text{ cm}^{-1}$ ). These sources are focussed through a variable aperture wheel allowing spot sizes varying between 0.5 and 12.5 mm to illuminate a sample. Two liquid He-immersion dewars are integrated with the spectrometer for separate use in absorption measurements, which make use of the internal IR light sources, and emission for which we make use of a variety of external lasers to excite the sample, leaving the PL signal produced by the sample to act as the light source for the instrument. Depending on the wavelength range of interest a number of beamsplitters can be used including  $\text{CaF}_2$ , KBr, and Mylar, which cover the NIR, MIR and, FIR regimes

respectively. Both arms of the interferometer have corner cube reflectors constructed of gold-plated mirrors, one in fixed position, the other on a mobile stage.

Before any measurement takes place, the instrument is pumped down to a stable vacuum of at least 0.01 hPa to minimize the presence of water vapour lines, many of which are prominent in the mid-IR range. This never removes them entirely, but as long as the pressure is low and, more critically, stable, water lines are effectively removed when a sample spectrum is divided by a reference taken with no sample in position. In absorption we use detectors ranging from mercury-cadmium-telluride (MCT) for mid infra-red detection ( $450\text{-}5000\text{ cm}^{-1}$ ) and a LHe-cooled bolometer for studies of shallow donor regions ( $<800\text{ cm}^{-1}$ ). For PL detection we use Ge-diode ( $6000\text{-}12000\text{ cm}^{-1}$ ) and InSb ( $1850\text{-}12000\text{ cm}^{-1}$ ) liquid nitrogen cooled detectors.

## 3.2 Magnesium diffusion in silicon

Here we summarize work of Shuman *et al.* [113, 114] which established parameters for Mg diffusion in Si in the  $600\text{-}1200^\circ\text{C}$  temperature range. These authors provided us with the samples used in the work described in this thesis.

An initial study of Mg-diffusion in the relatively low temperature,  $600\text{-}800^\circ\text{C}$  range, established parameters for the creation of magnesium-diffused silicon from an ion-implanted surface layer that served as the source [114]. The implanted layer of silicon is rendered amorphous as a result of damage from ion-implantation. Then during the anneal, recrystallization of the amorphous layer to form a single crystal causes the magnesium to diffuse into the bulk crystal. In their process, Shuman *et al.* used samples with Mg ion-implanted at an energy of 150 keV. The depth of the  $p - n$  junction after diffusion was used to determine the diffusion coefficient  $D_{Mg}$ . Shuman *et al.* determined that the diffusion profile was approximately Gaussian based on the results of secondary-ion mass spectroscopy (SIMS) measurements. In this case  $D_{Mg}$  could be written as,

$$D_{Mg} = \frac{x^2}{4t \ln[N_s(t)/N_{Mg}]}, \quad (3.9)$$

where  $x$  is the  $p - n$  junction depth,  $t$  is the diffusion time,  $N_s(t)$  is the concentration of  $\text{Mg}_i$  in the ion-implanted surface layer after time  $t$  and  $N_{Mg}$  is the concentration of  $\text{Mg}_i$  at the  $p - n$  interface. Further, based on anneals performed at a number of temperatures in between  $600\text{-}800^\circ\text{C}$  the authors fit their data to the following Arrhenius relation,

$$D_{Mg} = 32.0 \exp(-E_a/k_B T). \quad (3.10)$$

Here  $k_B$  is Boltzmann's constant,  $E_a = 1.98\text{ eV}$  is the activation energy, and  $T$  is temperature. The high diffusion rate of Mg in silicon is noted to be characteristic of interstitial impurities.

In a second study encompassing the higher temperature regime 1000-1200°C, Shuman *et al.* combine their previous results for the 600-800°C range with new data to establish an Arrhenius curve for the full 600-1200°C range. In this case magnesium was diffused into silicon by the sandwich diffusion method. In this procedure, a thin layer of high purity magnesium was evaporated onto the faces of the silicon sample and thinner silicon plates that were placed on either side. The plates were effectively welded to the sample by the high temperatures of the anneal that followed, preventing magnesium from escaping by evaporation. The extra silicon from the top and bottom plates were later ground off.

The magnesium diffusion profiles for these experiments were best described by a complementary error function. This is characteristic of diffusion from an infinite source, in which the surface concentration remains effectively fixed throughout the process. Magnesium concentration  $N_{Mg}(x, t)$  as a function of depth from the surface  $x$  and diffusion time  $t$  is written for this case as,

$$N_{Mg}(x, t) = N_s \operatorname{erfc} \left( \frac{x}{2\sqrt{D_{Mg}t}} \right). \quad (3.11)$$

Here,  $N_s$  is the surface concentration, which is taken to be fixed during diffusion. To characterize  $N_{Mg}(x, t)$ , material was removed from a sample in 20  $\mu\text{m}$  increments and resistivity was measured before and after with a four-point probe measurement. The resistivity as a function of depth was used to calculate the  $\text{Mg}_i$  concentration profile. By fitting all available data in the 600-1200°C range, Shuman *et al.* also obtained the following Arrhenius relation,

$$D_{Mg} = 5.3 \exp(-E_a/k_B T), \quad (3.12)$$

where the activation energy is  $E_a = 1.83 \text{ eV}$ . Fits with  $D_{Mg}$  as a fit parameter gave rise to the theoretical curves seen in Fig. 3.2 for fixed temperature  $T = 1000^\circ\text{C}$  and fixed diffusion time  $t = 1800 \text{ s}$ , data for which is seen in [113] by Shuman *et al.* The authors note that some lithium contamination is present that they were unable to eliminate. This is visible in this work in absorption spectroscopy through the signatures of lithium and lithium-oxide donors seen in the shallow donor region as will be detailed later.

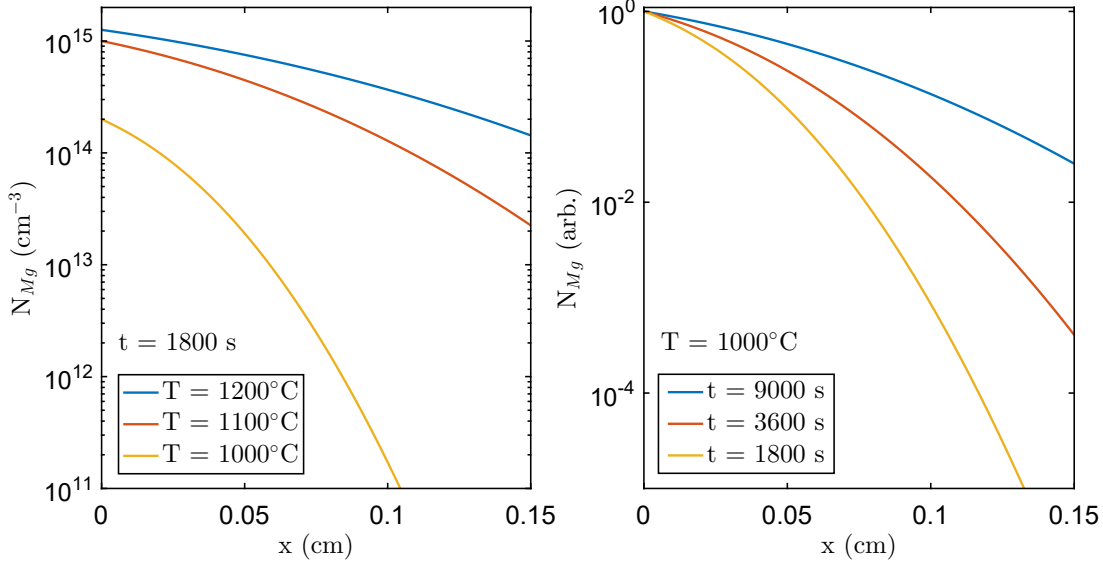


Figure 3.2: Magnesium concentration profiles as a function of junction depth  $x$  for constant temperature (left) and constant diffusion time (right). The constant time curves are presented in units of  $\text{cm}^{-3}$  with initial surface concentrations  $N_S$  as seen in Shuman *et al.* [113]. The y-axis of the constant temperature curves are presented in normalized units with a diffusion constant  $D_{Mg} = 2.5 \times 10^{-7}$ . All other parameters, including  $D_{Mg} = 2.5 \times 10^{-7}$ ,  $1.2 \times 10^{-6}$ , and  $2.5 \times 10^{-6} \text{ cm}^2 \text{ s}^{-1}$  for  $T = 1000$ ,  $1100$ , and  $1200^\circ\text{C}$  respectively in the isochronic curves are taken directly from Shuman *et al.* [113].

### 3.3 Absorption

In this study we worked with four float-zone grown diffused Si:Mg samples. These included two relatively high boron content  $^{28}\text{Si}$  and  $^{\text{nat}}\text{Si}$  samples with boron concentrations of  $1.8 \times 10^{15} \text{ cm}^{-3}$  and  $2.2 \times 10^{15} \text{ cm}^{-3}$  respectively ( $^{28}\text{Si}$  HB and  $^{\text{nat}}\text{Si}$  HB), and two undoped low boron content  $^{28}\text{Si}$  and  $^{\text{nat}}\text{Si}$  samples ( $^{28}\text{Si}$  LB and  $^{\text{nat}}\text{Si}$  LB) containing approximately  $4 \times 10^{13} \text{ cm}^{-3}$  and  $1 \times 10^{13} \text{ cm}^{-3}$  of boron respectively. The properties of the  $^{28}\text{Si}$  LB material have been detailed elsewhere [32]. Both  $^{28}\text{Si}$  samples were enriched to 99.995%  $^{28}\text{Si}$ . Our sample growers estimate approximate Mg concentrations of  $2 \times 10^{14} \text{ cm}^{-3}$  and  $7 \times 10^{14} \text{ cm}^{-3}$  for the  $^{28}\text{Si}$  and  $^{\text{nat}}\text{Si}$  LB samples respectively. Samples compensated with different concentrations of the single-acceptor boron provide us with a way to maintain stable quantities of the neutral and singly-ionized Mg species. Our absorption results focus primarily on these four samples.

All absorption measurements were performed using a Bruker IFS 125HR Fourier transform infrared (FTIR) spectrometer. Samples were mounted in a liquid helium cryostat with either polypropylene or ZnSe windows. Strain free mounting techniques, in which samples were recessed inside holders that held them loosely, were employed with a variety of sample holders depending on the geometry of the individual sample. Spectra were collected at pumped helium, sub-lambda temperatures for all absorption and luminescence mea-

measurements, except where noted. For infrared absorption spectra, a KBr or coated Mylar beam-splitter was used, with a liquid nitrogen-cooled mercury cadmium telluride detector when studying  $\text{Mg}_i^0/\text{Mg}_i^+$  centers, and a 4.2 K silicon bolometer with an  $800\text{ cm}^{-1}$  low-pass cold filter for studying the shallow donor region.

To improve our signal from shallow donor features, we made use of above band-gap illumination through the appropriate broad-band near infrared (NIR) source in our interferometer to generate free carriers that photoneutralize ionized boron acceptors and shallow donors. In Fig. 3.3 we see this behaviour for the HB samples. Spectral features associated with B and a center discussed later which we identify as an Mg-B complex are all greatly enhanced under illumination by our NIR as opposed to mid infrared (MIR) source.

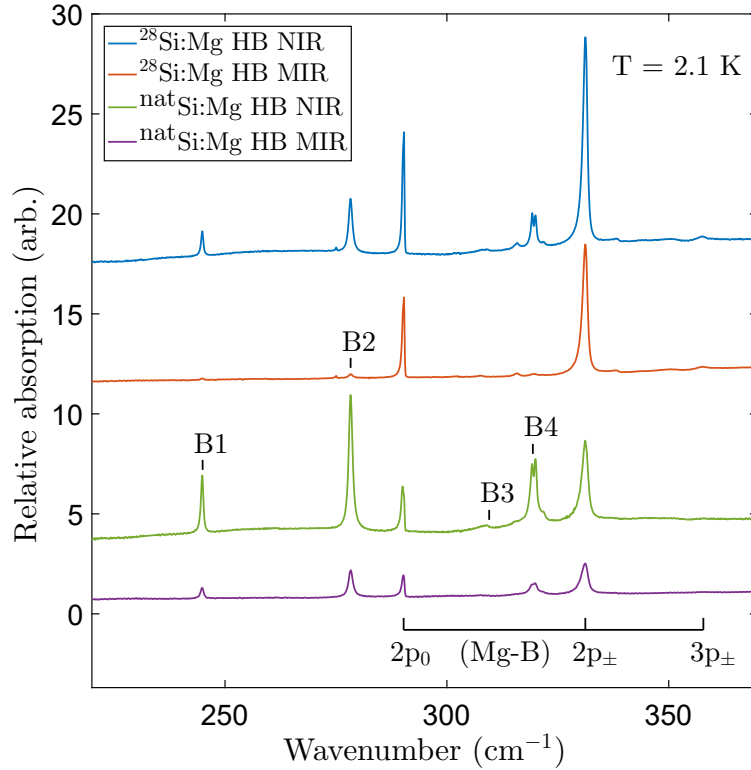


Figure 3.3: Demonstration of above band-gap light (NIR source) generating stronger absorption lines for both Mg-B and B centers than when spectroscopy is performed without above band-gap light (MIR source). This is due to photoneutralization of ionized donors and acceptors by free holes and electrons. Spectra were collected at  $T = 2.1\text{ K}$  with  $0.1\text{ cm}^{-1}$  ( $\sim 0.012\text{ meV}$ ) resolution.

To remove surface strains samples were etched in a 10:1  $\text{HNO}_3:\text{HF}$  solution for about 5 minutes. Where possible, wafer samples were wedged to prevent thin film interference fringes appearing in final spectra.

### 3.4 Photoluminescence/Raman

Emission measurements allow us to study a range of features not detectable in absorption. These include bound exciton transitions in photoluminescence and transitions which are forbidden in absorption spectroscopy by using Raman spectroscopy. These latter measurements tend to have complementary selection rules to those seen in absorption. Details of which transitions are allowed vs. forbidden in absorption and Raman measurements are included in the appendices. In these studies we worked with a float-zone grown diffused  $^{28}\text{Si}:\text{Mg}$  sample, referred to in absorption measurements and in our previous work [1] as the  $^{28}\text{Si}$  LB sample. Our boron acceptor compensated samples were also investigated. As with absorption, all photoluminescence measurements were performed using our Bruker IFS 125HR FTIR spectrometer with a  $\text{CaF}_2$  beam-splitter. For the  $^{28}\text{Si}:\text{Mg}$  studies samples were mounted in a liquid helium cryostat with fused silica windows. Photoluminescence signals were generated using 1030 nm and 1047 nm excitation sources for high resolution scans of the IBE and temperature dependence PL measurements respectively. Light was detected with a liquid nitrogen cooled Ge detector. Scattered excitation light was removed by sharp cut long-pass filters. For PL measurements at temperatures above 4.2 K, the sample was lightly held against a temperature-controlled Cu plate cooled in flowing He gas. For the high resolution isotopic fingerprint PL scans an apodized instrumental resolution of 0.0031 meV full width at half maximum (FWHM) was used, while a lower resolution of 0.12 meV FWHM was used for the temperature dependence study, since for these studies lower excitation levels were necessary to minimize sample heating when the sample was not immersed in liquid He. Raman spectroscopy was also performed in an effort to observe the IR forbidden  $1s(A_1)$  to  $1s(E)$  transition. This data was collected with below band-gap 1081 nm excitation. Sample and detector conditions were the same as for PL measurements.

Separately, measurements of photoluminescence lifetimes were made using an SR430 multichannel scaler, coupled to a Hamamatsu H10330A-25 photon counting detector to detect light passed through a double diffraction grating spectrometer. A 980 nm laser was used as the excitation source for these measurements.

## Chapter 4

# Absorption results

Results are presented in the following order. First I discuss our spectra displaying the well known  $\text{Mg}_i^0/\text{Mg}_i^+$  donor transitions and show a number of higher excited states for each not seen prior to this work. Second I present our study of the  $\text{Mg}_{i*}^0/\text{Mg}_{i*}^+$  transitions first documented by Ho [60, 61], which we interpret to represent Mg complexing with some other species or possibly inhabiting an interstitial site other than the usual  $T_d$ . Here we also note the presence of yet another set of lines also previously seen in [60, 61] which appear to be thermally induced transitions from low lying levels near the  $\text{Mg}_{i*}^0$  ground state. The labelling scheme adopted by Ho [60, 61] for lines “1”-“6” and “a”, “b” is maintained in all figures where those transitions are visible together with our own identifications. Third we detail our observations of a new shallow donor species seen in absorption and photoluminescence which we interpret as a magnesium-boron (Mg-B) complex.

In each figure I choose spectra that best display the features relevant to each plot, i.e. successive plots are not necessarily different segments of the same spectra. Peak positions listed in Tab. 4.3 and 4.5 are obtained from fits to spectra that best show the specific feature in question. Most spectra are presented in absorption coefficient units ( $\text{cm}^{-1}$ ) to account for differences in sample thickness. This was done by measuring the spectral height of the TA+TO two-phonon absorption feature intrinsic to silicon at  $\sim 78$  meV in undoped  $^{\text{nat}}\text{Si}$  and  $^{28}\text{Si}$  samples of known thickness. That height was then used to determine a conversion factor later applied to measurements in Mg-doped silicon, based on the heights of the corresponding phonon features in those spectra. This was necessary since steps taken to avoid interference fringes in spectra meant the effective optical path length through a sample could not always be taken directly from the thickness of that sample. For instance in absorption, wafer samples were often oriented such that light was incident at non-normal incidence to spatially separate light transmitted directly through the sample from that arising from multiple internal reflections. Often this was sufficient to suppress the fringing entirely or at least to reduce it and alter the phase. In the latter case fringes with different phase but approximately the same frequency for each scan could be averaged appropriately such that fringes added destructively, eliminating a majority of interference effects. Primary

sources of thin film interference included the silicon itself, when working with wafer samples that were too thin to wedge, and the dewar windows, of which one set were un-wedged ZnSe.

Fits to all features, where applicable, are made using mixed Gaussian-Lorentzian peaks. These are a standard approach taken to approximate a Voigt profile, i.e. the convolution of Gaussian and Lorentzian profiles given by

$$V(\nu) = \int_{-\infty}^{\infty} G(\nu')L(\nu - \nu')d\nu', \quad (4.1)$$

with Gaussian profile,

$$G(\nu) = \frac{A}{\gamma} \sqrt{\frac{4\ln 2}{\pi}} \exp \left[ -4\ln 2 \left( \frac{\nu - \nu_0}{\gamma} \right)^2 \right], \quad (4.2)$$

and Lorentzian,

$$L(\nu) = \frac{2A/\pi\gamma}{1 + 4[(\nu - \nu_0)/\gamma]^2}. \quad (4.3)$$

However the form of Eq. 4.1 has no analytical solution. So instead we work with peak fits of the form,

$$V(\nu) = fL(\nu) + (1 - f)G(\nu), \quad (4.4)$$

with fraction  $f$  denoting the weighting assigned to Lorentzian component  $L(\nu)$  and Gaussian component  $G(\nu)$ . These are known to constitute a reasonable approximation to the Voigt profile [66] and are widely used in spectroscopy to characterize spectral lines.

In some cases, often as a consequence Stark broadening of some features, we note line-shapes that are asymmetric. In these cases we adopt a modified version of Eq. 4.4 for fitting. In these situations,  $\gamma$  which normally specifies linewidth, is used to account for asymmetry seen in, for example, the isotopic fingerprint of the Mg-pair IBE. This is taken to have a frequency dependence given by,

$$\gamma(\nu) = \frac{2\gamma_0}{1 + \exp[a(\nu - \nu_0)]}, \quad (4.5)$$

as detailed by Aaron *et al.* [115]. When incorporated into Eq. 4.4, we find that positive values of  $a$  will correspond to peaks with a tail to low energy and negative values will result in a tail to high energy.

All peak energies determined from fits are assumed to carry an uncertainty of  $\pm 0.01$  meV unless otherwise specified. For all figures, spectra are presented from top to bottom in the order specified in the legend. Scaling factors associated with a given spectrum indicate that a trace has been multiplied by the listed value as indicated.

Illumination conditions on samples were variable since our apparatus did not keep our samples in the dark and relies on broad-band IR illumination to perform spectroscopy. We

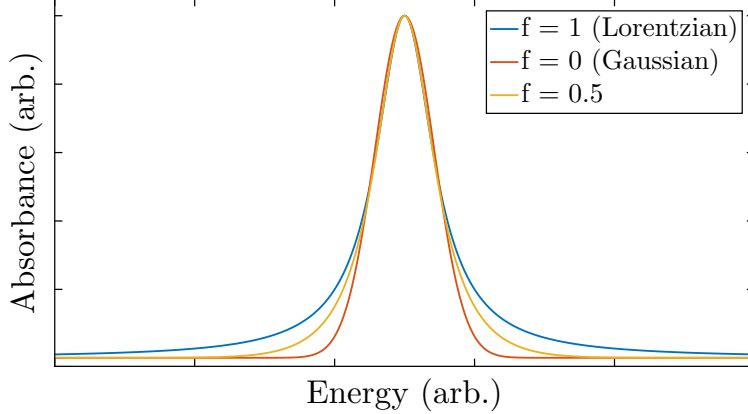


Figure 4.1: Here we see Eq. 4.4 evaluated for identical parameters except for the weighting factor  $f$  which is given values that yield a pure Gaussian, Lorentzian and a 50/50 mixture of the two.

were not able to reproduce the results of Baxter and Ascarelli [15] which suggested that we should be able to photoconvert  $T_d$  magnesium interstitials to  $C_{3v}$  with sufficient power from an IR laser. We attempted this with up to 30 mW of power, supplied with an IPG photonics IR laser at  $2.2 \mu\text{m}$ .

In addition to looking for evidence of a photoconversion effect between interstitial sites, that we had anticipated would strengthen the  $\text{Mg}_{i^*}$  spectral lines, we looked for bleaching of these same features at temperatures beyond 14 K. This would also be characteristic of the alternate interstitial site discussed by Baxter and Ascarelli, who predicted a rapid increase in the rate of decay from  $\text{Mg}_{i^*}$  to  $\text{Mg}_i$  above this temperature [15]. No such bleaching was observed and in combination with other evidence detailed later, this has led us to believe that  $\text{Mg}_{i^*}$  represents a complex rather than an alternate interstitial site.

## 4.1 $\text{Mg}_i^0$ and $\text{Mg}_i^+$ donor spectra

Here we display absorption data showing lines previously seen [39, 59, 58, 56, 57, 60, 61] for the standard  $\text{Mg}_i$  center and a number of newly resolved higher excited states. We observe no sign of  $\text{Mg}_i$   $1s(A_1)$  to  $1s(T_2)$  transitions for the neutral/ionized species. Calculations by Altarelli [5] of binding energies for excited states of singly-ionized double donors in silicon suggest a binding energy of 155 meV for  $1s(T_2)$ . For the case of  $\text{Mg}_i^+$  this would lead us to anticipate  $1s(T_2)$  appearing in the  $\text{Mg}_i^0$  region. It may be that measurements performed by Ho and Ramdas [59], who anticipated observing this level between 107 and 135 meV, were measuring in the wrong spectral region to see it. Magnesium, while a relatively deep donor, is not as deep as chalcogens like,  $\text{Se}^+$  (593 meV) [91, 119], for which these transitions are very strong. As a result, transitions within the ‘s’ states are likely better approximated by EMT and so more strongly forbidden. It is also possible that for Mg, these transitions are allowed but have very short lifetimes and are too broadened to observe. It is likely that to

detect what are probably very weak features even in  $\text{Mg}_i^+$ , we would require more optimally doped samples to have a chance at seeing the ‘s’-level transitions. A much higher ratio of B:Mg might for instance enable us to see these transitions for  $\text{Mg}_i^+$  specifically, since one would expect most magnesium to be compensated by boron in such a system.

The  $\text{Mg}_i^0$  and  $\text{Mg}_i^+$  regions reveal many excited states in LB samples, with HB counterparts characterized by Stark broadened features and a resulting absence of higher excited states. This is seen in Fig. 4.2 and further detailed in Tab. 4.3 for  $\text{Mg}_i^0$ , which for HB samples have broad features with no peaks beyond  $2p_{\pm}$ . Some fringing effects, particularly visible in the  $^{\text{nat}}\text{Si}$  LB spectrum of Fig. 4.2 are present as a consequence of thin film interference in un-wedged ZnSe dewar windows.

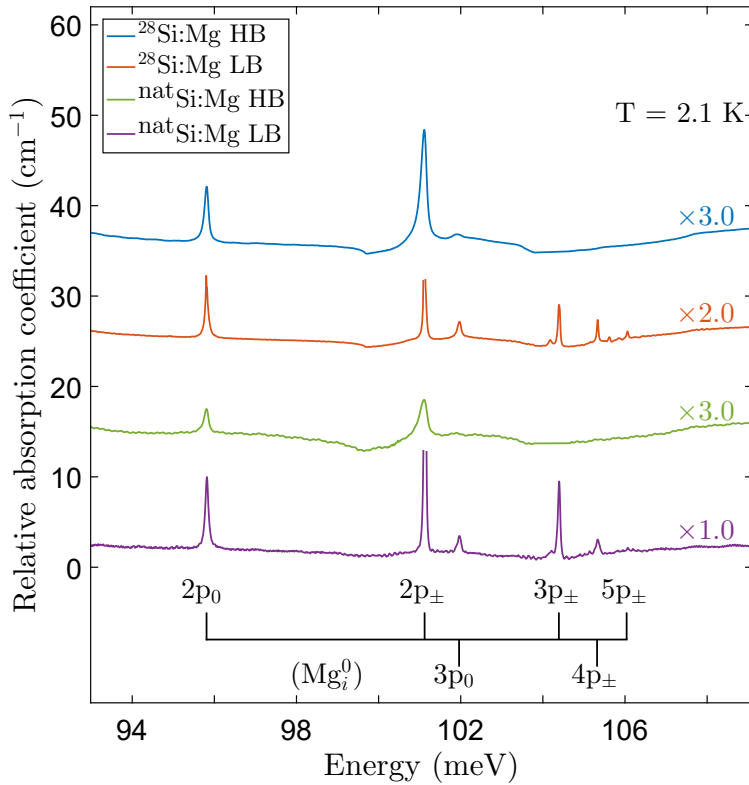


Figure 4.2: Here we examine the  $\text{Mg}_i^0$  region. The  $2p_{\pm}$  transitions have been truncated in LB spectra since for our sample thicknesses, the transmission there was essentially zero. Excited states are visible as high as  $6p_{\pm}$  (See Fig. 4.5 for a more detailed view) in LB samples, but no higher than  $3p_0$  in HB samples due to Stark broadening. Spectra were collected at  $T = 2.1\text{ K}$  with  $0.1\text{ cm}^{-1}$  ( $\sim 0.012\text{ meV}$ ) resolution.

Similarly in the  $\text{Mg}_i^+$  region seen in Fig. 4.3 we note many higher excited states, some newly observed, which are obscured by Stark broadening in more heavily compensated samples. Of particular note in these spectra is splitting of the  $p_{\pm}$  levels visible for  $2p_{\pm}$  in all samples and in higher  $p_{\pm}$  levels in LB samples. Our  $^{28}\text{Si}$ :Mg LB spectra have afforded us an opportunity to study a number of very weak transitions for  $\text{Mg}_i^+$  detailed in Tab. 4.5 that

have not been seen previously. With its lack of isotopic broadening and relatively low boron compensation, this  $^{28}\text{Si}$  sample has also allowed us to observe splitting of the  $p_{\pm}$  levels as high as  $6p_{\pm}$ . By contrast in natural silicon, the presence of  $^{29}\text{Si}$  and  $^{30}\text{Si}$  isotopes leads to a small broadening effect with optical transitions for the heavier isotopes occurring at slightly higher energies. This also obscures fine structure, particularly for high excited states where any splittings are small. As seen in Tab. 4.5 the  $p_{\pm}$  splittings in the LB  $^{28}\text{Si}$  sample are 0.23, 0.10, 0.04, 0.04 and 0.02 meV for  $2p_{\pm}$ ,  $3p_{\pm}$ ,  $4p_{\pm}$ ,  $5p_{\pm}$  and  $6p_{\pm}$  respectively. This is consistent with the splittings observed for  $2p_{\pm}$ , and  $3p_{\pm}$  by Ho [58]. In previous  $\text{Mg}_i$  studies doublets have been proposed to result from wavefunction overlap of the  $p_{\pm}$  excited state wavefunctions with the potential of the donor impurity itself [59, 129]. This is referred to as central cell splitting. Our observations are consistent with decreasing central cell overlap and correspondingly decreased splitting with higher excited state. This matches our expectations for wavefunctions that are increasingly larger in radius with increasing energy (decreasing binding energy). As determined by Kohn and Luttinger [81], in the  $T_d$  symmetry group the  $2p_{\pm}$  level has the reducible representation  $2T_1+2T_2$ . From the  $1s(A)$  spherically symmetric ground state, only transitions to states with  $T_2$  symmetry are allowed. This leaves us with the two degenerate  $T_2$  levels to which transitions can occur. This degeneracy can be lifted by various perturbations, including externally applied magnetic fields/strains often applied to studies of defect symmetry. In this case degeneracy is lifted through some non-zero overlap of the p-states with the central cell potential. This lifting of degeneracy between the two  $T_2$  levels leads to the observed doublet seen in Fig. 4.3 for  $2p_{\pm}$  and to a lesser degree for for higher  $p_{\pm}$  levels.

Splitting of  $p_{\pm}$  levels can be seen in Figs. 4.3, 4.5, and 4.7. The energies for these and all other labelled transitions are included in Tabs. 4.3 and 4.5 for neutral and ionized donors respectively. Transitions in the ionized species are in general less impacted by Stark broadening in HB samples relative to counterparts in the neutral species,  $\text{Mg}_i^0$ , due to lower electric-field sensitivity in the more tightly bound singly-ionized donor excited states. As a consequence, we do not observe splitting of the  $\text{Mg}_i^0$   $p_{\pm}$  states.

We note that all  $p_{\pm}$  doublets show a clear asymmetry in transition strength between components, with the lower energy peak of each doublet always weaker than the higher. This asymmetric character was discussed in detail by Thilderkvist *et al.* [129] based on Zeeman studies of the standard  $\text{Mg}_i$  center. These authors were able to determine expressions for the valley combinations of p-states that make up the two triplet levels. To each of the six equivalent valley minima in the conduction band they attribute two p-states  $p_i^a$  and  $p_j^b$ . From EMT as seen in Eq. 2.11 we have  $p_i^a = P_i(r)u_{k_{\mu}} \exp(ik_{\mu}r)$  for states  $T_1^a$ ,  $T_1^b$ ,  $T_2^a$ , and  $T_2^b$ , i.e. the contributions of  $T_1$  and  $T_2$  to components  $a$  and  $b$  of the doublet. Thilderkvist *et al.* write these as,

$$T_x^a = \frac{1}{2} \left[ (p_x^{(y)} + p_x^{(-y)}) \pm (p_x^{(z)} + p_x^{(-z)}) \right] \quad (4.6)$$

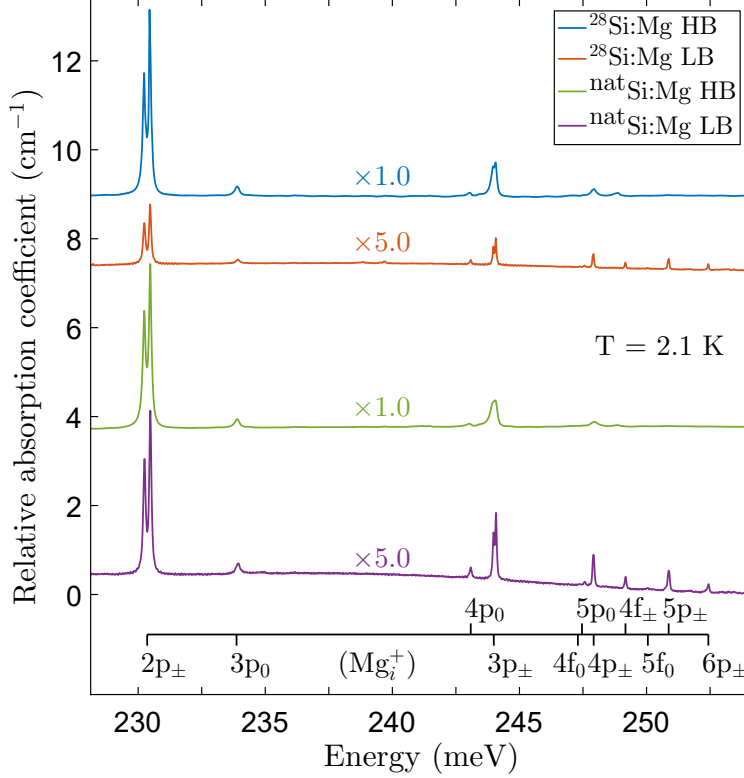


Figure 4.3: A closer look at the transitions of  $\text{Mg}_i^+$  reveals  $np_{\pm}$  doublets (most obviously for  $2p_{\pm}$ ) suggested previously to result from central cell splitting. The splitting decreases with increasing  $n$ , and is less obvious in HB samples due to Stark broadening. Spectra were collected at  $T = 2.1$  K with  $0.1 \text{ cm}^{-1}$  ( $\sim 0.012 \text{ meV}$ ) resolution.

and

$$T_x^b = \frac{1}{2} \left[ (p_z^{(y)} + p_x^{(-y)}) \pm (p_y^{(z)} + p_y^{(-z)}) \right]. \quad (4.7)$$

With the  $\pm$  giving the expressions for the  $T_2$  and  $T_1$  representations respectively, and where  $T_y^{a,b}$  and  $T_z^{a,b}$  equivalents of these states are given by cyclic permutations of the indices. It should be noted that as written here, and shown by Thilderkvist *et al.*, these states  $T_x^a$  and  $T_x^b$  are not orthogonal. This may be indicative of sign/subscript errors in the source material. To make these states orthogonal, one would re-write the term  $(p_z^{(y)} + p_x^{(-y)})$  as  $(p_x^{(y)} - p_x^{(-y)})$ . This does not ultimately influence any conclusions we draw from this analysis.

A symmetry allowed matrix element for the dipole coupled  $T_{2x}^a$  transition from the  $1s(A_1)$  ground state is  $\langle T_{2x}^a | x | 1s(A_1) \rangle$ , which from Eq. 4.6 above is proportional to  $\langle 2p_x | x | 1s \rangle$ . This matrix element is clearly symmetry allowed, involving a transition from the symmetric  $1s(A_1)$  to the odd-parity  $2p_{\pm}$  excited state. It is also EMT allowed since  $2p_x$  is coupled to  $1s(A_1)$  via the  $x$  operator. This means it represents a non-zero integral over the product of  $2p_x$  and  $1s(A_1)$  wavefunctions and the  $x$  operator. We therefore anticipate observing a strong transition. By contrast the equivalent  $T_{2x}^b$ , which has matrix element  $\langle T_{2x}^b | x | 1s(A_1) \rangle$ , involves

$\langle 2p_z|x|1s\rangle$ . This matrix element is again symmetry allowed but here is EMT forbidden, since  $2p_z$  is coupled to  $1s(A_1)$  via the  $x$  operator. In this case, the integral over the product of wavefunctions and operator will give a result of zero. Since, however, any linear combination of the  $T_2^a$  and  $T_2^b$  states that yields a symmetry allowed transition is likewise allowed, Thilderkvist *et al.* define a new set of states for  $T_2$  as,

$$T_{2x}^{(1)} = \cos(\theta)T_{2x}^a + \sin(\theta)T_{2x}^b \quad (4.8)$$

and

$$T_{2x}^{(2)} = -\sin(\theta)T_{2x}^a + \cos(\theta)T_{2x}^b \quad (4.9)$$

and equivalently for the  $T_1$  states. Since the  $T_{2x}^b$  states contribute little, being EMT forbidden [129], Thilderkvist *et al.* were then able to determine a value for the parameter  $\theta$  based on the relative intensities of the components of the  $2p_{\pm}$  doublet. This was calculated as  $\theta \sim \pm 48.5^\circ$  or equivalently  $180^\circ \pm 48.5^\circ$ . We see these doublet splittings as high as  $6p_{\pm}$  in  $Mg_i^+$ . In our case the parameter  $\theta$  describing the relative contributions of  $T_2^a$  and  $T_2^b$  is determined to be  $\theta \sim \pm 51^\circ$  for  $2p_{\pm}$ , in reasonable agreement with the findings of [129]. Higher  $p_{\pm}$  levels display a gradually increasing integrated intensity contribution from the stronger component of the doublet and a correspondingly increasing value of  $\theta$ . This may represent decreased mixing of  $T_{2x}^a$  and  $T_{2x}^b$  at higher energies.

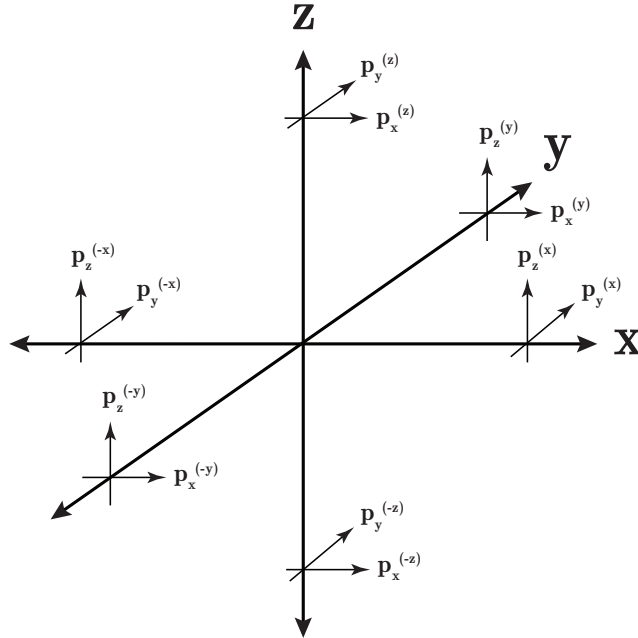


Figure 4.4: Here we show the orientations of  $p_{\pm}$  states associated with each of the six-conduction band minima of Si, as detailed by Thilderkvist *et al.* [129].

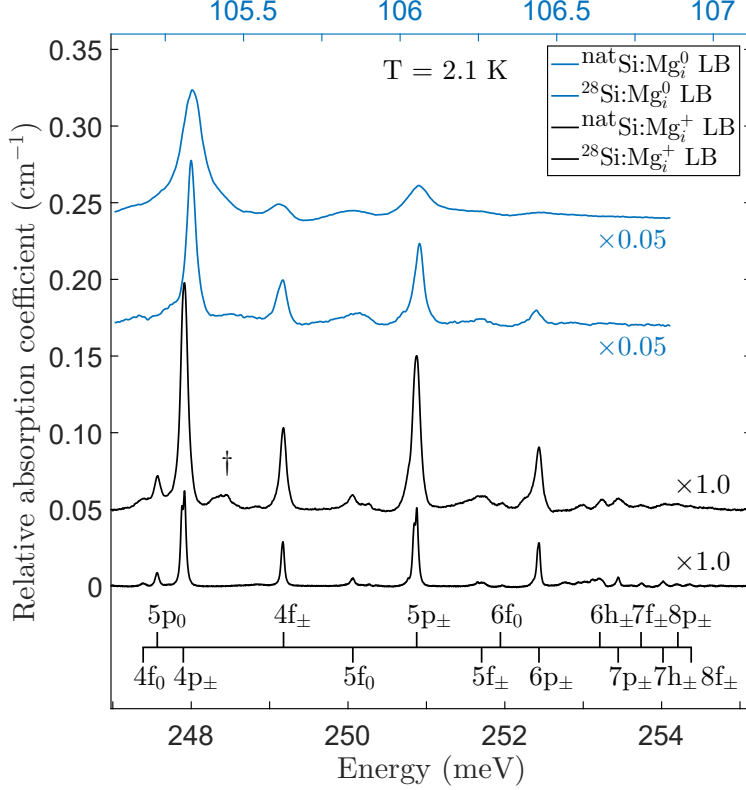


Figure 4.5: Spectra displaying several newly observed excited states of  $\text{Mg}_i^0$  and  $\text{Mg}_i^+$  in LB samples. The bottom axis (black) corresponds to  $\text{Mg}_i^+$  spectra while top (blue) corresponds to  $\text{Mg}_i^0$ . The spectral window for the  $\text{Mg}_i^+$  data displayed has been chosen to be four times larger than that of  $\text{Mg}_i^0$ , giving matched line spacings on the plot between the two for ease of viewing. The † symbol labels a feature of unknown origin seen in the  $^{\text{nat}}\text{Si}$   $\text{Mg}_i^+$  spectrum. Data for these spectra were collected at  $T = 2.1$  K and  $0.05 \text{ cm}^{-1}$  ( $\sim 0.0062 \text{ meV}$ ) resolution.

In Fig. 4.6 we see a broader view of the  $\text{Mg}_i^+$  spectrum, including the  $2p_0$  transition, and also note the presence of another singly ionized double donor labelled  $\text{Mg}_{i^*}^+$ , data for which is covered in the next section. We see a doublet with peaks at  $147.59 \text{ meV}$  and  $147.95 \text{ meV}$ , indicated in Fig. 4.6 with a † in HB samples. This represents the  $2p_{\pm}$  transition of an unknown deep donor, higher excited states of which are too weak to be seen in Fig. 4.6. It is possible this center is also Mg related given its appearance in only the most heavily compensated samples, however it is too weak to characterize here.

In Fig. 4.7 we note the shift between  $^{28}\text{Si}$  and  $^{\text{nat}}\text{Si}$  generated by an  $\sim 0.01 \text{ meV}$  difference in their ground state binding energy. A slight narrowing of the peaks in isotopically enriched silicon is visible relative to its natural silicon counterparts in both  $\text{Mg}_i^0$  and  $\text{Mg}_i^+$ . In the latter we see a partially resolved doublet thought to result from central cell interaction still visible even at this higher excited state ( $4p_{\pm}$ ) in  $^{28}\text{Si}$ . We also note that even in LB samples, neither natural nor enriched silicon samples show particularly narrow transitions

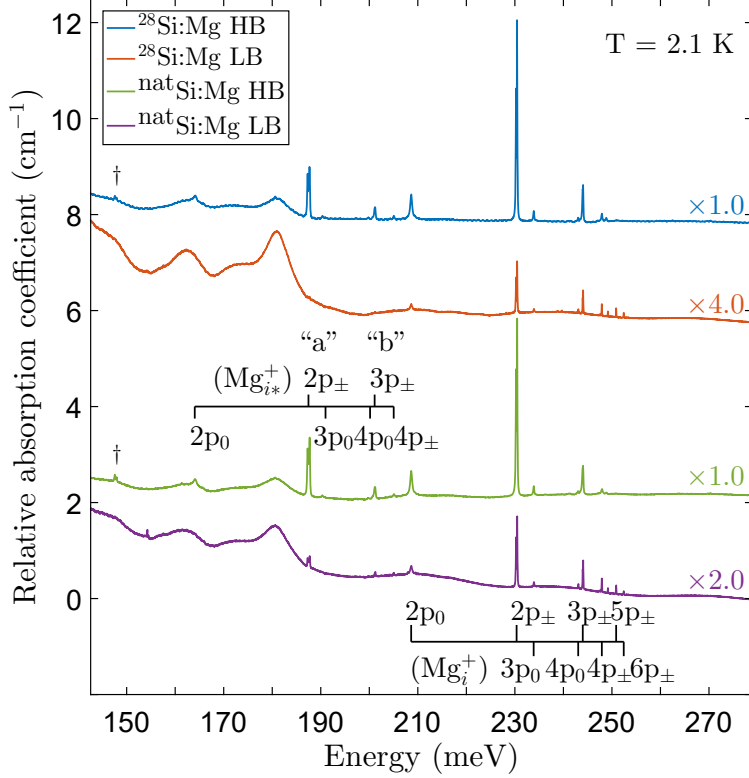


Figure 4.6: In the ionized region we observe known excited states as high as  $6p_{\pm}$  for  $Mg_i^+$  and up to  $4p_{\pm}$  for the alternate magnesium center,  $Mg_{i*}^+$ , which is examined more closely later. Here we also display the  $2p_0$  levels left out of other figures for the sake of viewing higher excited states. The  $2p_{\pm}$  and  $3p_{\pm}$  levels of  $Mg_{i*}^+$  are also labelled by “a” and “b” for consistency with the labelling scheme introduced by Ho [61]. A doublet of unknown origin is visible and indicated by a † in both  $^{nat}\text{Si}$  and  $^{28}\text{Si}$  HB samples. Spectra were collected at  $T = 2.1$  K with  $0.1 \text{ cm}^{-1}$  ( $\sim 0.012 \text{ meV}$ ) resolution.

for the singly-ionized species relative to those of the singly-ionized chalcogen double donors [91]. This may be a consequence of magnesium also incorporating as a substitutional double acceptor [10] as well as an interstitial double donor. Since both donors and acceptors are present, magnesium is capable of acting as its own compensating species, resulting in ionized donors and acceptors throughout the sample. This would give rise to an intrinsic Stark broadening of spectral lines. Strain fields could also cause inhomogeneous broadening, as discussed in the theory section, though this effect is not specific to magnesium’s dual nature as a double donor/acceptor.

Spacings between excited state levels as measured from the lowest visible level,  $2p_0$ , are seen in Tab. 4.1. We note that the ratio of spacings between  $Mg_i^+$  and  $Mg_i^0$  is consistently near the expected factor of 4 that arises from the helium-like electronic level structure of  $Mg_i^+$  vs. the hydrogen-like spectrum of  $Mg_i^0$ . The fact that the ratio is always slightly greater than 4 is a consequence of the measured binding energy of  $2p_0$  for  $Mg^+$  being somewhat lower than the EMT predicted value of  $45.968 \text{ meV}$  [129]. This is likely due to some non-zero

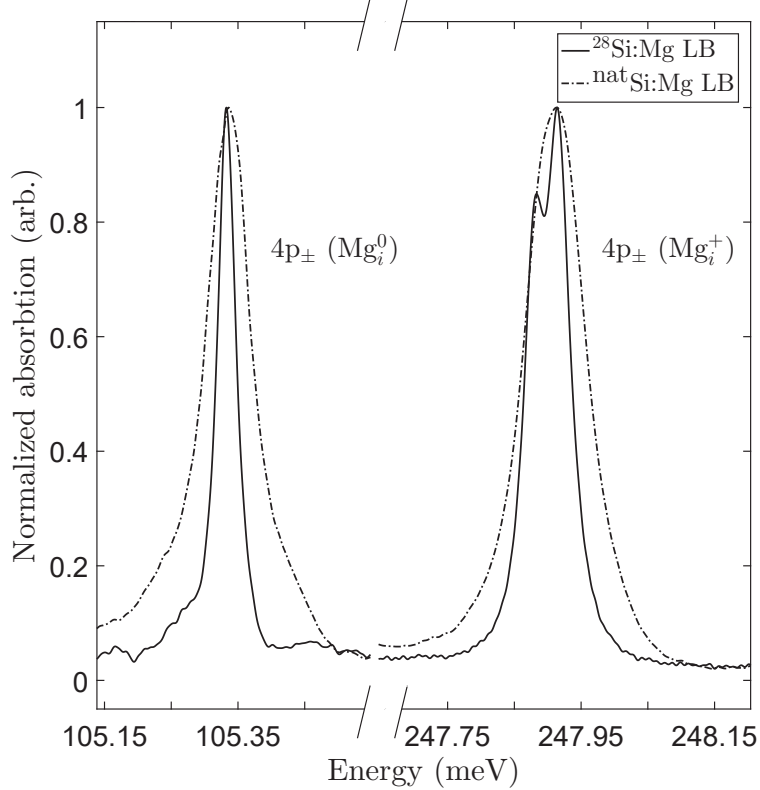


Figure 4.7: Here we illustrate the narrower linewidths observed in  $^{28}\text{Si}$  due to lack of isotopic broadening and a shift in ground state energy of  $\sim 0.01$  meV seen between  $^{28}\text{Si}$  and  $^{\text{nat}}\text{Si}$ . This is shown above for the  $4p_{\pm}$  states of  $\text{Mg}_i^0$  and  $\text{Mg}_i^+$ . The  $\text{Mg}_i^0$  and  $\text{Mg}_i^+$  are presented on a split axis with all lines normalized to the same height for ease of viewing.

overlap of the  $2p_0$  wavefunction with the central cell, as with the  $p_{\pm}$  levels. In Tab. 4.2 we show the the observed binding energies of states in  $\text{Mg}_i^0$  and  $\text{Mg}_i^+$  spectra, contrasted with those predicted by EMT. For the neutral species in particular the agreement is remarkably close. The EMT predicted values for the ionized species are taken to be those of the neutral multiplied by the requisite factor of 4 due to the unscreened nuclear charge seen by the remaining electron. This is the simplest possible assumption and consistently gives a slight overestimate of the binding energy for a majority of higher excited states.

We may also choose to look at spacings relative to higher excited states than  $2p_0$ . Viewed from a sufficiently high excited state, one would expect that the impact of central cell interactions would be much reduced and we would see a spacing ratio much closer to 4. For example if we look at the  $f$  states, the spacing between  $4f_{\pm}$  and  $5f_{\pm}$  in  $^{28}\text{Si}$  is seen to be  $0.63$  meV and  $2.51$  meV in  $\text{Mg}_i^0$  and  $\text{Mg}_i^+$  respectively, the ratio of which is 3.98.

Spacing	Energy (meV)		Ratio
	$\text{Mg}_i^+ (^{28}\text{Si})$	$\text{Mg}_i^0 (^{28}\text{Si})$	
2p <sub>0</sub> -2p <sub>±</sub>	21.72	5.28	4.11
2p <sub>0</sub> -3p <sub>0</sub>	25.28	6.15	4.11
2p <sub>0</sub> -4p <sub>0</sub>	34.44	8.37	4.11
2p <sub>0</sub> -3p <sub>±</sub>	35.38	8.59	4.12
2p <sub>0</sub> -4p <sub>±</sub>	39.26	9.52	4.12
2p <sub>0</sub> -4f <sub>±</sub>	40.53	9.81	4.13
2p <sub>0</sub> -5f <sub>0</sub>	41.42	10.04	4.13
2p <sub>0</sub> -5p <sub>±</sub>	42.22	10.25	4.12
2p <sub>0</sub> -5f <sub>±</sub>	43.04	10.44	4.12
2p <sub>0</sub> -6p <sub>±</sub>	43.78	10.62	4.12

Table 4.1: Peak spacings from 2p<sub>0</sub> to higher states of the standard  $\text{Mg}_i^+$  and  $\text{Mg}_i^0$  species in <sup>28</sup>Si. Ratios of the spacings between the ionized and neutral species are consistently slightly greater than the expected value of 4.

Label	Energy (meV)					
	$\text{Mg}_i^0 (^{28}\text{Si})$	EMT	$\delta$	$\text{Mg}_i^+ (^{28}\text{Si})$	EMT	$\delta$
2p <sub>0</sub>	11.69	11.492	0.20	47.85	45.97	1.88
2p <sub>±</sub>	6.41	6.402	0.01	26.13	25.61	0.52
3p <sub>0</sub>	5.54	5.485	0.06	22.57	21.94	0.63
4p <sub>0</sub>	3.32	3.309	0.01	13.41	13.24	0.17
3p <sub>±</sub>	3.10	3.120	-0.02	12.47	12.48	-0.01
4f <sub>0</sub>	-	2.339	-	9.11	9.36	-0.25
5p <sub>0</sub>	-	2.235	-	8.92	8.94	-0.02
4p <sub>±</sub>	2.17	2.187	-0.02	8.59	8.75	-0.16
4f <sub>±</sub>	1.88	1.894	-0.01	7.32	7.58	-0.26
5f <sub>0</sub>	1.65	1.630	0.02	6.43	6.52	-0.09
5p <sub>±</sub>	1.44	1.449	-0.01	5.63	5.80	-0.17
5f <sub>±</sub>	1.25	1.260	-0.01	4.81	5.04	-0.23
6f <sub>0</sub>	-	1.241	-	4.52	4.96	-0.44
6p <sub>±</sub>	1.07	1.070	0.00	4.07	4.28	-0.21
7f <sub>0</sub>	-	0.980	-	3.47	3.92	-0.45
6h <sub>±</sub>	-	0.886	-	3.28	3.54	-0.26
7p <sub>±</sub>	-	0.822	-	3.05	3.29	-0.24
7f <sub>±</sub>	-	0.750	-	2.75	3.00	-0.25
7h <sub>±</sub>	-	0.676	-	2.47	2.70	-0.23
8p <sub>±</sub>	-	0.636	-	2.29	2.54	-0.25
8f <sub>±</sub>	-	0.596	-	2.14	2.38	-0.24

Table 4.2: Here we show the observed and EMT predicted binding energies as seen in [101] for transitions observed in  $\text{Mg}_i^0$  and  $\text{Mg}_i^+$  spectra in <sup>28</sup>Si. The differences  $\delta$  between observed and EMT predicted values are included where applicable.

## 4.2 $\text{Mg}_{i^*}^0$ and $\text{Mg}_{i^*}^+$ donor spectra

Below the transitions of  $\text{Mg}_i^0$  and  $\text{Mg}_i^+$  seen in the previous section we observe the neutral and singly ionized species of another double donor, which we label  $\text{Mg}_{i^*}^0$  and  $\text{Mg}_{i^*}^+$ . Here we include views of the neutral and singly ionized species of the double donor we attribute either to magnesium inhabiting a symmetry site other than the usual  $T_d$ , or magnesium complexing with other impurities. In either case the resulting reduction in symmetry relative to  $T_d$  may explain the additional fine structure we observe in a number of spectral lines. This section also contains tables of transition energies as seen in natural and isotopically enriched Si samples for all  $\text{Mg}_i^0$  and  $\text{Mg}_{i^*}^0$  lines (Tab. 4.3) as well as  $\text{Mg}_i^+$  and  $\text{Mg}_{i^*}^+$  (Tab. 4.5). Background structure seen in the  $\text{Mg}_i/\text{Mg}_{i^*}$  regions is generated by a broad band of multi-phonon absorption features seen most prominently in Figs. 4.6 and 4.8.

The neutral region is seen in Fig. 4.8 and the ionized in Figs. 4.6 and 4.10. Some of these lines have been observed previously by Ho [60, 61] who labelled features of our  $\text{Mg}_{i^*}^0$  as lines “1”-“6”, and of  $\text{Mg}_{i^*}^+$  as “a” and “b”, however our interpretation of all these lines as arising from the neutral and singly ionized charge states of a single perturbed  $\text{Mg}_i$  species is new. As with  $\text{Mg}_i^0$  and  $\text{Mg}_i^+$  we see no sign of the s-level valley-orbit transitions, whether  $1s(A_1)$  to  $1s(T_2)$  in absorption or  $1s(A_1)$  to  $1s(E)$  in Raman. This is not unexpected given that  $\text{Mg}_{i^*}$  centers are shallower than  $\text{Mg}_i$  for which we also don’t observe such transitions.

As in  $\text{Mg}_i^0$  and  $\text{Mg}_i^+$ , the HB samples show significant Stark broadening that obscures any fine structure, and suppresses higher excited states of the  $\text{Mg}_{i^*}$  species. High excited states are most easily resolved in the LB sample spectra, and in particular in  $^{28}\text{Si}$ , thanks to a lack of isotopic broadening.

We determine the ionization energies of  $\text{Mg}_{i^*}^0$  and  $\text{Mg}_{i^*}^+$  by the binding energies of one of the highest cleanly resolved  $\text{Mg}_{i^*}$  transitions,  $4p_{\pm}$ , added to the corresponding EMT predicted binding energies. For  $4p_{\pm}$  these are 2.187 and 8.75 meV for the neutral and ionized species respectively [101]. From this we estimate that  $\text{Mg}_{i^*}^0$  and  $\text{Mg}_{i^*}^+$  have ionization energies of 94.41 and 213.80 meV respectively, both slightly higher than the estimates given by Ho, which were 94.36 and 213.53 meV [57, 61]. For  $\text{Mg}_{i^*}^+$ , Altarelli’s predicted transition energy of 155 meV for  $1s(A_1)$  to  $1s(T_2)$  [5] then suggests we should see that transition in the shallow donor region, though no sign of it is seen in these samples.

We note unusual fine structure in the  $2p_0$  level of  $\text{Mg}_{i^*}^0$  seen in Fig. 4.8 and through fits to the LB sample transition in Fig. 4.9. Energies of the peaks in this apparent partially resolved quartet are given in Tab. 4.3. In  $T_d$  symmetry, the  $2p_0$  level has the representation  $A_1 + E + T_2$ . Of these however, only transitions to states with  $T_2$  symmetry are dipole allowed in the tetrahedral group. This gives rise to the commonly observed singlet for these states. The fine structure we observe in  $2p_0$  is therefore immediately indicative of a symmetry lower than  $T_d$ .

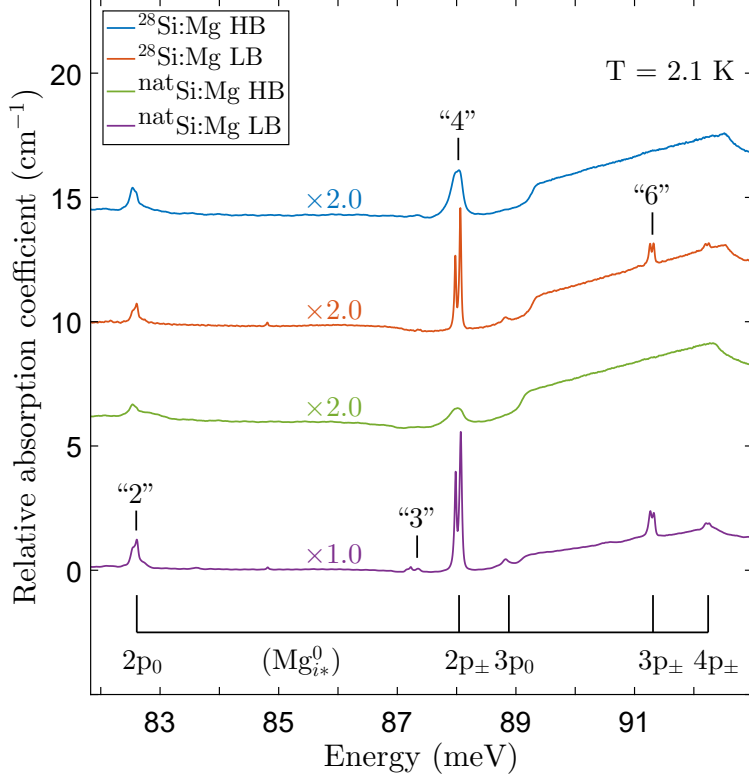


Figure 4.8: The  $\text{Mg}_{i^*}^0$  center (with excited states seen up to  $4p_{\pm}$ ) has been previously observed by Ho [60, 61]. We note that the  $2p_0$  transition has partially resolved fine structure suggesting up to four peaks as detailed in Fig. 4.9. The labels 2, 3, 4 and 6 are those introduced by Ho [60, 61]. Spectra were collected at  $T = 2.1$  K with  $0.1 \text{ cm}^{-1}$  ( $\sim 0.012$  meV) resolution.

As with the standard  $\text{Mg}_i^0/\text{Mg}_i^+$  species,  $\text{Mg}_{i^*}^+$  is significantly less sensitive to Stark broadening than  $\text{Mg}_{i^*}^0$ , revealing complex fine structure of the  $2p_{\pm}$  level in particular. The reduction of this broadening in  $\text{Mg}_{i^*}^+$ , combined with central cell interactions that lift degeneracy between states allowed by the new low symmetry configuration [129], can lead to complex fine structure. The  $2p_{\pm}$  transition of  $\text{Mg}_{i^*}^+$  seen in Fig. 4.10, appears as a partially resolved quartet of states rather than the doublet seen in  $\text{Mg}_i^+$ . A fit to this structure is included in Fig. 4.11. The  $\text{Mg}_{i^*}^+$   $2p_0$  feature was rather weak and broad as seen in Fig. 4.6, and no fine structure could be resolved, through we would anticipate that such structure exists. The relative weakness of this feature is simply a result of there being less of the  $\text{Mg}_{i^*}^+$  species present than  $\text{Mg}_{i^*}^0$ . Parameters for the fits seen in Figs. 4.9 and 4.11 are seen in Tab. 4.4.

We note that the observation of doublets for the  $p_{\pm}$  levels of  $\text{Mg}_{i^*}^0$  is not necessarily inconsistent with the quartet structure of the  $2p_{\pm}$  level of  $\text{Mg}_{i^*}^+$ . Splittings for the neutral species transitions are expected to be less pronounced than those of the ionized. This is due to increased broadening because of their greater electric field sensitivity and smaller

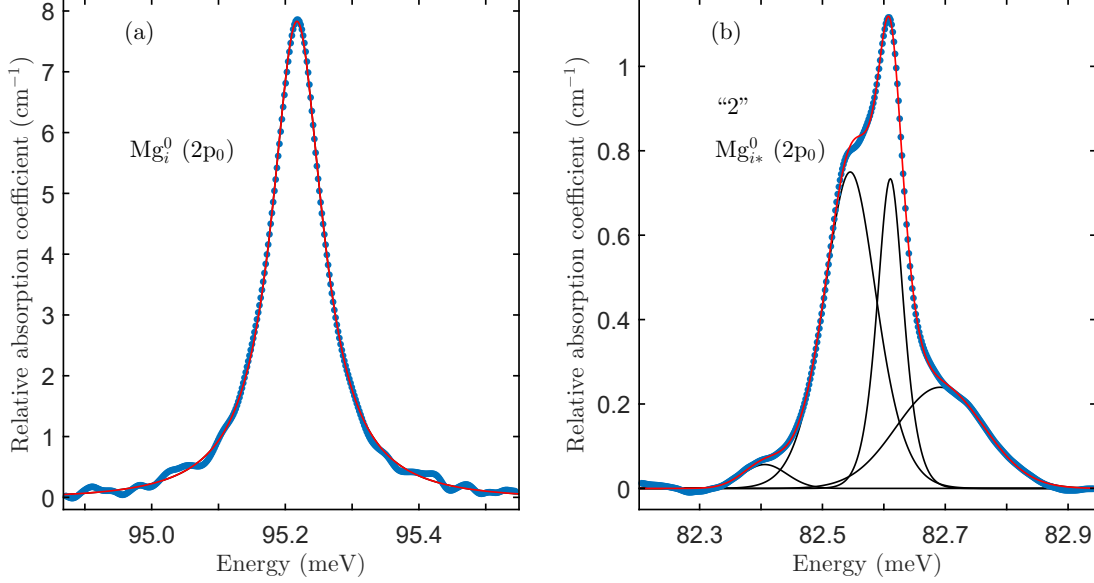


Figure 4.9: **(a)** In the left panel, we see a fit to the  $2p_0$  transition singlet of  $Mg_i^0$ , using one mixed Gaussian-Lorentzian peak. **(b)** On the right we show a fit to the fine structure of the  $2p_0$  feature of  $Mg_{i*}^0$ , referred to by Ho [61] as line “2”, using four mixed Gaussian-Lorentzian peaks. Data shown corresponds to the  $^{nat}Si$  LB sample.

splittings because of a weaker central cell interaction. There may be unresolved extra fine structure in the  $p_{\pm}$  lines of  $Mg_{i*}$  due to the smaller values of these splittings for the neutral center. More generally, the observed splittings for all of these lines can only put a lower bound on the number of non-degenerate components of a given transition. A discussion of point group symmetries included in the appendices demonstrates that the reduced symmetry configuration could belong to the  $C_{3v}$  point group, which is the highest symmetry sub-group of  $T_d$ . As such it is also possible for the configuration to belong to any point group with lower symmetry than  $C_{3v}$ .

Splitting of the  $p_{\pm}$  levels for these spectra is visible only in LB samples, with both  $^{nat}Si/^{28}Si$  spectra revealing doublets through several  $p_{\pm}$  levels. Peak values for visible splittings as high as  $4p_{\pm}$  in  $Mg_{i*}^0$  are detailed in Tab. 4.3, with splittings given by 0.09, 0.06 and 0.06 meV for  $2p_{\pm}$ ,  $3p_{\pm}$  and  $4p_{\pm}$  respectively as seen in Fig. 4.8. In Fig. 4.8, we include Ho’s labels “2”, “4” and “6” [60, 61] corresponding to the  $2p_0$ ,  $2p_{\pm}$  and  $3p_{\pm}$  of  $Mg_{i*}^0$ . We further indicate line “3” also observed by Ho, which will be discussed in the following section.

The complex fine structure of  $Mg_{i*}$  can be understood in the context of a reduced symmetry configuration. We speculate that these alternate centers may result either from  $Mg_i$  that inhabit the hexagonal  $C_{3v}$  site along the  $\langle 111 \rangle$  crystal axis or from  $Mg_i$  forming a complex with another impurity. This new symmetry that is a subgroup of the  $T_d$  symmetry of the standard  $Mg_i$  impurity leads to a lifting of degeneracies [130, 48] of excited states leading to the extra structure observed in these transitions.

Label	Transition energy (meV)			
	$\text{Mg}_i^0$ ( $^{\text{nat}}\text{Si}$ )	$\text{Mg}_{i*}^0$ ( $^{\text{nat}}\text{Si}$ )	$\text{Mg}_i^0$ ( $^{28}\text{Si}$ )	$\text{Mg}_{i*}^0$ ( $^{28}\text{Si}$ )
2p <sub>0</sub>	95.82	82.40	95.81	-
		82.55		82.55
		82.61		82.61
		82.69		82.71†
2p <sub>±</sub>	101.08	87.98	101.09	87.98
		88.07		88.06
3p <sub>0</sub>	101.97	88.82	101.96	88.82
4p <sub>0</sub>	104.24	-	104.18	-
3p <sub>±</sub>	104.39	91.27	104.40	91.26
		91.33		91.32
4f <sub>0</sub>	-	-	-	-
5p <sub>0</sub>	-	-	-	-
4p <sub>±</sub>	105.34	92.20	105.33	92.19
		92.26		92.25
4f <sub>±</sub>	105.61	-	105.62	-
5f <sub>0</sub>	105.84	-	105.85	-
5p <sub>±</sub>	106.06	92.95†	106.06	-
5f <sub>±</sub>	106.22	-	106.25	-
6f <sub>0</sub>	-	-	-	-
6p <sub>±</sub>	106.47†	-	106.43†	-

Table 4.3: Peak positions of observed  $\text{Mg}_i^0/\text{Mg}_{i*}^0$  transitions in  $^{\text{nat}}\text{Si}$  and  $^{28}\text{Si}$  samples. The † symbol labels particularly weak features.

The alternate symmetry site  $\text{C}_{3v}$ , discussed by Ho and Ramdas [59] and Baxter and Ascarelli [15] predicts additional fine structure potentially consistent with what we observe in  $\text{Mg}_{i*}^0$  and  $\text{Mg}_{i*}^+$  spectra. The four visible peaks of  $\text{Mg}_{i*}^+$  for  $2p_{\pm}$  can be understood in group theory terms by considering a symmetry such as  $\text{C}_{3v}$  that is a subgroup of the  $\text{T}_d$  symmetry of the standard  $\text{Mg}_i$  impurity, leading to a lifting of degeneracy [130, 48]. As determined by Kohn and Luttinger [81], in the  $\text{T}_d$  group the  $2p_{\pm}$  level has the reducible representation  $2\text{T}_1+2\text{T}_2$ . From the  $1s(\text{A}_1)$  ground state, only transitions to states with  $\text{T}_2$  symmetry are dipole allowed. Lifting of degeneracy between the two  $\text{T}_2$  levels through central cell interaction leads to the commonly observed doublet seen in Fig. 4.3 for  $2p_{\pm}$  and to a lesser degree for higher  $p_{\pm}$  levels.

As an example we now discuss the additional fine structure one would expect from the  $\text{C}_{3v}$  site relative to the usual  $\text{T}_d$ . Character tables depicting the allowed symmetry operations of these groups are included in the appendices. Representations of a group that are ‘irreducible’ in one point group, are not necessarily so in another. On moving from  $\text{T}_d$  to  $\text{C}_{3v}$  we find that  $\text{T}_1$  and  $\text{T}_2$  decompose as  $\text{E}+\text{A}_2$  and  $\text{E}+\text{A}_1$  respectively. The matrix elements  $\int \Psi_i \hat{\text{O}} \Psi_f$ , then imply that transitions to  $\text{A}_1$  and  $\text{E}$  will be dipole allowed from an  $\text{A}_1$  ground state. This is based on the result of the triple product of symmetry representations for each

Parameter	Defect/transition label			
	$\text{Mg}_i^0$ ( $2p_0$ )	$\text{Mg}_{i*}^0$ ( $2p_0$ )	$\text{Mg}_i^+$ ( $2p_{\pm}$ )	$\text{Mg}_{i*}^+$ ( $2p_{\pm}$ )
$A$	7.83	0.060	0.40	0.90
		0.75	0.57	0.28
		0.73		0.72
		0.24		0.67
$\nu_0$ (meV)	95.82	82.40	230.24	187.28
		82.55	230.47	187.46
		82.61		187.64
		82.69		187.73
$\gamma$ (meV)	0.09	0.08	0.11	0.20
		0.11	0.10	0.15
		0.05		0.26
		0.17		0.13
$f$	0.97	0.00	0.98	0.95
		0.49	0.97	0.88
		0.64		0.90
		0.00		0.56

Table 4.4: Fit parameters as seen in Eqs. 4.2, 4.3, and 4.4 for fits to  $\text{Mg}_i$  and  $\text{Mg}_{i*}$  transitions seen in Figs. 4.9 and 4.11. These include fits to  $2p_0$  ( $\text{Mg}_i^0/\text{Mg}_{i*}^0$ ) and  $2p_{\pm}$  features ( $\text{Mg}_i^+/\text{Mg}_{i*}^+$ ).

term in the integrand containing some contribution from the fully symmetric representation  $A_1$ . The dipole operator  $\hat{O}$  is taken here to belong to representations that transform as translations (x,y,z), i.e.  $A_1+E$  for  $C_{3v}$ . Transitions from  $A_1$  to  $A_2$  are forbidden since the triple product contains no contribution from  $A_1$  and therefore implies an odd function that integrates to zero over all space. This leaves three allowed transitions, two doubly degenerate doublets  $E$  and doubly degenerate singlets  $A_1$ . Degeneracy between those levels could be lifted through central cell interaction [129] leading to a total of six possible lines, of which we observe as many as four, demonstrating the plausibility of a  $C_{3v}$  assignment. The fine structure in the  $2p_0$  of  $\text{Mg}_{i*}^0$  is likewise potentially consistent with this assignment. In  $T_d$ ,  $2p_0$  has the irreducible representation  $A_1+E+T_2$ . Since as discussed in  $C_{3v}$ ,  $T_2$  decomposes as  $E+A_1$ , we are left with a possible total of four lines, all of which we see.

As discussed in the next section evidence provided by an anneal/quench procedure suggests that the reduced symmetry of this center is actually more likely derived from it being part of a complex rather than inhabiting the  $C_{3v}$  interstitial site. This means that the symmetry of  $\text{Mg}_i^*$  will be some sub-group of  $T_d$ , whether  $C_{3v}$  or lower.

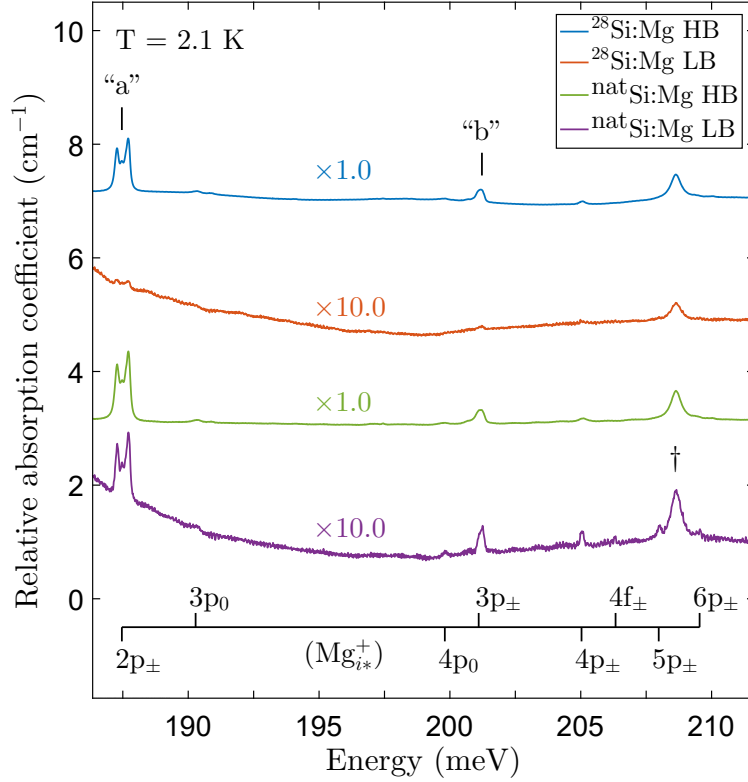


Figure 4.10: Here we see the donor spectrum of  $\text{Mg}_{i^*}^+$ . In the fine structure of  $2p_{\pm}$  in  $\text{Mg}_{i^*}^+$  we note that there is more than a simple doublet visible. Closer inspection reveals at least four peaks, a fit to which is seen in Fig. 4.11. The  $\dagger$  symbol denotes the  $2p_0$  line of  $\text{Mg}_{i^*}^+$ . Labels “a” and “b” correspond to Ho’s notation [61] for lines we identify as the  $2p_{\pm}$  and  $3p_{\pm}$  of  $\text{Mg}_{i^*}^+$ . Spectra were collected at  $T = 2.1$  K with  $0.1 \text{ cm}^{-1}$  ( $\sim 0.012 \text{ meV}$ ) resolution.

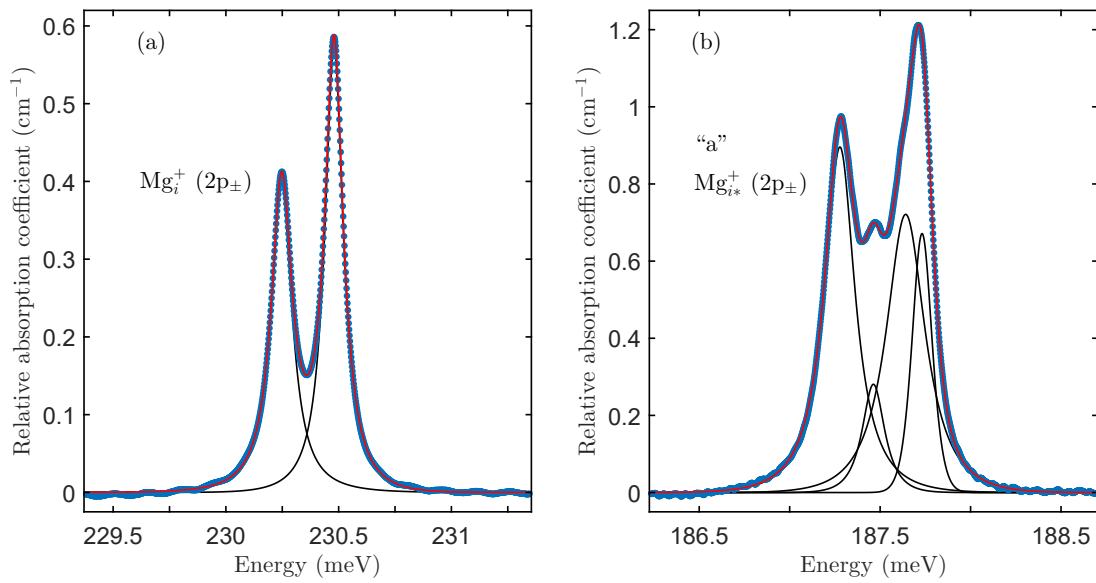


Figure 4.11: **(a)** In the left panel we include a fit to the  $2p_{\pm}$  transition doublet of  $\text{Mg}_i^+$ , using two mixed Gaussian-Lorentzian peaks. **(b)** On the right we display a fit to the fine structure of the  $2p_{\pm}$  feature of  $\text{Mg}_{i*}^+$ , referred to by Ho [61] as line “a”, using four mixed Gaussian-Lorentzian peaks. Data shown for  $\text{Mg}_i^+$  and  $\text{Mg}_{i*}^+$  correspond to the  $^{\text{nat}}\text{Si}$  LB and  $^{\text{nat}}\text{Si}$  HB samples respectively.

Label	Transition energy (meV)			
	$\text{Mg}_i^+$ ( $^{\text{nat}}\text{Si}$ )	$\text{Mg}_{i*}^+$ ( $^{\text{nat}}\text{Si}$ )	$\text{Mg}_i^+$ ( $^{28}\text{Si}$ )	$\text{Mg}_{i*}^+$ ( $^{28}\text{Si}$ )
2p <sub>0</sub>	208.65	164.09	208.64	164.09
2p <sub>±</sub>	230.25	187.28	230.24	187.27
	230.48	187.46	230.47	187.46
		187.64		187.63
		187.73		187.73
3p <sub>0</sub>	233.94	190.33	233.92	190.32
4p <sub>0</sub>	243.08	199.76	243.08	199.77
3p <sub>±</sub>	243.98	201.20	243.97	201.15
	244.08		244.07	
4f <sub>0</sub>	247.37	-	247.38	-
5p <sub>0</sub>	247.57	-	247.57	-
4p <sub>±</sub>	247.91	205.05	247.88	205.05
			247.92	
4f <sub>±</sub>	249.17	206.30†	249.17	-
5f <sub>0</sub>	250.05	-	250.06	-
5p <sub>±</sub>	250.87	208.00†	250.84	-
			250.88	
5f <sub>±</sub>	251.69	-	251.68	-
6f <sub>0</sub>	251.98	-	251.97	-
6p <sub>±</sub>	252.44	209.54†	252.41	-
			252.43	
7f <sub>0</sub>	252.98	-	253.02	-
6h <sub>±</sub>	253.23	-	253.21	-
7p <sub>±</sub>	253.45	-	253.44	-
7f <sub>±</sub>	253.73	-	253.74	-
7h <sub>±</sub>	254.04	-	254.02	-
8p <sub>±</sub>	254.19	-	254.20	-
8f <sub>±</sub>	254.37	-	254.35	-

Table 4.5: Peak positions of observed  $\text{Mg}_i^+/\text{Mg}_{i*}^+$  transitions in  $^{\text{nat}}\text{Si}$  and  $^{28}\text{Si}$  samples. The † symbol labels particularly weak features.

### 4.3 Thermal effects

Here we discuss the impact on  $\text{Mg}_{i^*}$  spectra of temperature dependence studies which reveal interesting new behaviours. With increasing temperature we note that the  $2p_0$ ,  $2p_{\pm}$ , and  $3p_{\pm}$  lines of  $\text{Mg}_{i^*}^0$ , previously referred to by Ho as lines “2”, “4” and “6” thermalize to a second set of levels previously referred as lines “1”, “3” and “5” [57, 61].

Annealing the sample at  $1200^\circ\text{C}$  followed by a quench into alcohol causes dramatic reduction in intensity of all  $\text{Mg}_{i^*}$  features. This suggests that  $\text{Mg}_{i^*}$  may be a complex rather than  $\text{Mg}_i$  inhabiting an alternate interstitial site.

#### 4.3.1 Anneal and Quench

The alternate symmetry site  $C_{3v}$ , discussed by Ho and Ramdas and [59] and Baxter and Ascarelli [15] predicts additional fine structure potentially consistent with what we observe in  $\text{Mg}_{i^*}^0$  and  $\text{Mg}_{i^*}^+$  spectra. However, as we note in Fig. 4.12, a five minute anneal at  $1200^\circ\text{C}$  and subsequent quench into alcohol results in the reduction or elimination of all  $\text{Mg}_{i^*}$  lines. This points to the most likely scenario being that  $\text{Mg}_{i^*}$  is a complex that Mg forms with some other species. Such a center would dissociate at  $1200^\circ\text{C}$  and be prevented from reforming during the rapid cooldown of the quench. This behaviour would not be expected if  $\text{Mg}_{i^*}$  was due to an alternate interstitial site since if anything, one would expect a more equal population of nearly degenerate interstitial sites at elevated temperature. In other words we would have anticipated a strengthening of the  $\text{Mg}_{i^*}$  features post anneal/quench if it did represent an alternate interstitial site. We cannot make any definitive statements about the lifting of degeneracy we expect without knowing the precise nature of the potential  $\text{Mg}_{i^*}$  complex.

If the  $\text{Mg}_{i^*}$  center is a complex it seems likely that the second component is both ubiquitous and electronically neutral in silicon, since transitions of  $\text{Mg}_{i^*}$  have been seen in many samples [60, 61] and  $\text{Mg}_{i^*}$  still acts as a deep double donor, just as it does when complexed with oxygen [57]. With this in mind, carbon, which lies in the same periodic group as silicon, is a possible candidate. As noted by Jones *et al.* [70], substitutional acceptor complexes involving carbon referred to as X-centers are known to form among the Group IIIA elements. Other possibilities that could give rise to an Mg-related double donor could include an  $\text{Mg}_i\text{-Mg}_s\text{-Mg}_i$  complex, or  $\text{Mg}_i$  associated with a neutral damage center such as a vacancy.

#### 4.3.2 Thermalization of $\text{Mg}_{i^*}^0$ levels

We now discuss lines “1”, “3”, and “5” previously observed by Ho and interpreted to be ground state to  $2p_0$ ,  $2p_{\pm}$  and  $3p_{\pm}$  transitions of a donor with an ionization energy  $0.79\text{ meV}$  less than that of the donor responsible for lines “2”, “4”, and “6” [57, 61]. We instead find that lines “1” through “6” all arise from the same perturbed  $\text{Mg}_{i^*}^0$  donor, with lines “2”, “4”,

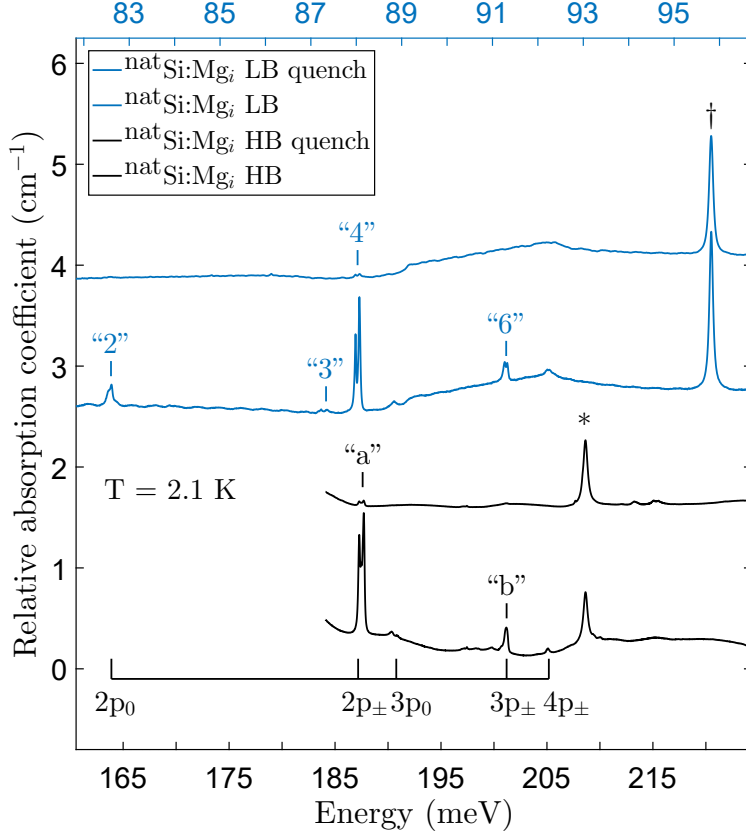


Figure 4.12: Here we show the same samples viewed in absorption before and after a five minute anneal at 1200 °C and quench into alcohol reveal dramatic changes in the  $Mg_{i*}$  region. The top two spectra depict the neutral species and are plotted against the top axis. The bottom two spectra show the ionized species and correspond to the bottom axis. After the anneal/quench we see that  $Mg_{i*}^0$  and  $Mg_{i*}^+$  lines are heavily reduced if not eliminated altogether. In the  $Mg_{i*}^+$  spectra we cut off the view past the  $2p_{\pm}$  feature since those regions contain large absorption features from the dewar windows. The † and \* label the positions of the  $2p_0$  transitions of  $Mg_i^0$  and  $Mg_i^+$ , respectively. Axes are scaled by a factor of  $\sim 4$  between the neutral and ionized species such that the transitions of the two charge states are aligned.

and “6” originating from the ground state and lines “1”, “3”, and “5” originating from very low-lying excited states which can be thermally populated even at liquid He temperatures.

At pumped He temperatures the line “1”, “3”, and “5” intensities are very low, as seen in Fig.4.8 where line “3” can barely be observed at 2.1 K, and lines “1” and “5” are unobservable. At 4.2 K the intensities of lines “1”, “3”, and “5” are comparable to those of “2”, “4” and “6”, and at 10 K the “1”, “3”, and “5” lines are stronger than the “2”, “4”, and “6” lines as seen in Fig. 4.13. Focussing on the dominant  $2p_{\pm}$  transitions, we see that line “3” has three components which we labelled 3a, 3b and 3c. As already described, line “4” is a doublet with components labelled 4a and 4b. As can be seen in Fig. 4.13, lines 3a and 3b have very similar temperature dependence, while line 3c increases somewhat less with

increasing temperature than do lines 3a and 3b. This is consistent with the higher energy level, i.e. the lower energy transition, of the pair being populated more quickly at elevated temperatures. Peak positions of these features are listed in Tab. 4.6.

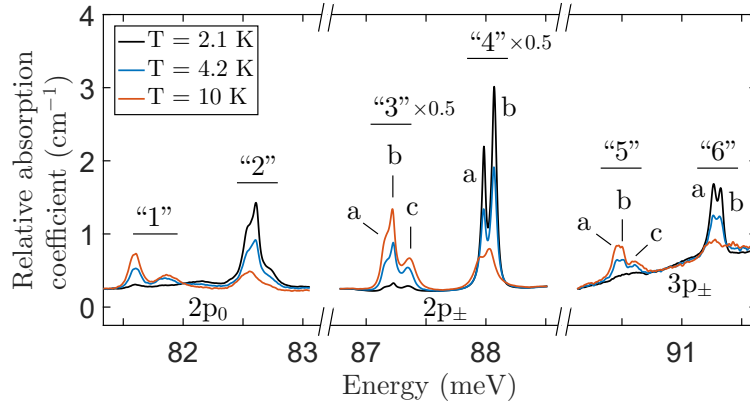


Figure 4.13: Example spectra for three selected temperatures (2.1, 4.2, and 10 K) showing thermal activation between  $\text{Mg}_{i*}^0$  transitions referred to by Ho as lines 2, 4 and 6 and the  $2p_0$ ,  $2p_{\pm}$  and  $3p_{\pm}$  of the thermally activated levels also noted by Ho as 1, 3, and 5 [57, 61]. The  $p_{\pm}$  levels of these are also labelled by visible components “a”-“c”, possibly indicative of two partially resolved doublets. The  $2p_{\pm}$  region showing lines 3 and 4 has been scaled down by a factor of 0.5 for ease of viewing. Data shown corresponds to the  $^{\text{nat}}\text{Si}$  LB sample.

This is shown in more detail in Fig. 4.14, an Arrhenius plot of the line  $3a + 3b$ , and line  $3c$  integrated intensity, vs. the line  $4a + 4b$  integrated intensity as a function of inverse temperature. Activation energies,  $\delta E$ , are extracted from the slopes,  $m$ , of the linear fits as  $\delta E = -mk_B$  with  $k_B$  the Boltzmann constant. The thermal activation energy of  $0.80(2)$  meV for lines  $3a + 3b$ , is in good agreement with the energy shifts between lines  $3a$  ( $3b$ ) and line  $4a$  ( $4b$ ), namely  $0.82(2)$  meV ( $0.84(2)$  meV). The thermal activation energy of  $0.69(3)$  meV for line  $3c$  is similarly in good agreement with the energy difference of  $0.72(2)$  meV between line  $3c$  and line  $4b$ . The origin of the line “3” and line “4” components is summarized in the inset to Fig. 4.14. Very similar behaviour is observed for lines  $5a$ ,  $5b$ ,  $5c$ ,  $6a$ , and  $6b$  terminating in the  $3p_{\pm}$  levels. The behaviour of the line “1” components vs. the “2” components is also consistent with the low lying excited states shown in the inset of Fig. 4.14. The greater splittings of the  $2p_0$  state, as already shown in Fig. 4.9 for line “2”, result in an overlap of transitions from from the two low-lying excited states which cannot be resolved in line “1”.

The ground state structure of  $\text{Mg}_{i*}^0$  is unusual, in that while the ground state is quite deep compared to the group V shallow donors, there are very low-lying excited states. For the group V donors the valley orbit excited states are more than 10 meV above the ground state. For the group-VI chalcogens like selenium, separation of the valley-orbit excited states from the ground state can be hundreds of meV [91, 128]. The precise identity of these low lying states remains a topic for future investigations. To our knowledge, this behaviour is not observed for any other donor in silicon. These levels may represent something not fully

understood about valley orbit splitting for interstitial donors. We note, as seen in the level structure shown in Fig. 4.14, that the second component of the supposed doublet labelled 3c is not visible. It may be that this transition is hidden beneath other features, or is for some reason forbidden. Attempts to observe similar low-lying excited states above the ground state of  $\text{Mg}_{i^*}^+$  center were unsuccessful. Equivalent states in  $\text{Mg}_{i^*}^+$  may simply lie too far above the ground state for thermally activated transitions to be visible before its features are too thermally broadened to be observed.

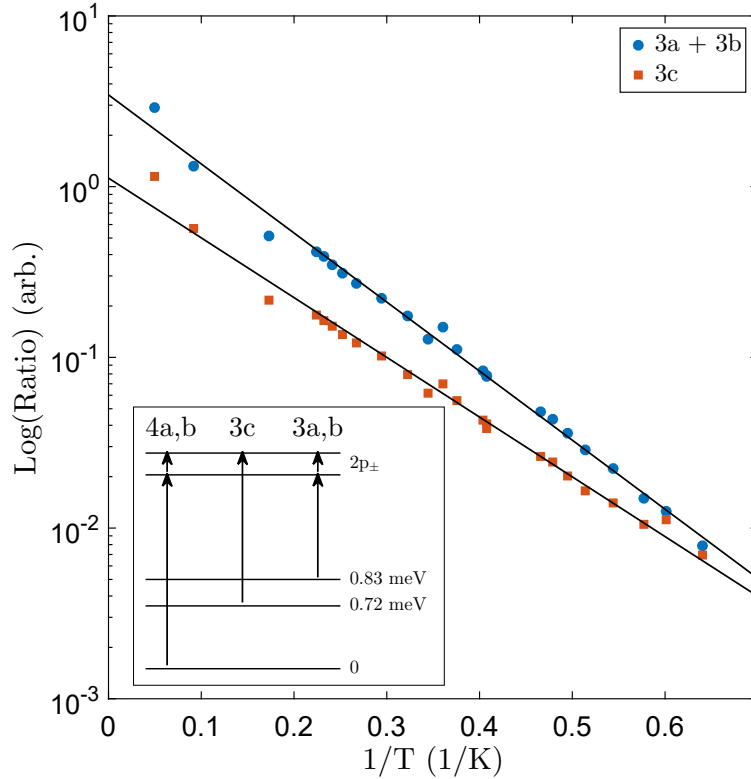


Figure 4.14: Here we see an Arrhenius plot showing integrated intensities of Ho’s line “3” as a function of  $1/T$  for components 3a + 3b together and line 3c. These are expressed as fractions of the integrated intensity of line “4”. In the inset we include a level diagram showing the main  $\text{Mg}_{i^*}^0$   $2p_{\pm}$  transition along with transitions from two low lying levels 0.72(2) meV and 0.83(2) meV above the actual ground state. Here we consider the the positions of these levels to be the average of the optical spacings between components of of lines “3” and “4”. These spacings match well to the thermal activation energies extracted from the slopes of these lines which are 0.80(2) meV and 0.69(3) meV for 3a + 3b and 3c respectively. Data shown corresponds to the  $^{\text{nat}}\text{Si}$  LB sample.

Label	Transition energy (meV)
“1” ( $2p_0$ )	81.56
	81.60
	81.87
“3” ( $2p_{\pm}$ ) (a,b,c)	87.16
	87.23
	87.35
“5” ( $3p_{\pm}$ ) (a,b,c)	90.46
	90.51
	90.61

Table 4.6: Peak positions detailing fine structure of the thermally activated transitions labelled “1”, “3” and “5” in Fig. 4.13. The values for “3” are given for spectra taken at  $T = 2.1$  K as with most other data presented in this work. For “1” and “5” the values correspond to data collected at  $T = 10$  K where the transitions were strong enough to observe and fit reliably.

#### 4.4 Mg-B shallow donor complex

The presence of a new shallow donor we identify as a Mg-B pair is observed in the absorption spectra shown in Fig. 4.15. The presence of another shallow donor that may be Mg related, labelled Mg-?, is also noted. Our identification of these centers as Mg-related single donor complexes follows first from the fact that we work with very high purity silicon, which is known to contain primarily boron and magnesium impurities. The possibility of Mg forming shallow donor complexes with a range of other defects has been discussed by Lin [86]. Further, the possibility of this specific center representing Mg-B or Mg-O, was also speculated on by Pajot [100]. Mg-O has since been identified as a deep double donor by Ho [56, 57], making Mg-B a logical, if not conclusive assignment for a strong, and otherwise new shallow donor. The suggestion that Mg-? represents another Mg-related complex is more tentative, as it is only visible in one sample. The HB samples reveal the Mg-B lines along with strong boron acceptor features. LB samples reveal higher excited states otherwise obscured by Stark broadening along with a number of other shallow donors. Fine structure in the  $2p_0$  line of the Mg-B complex which is revealed to be a doublet is visible in Fig. 4.16. Tab. 4.7 includes the peak positions of the excited states observed for Mg-B and Mg-? as seen in  $^{nat}\text{Si}$ . Some extra fine structure is not unexpected since, as a complex, Mg-B must by definition have reduced symmetry relative to the  $T_d$  symmetry of the Si lattice. The Be isoelectronic pair complex for example was determined by Henry *et al.* [52, 29] to be  $\langle 111 \rangle$  axially symmetric, and based on the results of Zeeman experiments by Henry *et al.* belongs to the  $D_{2d}$  symmetry group. We note that the  $p_{\pm}$  transitions of Mg-B do not appear as more than singlets. This could be because, as shallower levels than  $2p_0$ ,  $2p_{\pm}$  and higher  $p_{\pm}$  states may have splittings that are not as easily resolved.

The signature of Mg-B in Fig. 4.15 is visible alongside those of a number of donor species, including Li and Li-O and a weakly visible Mg-? center. This last donor may represent magnesium associated with some other acceptor such as aluminium [86]. We estimate an ionization energy of 47.50 meV (43.85 meV) for Mg-B (Mg-?) via the energy of the highest visible transitions, namely  $4p_{\pm}$  ( $3p_{\pm}$ ) for Mg-B (Mg-?), and the corresponding theoretical binding energy for that state as detailed by Pajot [101] and included in Tab. 4.2.

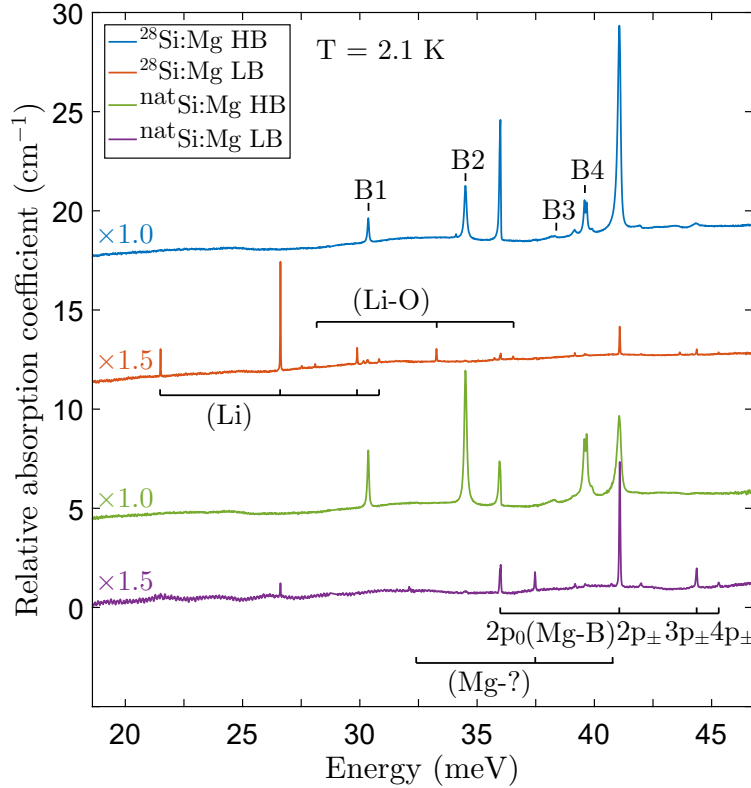


Figure 4.15: Observation of the shallow donor region reveals a center we identify as an Mg-B complex. In HB samples we observe strong boron acceptor features (B1 through B4 [101]) alongside the  $2p_0$ ,  $2p_{\pm}$  and (weakly)  $3p_{\pm}$  peaks of our Mg-B center. Low boron content (LB) samples reveal less Stark broadened versions of these same lines up to  $4p_{\pm}$  along with other shallow donors including Li and Li-O and an unidentified Mg-? donor center. Spectra were collected at  $T = 2.1$  K with  $0.1 \text{ cm}^{-1}$  ( $\sim 0.012 \text{ meV}$ ) resolution.

The Mg-B shallow donor is also observed in photoluminescence through the presence of a new donor bound exciton no-phonon (NP) line and associated TA and TO phonon replicas visible together with bands of boron single and multi-exciton complexes seen in Fig. 4.17. The splittings between the NP line and the TA and TO replicas of the Mg-B center are 18.7(1) meV and 58.2(1) meV respectively, in good agreement with determinations of these energies by Shaklee *et al.* and Vouk *et al.* [111, 132]. Absorption and emission measurements by these authors have led to accepted values of 18.4(2) meV and 58(1) meV for the TA and TO mode respectively [30]. Multi-exciton complexes, studied in detail in

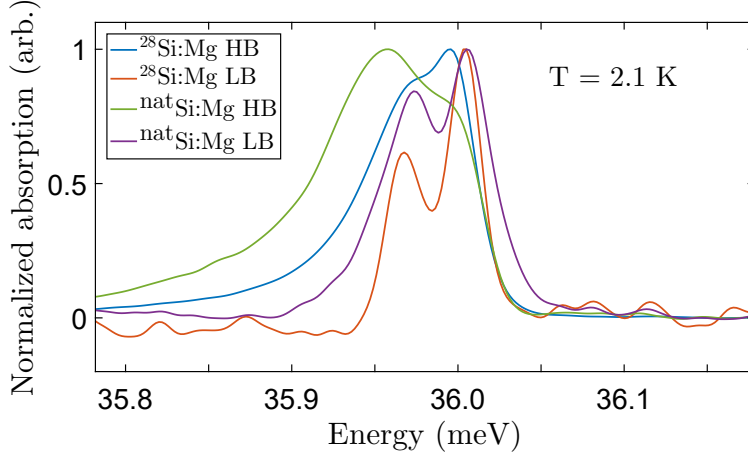


Figure 4.16: Here we note in an expanded view of Fig. 4.15, that the  $2p_0$  transition of Mg-B displays has some fine structure, appearing as a doublet. The  $2p_{\pm}$  transition and higher  $p_{\pm}$  transitions are singlets.

Label	Transition energy (meV)	
	Mg-B	Mg-?
$2p_0$	35.97	32.10
	36.01	
$2p_{\pm}$	41.08	37.47
$3p_0$	42.00	-
$3p_{\pm}$	44.36	40.73
$4p_{\pm}$	45.30	-

Table 4.7: Energies of donor transitions observed in the shallow donor region seen in Fig. 4.15. Values listed for Mg-B and Mg-? are as seen in  $^{nat}\text{Si}$ .

past investigations [78], are seen here only for boron since it is present in the highest concentration. As this is the case, it dominates the TA/TO phonon replica regions, though its NP transition is quite weak. The strength of NP transitions is determined not only by the concentration of an impurity but by the strength of its central cell potential, with stronger potentials corresponding to a higher probability of scattering the electron to the center of the Brillouin zone and overcoming the indirect Si bandgap. Boron has a particularly weak central cell effect as a shallow acceptor, while magnesium, a deep donor of group-II has a relatively strong one. Thus, despite the presumably much lower concentration of Mg-B than B in the sample, the NP transition of Mg-B is much stronger. The NP transition of phosphorus is also visible, though its phonon replicas are hidden beneath those of boron. The boron NP line shows clear evidence of fine structure, which has been examined in detail in past investigations. Yang *et al.* [139] uncovered many spectral components arising as a consequence of valley orbit splitting of the electron energy levels, splitting of hole levels due to hole-hole coupling and isotope splitting.

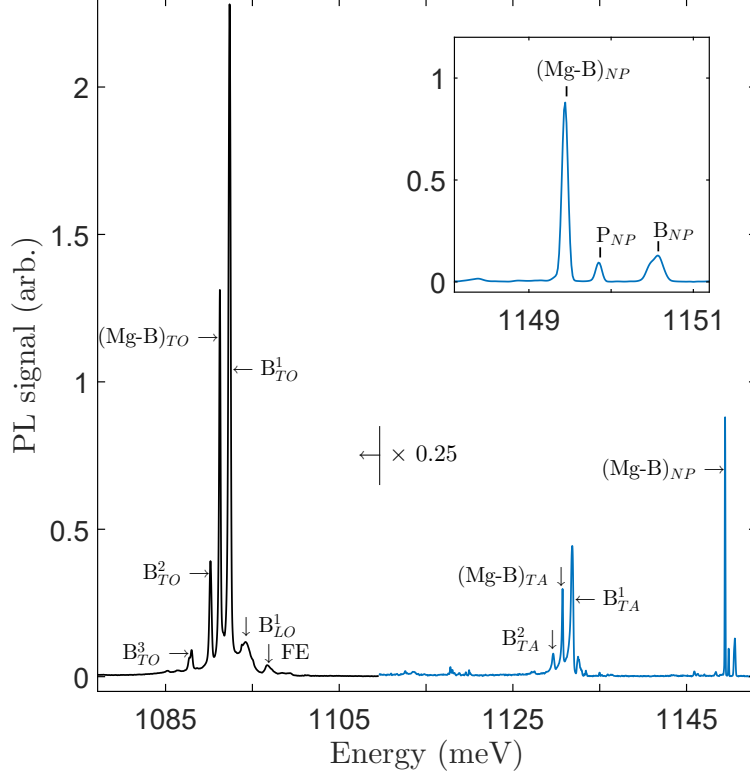


Figure 4.17: Photoluminescence spectrum of the  $^{28}\text{Si}$  HB Mg-diffused sample under 200 mW of 532 nm illumination. The no-phonon (NP) peaks of phosphorus and boron are clearly visible above a new peak we believe corresponds to the Mg-B donor bound-exciton. The TA and TO phonon replicas of the new bound-exciton peak are easily visible together with those of boron single (i.e.  $B_{TO}^1$ ) and multi-exciton (i.e.  $B_{TO}^2$  and  $B_{TO}^3$ ) complexes. A free exciton feature (FE) is also visible. The TO region has been multiplied by a factor of 0.25 in order to appear on the same scale as the TA and NP region. The inset offers an expanded view of the NP region. Spectra were collected at  $T = 4.2$  K with a resolution of  $0.5 \text{ cm}^{-1}$  ( $\sim 0.062 \text{ meV}$ ).

Haynes' rule [49] states that there exists a simple linear relation between the ionization energy of a donor/acceptor and the corresponding localization energy of the donor/acceptor bound exciton for that impurity. From the no-phonon region of our photoluminescence spectrum in Fig. 4.17 we are able to determine an estimated bound-exciton (BE) localization energy of 4.73 meV for Mg-B. With this and a number of other shallow donors studied we constructed the plot seen in Fig. 4.18, where we note that Mg-B follows the same trend, obeying a general form of Hayne's rule  $E_{ex} = A + BE_I$ , with  $A$  and  $B$  as defined in the theory section on the topic. As seen in Fig. 4.18, we find  $B = 0.11$ , and  $A = -0.71 \text{ meV}$ . All our BE localization energies are determined relative to the phosphorus no-phonon BE feature visible in all samples. The phosphorus BE localization energy is calculated as the spacing between the phosphorus TA phonon replica and the low energy edge of the free-exciton TA yielding an estimate of 4.32 meV. This and other BE localization energies seen

in Fig. 4.18 are listed in Tab. 4.8. Energies of the Li and Li-O transitions visible primarily in the  $^{nat}\text{Si}$  spectrum of Fig. 4.15 are tabulated in [101].

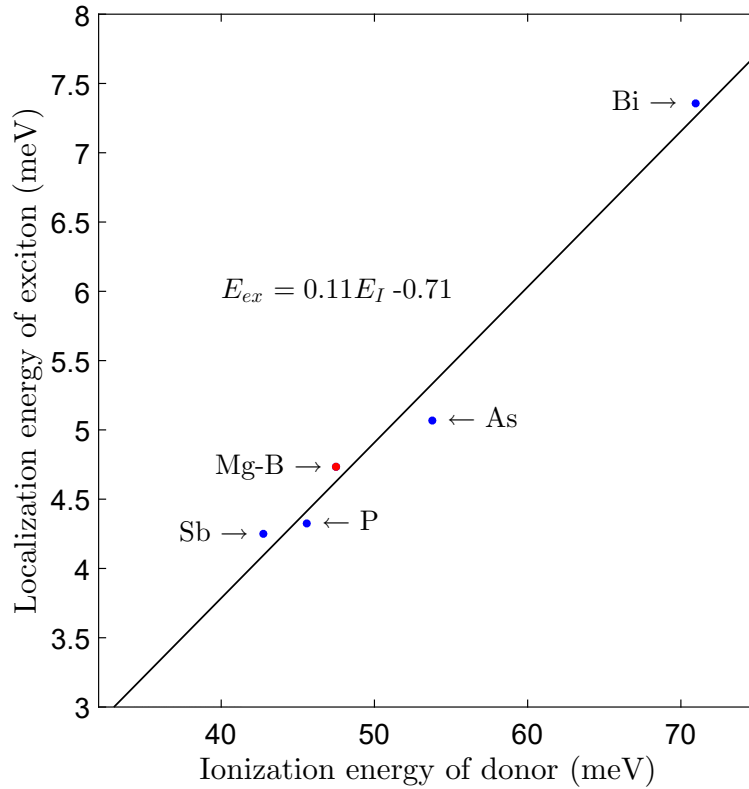


Figure 4.18: Haynes' Rule demonstrating the linear relationship between the ionization energies and BE localization energies of several group-V donors and Mg-B.

Donor	Transition energy (meV)	
	$E_{ex}$ (meV)	$E_I$ (meV)
Sb	4.25	42.763
P	4.32	45.578
Mg-B	4.73	47.50
As	5.07	53.758
Bi	7.36	70.983

Table 4.8: Ground state ionization energies ( $E_I$ ) of group-V shallow donors as seen in [101] and Mg-B as determined here. Bound exciton localization energies were determined relative to phosphorus which was consistently visible in all samples.

## Chapter 5

# Emission results

### 5.1 Raman/donor-acceptor pair band

Raman measurements were performed in an effort to observe IR-forbidden transitions from the  $1s(A_1)$  ground states of  $Mg_i^0$  and  $Mg_i^+$  to  $1s(E)$ . The results of this spectroscopy, seen in Fig. 5.1 did not reveal any sign of the  $1s(E)$  transition for either charge species. The only Raman features visible in Fig. 5.1 are the Brillouin zone center optical phonon  $O_\Gamma$ , and multi-phonon Raman line. This broad latter feature arises due to momentum conserving combinations of two or more phonons with wavevectors adding to zero. It may be that transitions to  $1s(E)$  levels are difficult to observe if for example they have extremely short lifetimes and so are exceptionally broad. We also note the presence of a number of PL features that remain unidentified. Broad phonon-assisted features seen in Fig. 5.1, known as donor-acceptor pair bands, are visible in HB samples. These represent the recombination of electrons and holes associated with spatially nearby donors and acceptors. This leaves behind ionized donors and acceptors and results in an emitted photon whose energy depends on the relative separation (i.e. Coulomb interaction) between the donor-acceptor pair. Since in any heavily doped sample these interactions will be seen over a range of separations, we observe a broad distribution for both the TO and TA phonon-assisted replicas. Labelled in Fig. 5.1 are regions centered about the energies anticipated by Ho and Ramdas [59] and those calculated by [5] for  $1s(E)$ . The regions in which we would anticipate these transitions are dominated by DAP bands in HB samples, making potential identification of what is likely a very weak feature difficult.

Though our attempts to observe the  $1s(E)$  transitions of  $Mg_i^0$  and  $Mg_i^+$  were unsuccessful, the presence of TO/TA phonon-assisted donor-acceptor pair bands in our HB samples is further indication of the presence of the shallow donor we identify as Mg-B. The energies of recombination for donor-acceptor pairs, giving rise to the DAP band luminescence may be written as seen in Eq. 2.28. From this we can estimate the donor ionization energy, given the known acceptor species, boron. First we look to the low energy edge of the TO or TA band, where separations are large and Coulomb/Van-der Waals terms can be neglected. Since we

know the ionization energy of boron, the size of the silicon band gap, and the energy of the TO or TA phonon mode the ionization energy of the donor species is easy to estimate ( $\sim 45$  meV). The number we obtain is not as accurate as our estimate calculated through direct observation in absorption of high excited states/comparison with theoretical binding energies tabulated in Pajot [101]. In particular the cutoff of the TO band is difficult to observe in Fig. 5.1 because of the position of the multi-phonon Raman feature which overlaps this region. Our previously discussed estimate for the Mg-B binding energy of 47.50 meV from absorption spectroscopy in the shallow donor region is therefore the more accurate value. These particular spectra are shown despite this since they otherwise represents our best spectra displaying the DAP features.

Some of the apparent noise seen at the high energy edges of both the TA and TO bands in Fig. 5.1 is likely caused by photon emission from donor-acceptor pairs at discrete spacings. This is a well known consequence of recombination between particularly nearby donor-acceptor pairs associated with the two inter-penetrating FCC sub-lattices that define the structure of Si.

A strong isoelectronic bound exciton line and its phonon replica are visible at  $\sim 1017$  meV. This feature has been previously suggested [10] to result from a substitutional-interstitial magnesium pair ( $\text{Mg}_s$  may be a double acceptor [120], which could result in an isoelectronic center when paired with  $\text{Mg}_i$ ). This center is discussed further in the sections that follow.

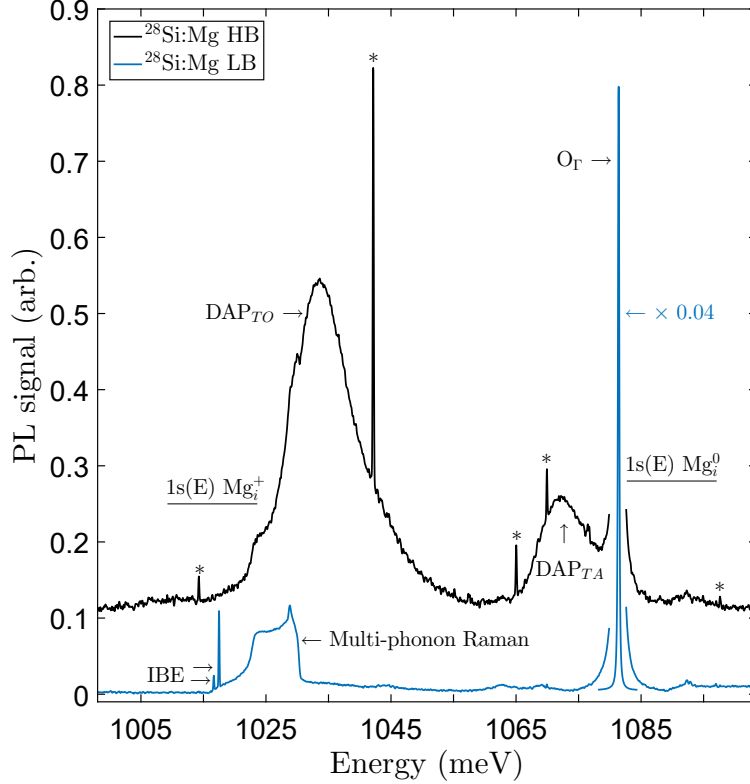


Figure 5.1: Raman spectra for HB and LB  $^{28}\text{Si}$  samples as seen using a 1080 nm excitation source with peak located at 1146.43 meV (not shown). A number of unidentified photoluminescence features that displayed no shift with changes in laser frequency (not shown) are labelled with \*. Regions in which we would have anticipated seeing  $1s(E)$  transitions based on theory are marked with horizontal lines centered about the predicted values as listed in Tab. 2.1. The Raman  $O_{\Gamma}$  [30] lines of HB and LB samples have been scaled to be of the same height and the line shown for the LB spectrum has then been scaled down by a factor of 0.04 to facilitate viewing on the same scale as other features. Visible in the HB sample are broad phonon-assisted features identified as donor-acceptor pair bands labelled  $DAP_{TO/TA}$ . Features belonging to an isoelectronic-bound exciton center, labelled IBE, are visible at  $\sim 1017$  meV. These spectra were collected at  $T = 2.1$  K with  $0.5 \text{ cm}^{-1}$  ( $\sim 0.062 \text{ meV}$ ) resolution.

## 5.2 Isoelectronic bound exciton

In the PL spectrum of the Mg-doped  $^{28}\text{Si}$  LB sample we observed a relatively strong NP feature at 1017 meV, which we label  $\text{Mg}_{NP}$ , which had been observed previously by Steinman and Grimmeiss [120] who suggested it might arise from a substitutional-interstitial Mg pair, in analogy with the well-known Be-pair IBE luminescence center [52]. Thanks to the near-elimination of inhomogeneous broadening made possible with  $^{28}\text{Si}$ , the NP line is seen to resolve into five components, as shown in Fig. 5.2. The fit to the fine structure seen in Fig. 5.2 consists of five mixed Gaussian-Lorentzian peaks with an asymmetry parameter [115] that is kept constant for all peaks. This slight asymmetric broadening to low energy

may be a consequence of Stark broadening due to random electric fields present even when using relatively lightly compensated starting material, due to Mg incorporating as both a substitutional (acceptor) and interstitial (donor) impurity.

The relative intensities of the five observed components closely match the expected relative abundances of Mg-Mg pairs with total masses ranging from 48 to 52 amu, as shown in Tab. 5.1 based on the known abundances of natural Mg (78.99(4)%  $^{24}\text{Mg}$ , 10.00(1)%  $^{25}\text{Mg}$  and 11.01(3)%  $^{26}\text{Mg}$ )[50]. The relative intensity of the the 50 amu peak for instance is predicted according to  $(0.1000(1) \times 0.1000(1)) + (0.1101(3) \times 0.7899(4)) \times 2 = 0.184(1)$ . This accounts for the possible configurations,  $^{24}\text{Mg}$ - $^{26}\text{Mg}$ ,  $^{26}\text{Mg}$ - $^{24}\text{Mg}$ , and  $^{25}\text{Mg}$ - $^{25}\text{Mg}$  that could give rise to this peak. The fact that the observed spectrum can be explained by grouping together isotope combinations having the same total mass indicates that the Mg atoms are indistinguishable from each other in terms of the NP isotope shifts, which is a common occurrence for a number of other IBE centers whose isotopic fingerprints have been studied in  $^{28}\text{Si}$  by Steger *et al.* [117]. As seen in Tab. 5.1 the spacings between the IBE components are indeed remarkably consistent with each peak  $\sim 0.011$  meV away from its neighbours. This result provides very strong confirmation for the proposal that the 1017 meV NP line observed in Mg-doped Si arises from a center containing a pair of Mg atoms.

$\Sigma\text{Mg}$ (amu)	Integrated intensity		Peak energy (meV)
	Observed	Predicted	
48	0.62(3)	0.62333(13)	1017.494
49	0.17(1)	0.15821(9)	1017.505
50	0.18(1)	0.18419(11)	1017.516
51	0.020(3)	0.02210(2)	1017.527
52	0.009(2)	0.01216(2)	1017.537

Table 5.1: Observed and predicted relative integrated intensities for peaks corresponding to Mg-Mg pairs. Total amu ranges from 48 to 52 depending on the combination of isotopes with  $^{24}\text{Mg}$ - $^{24}\text{Mg}$  comprising the largest fraction and  $^{26}\text{Mg}$ - $^{26}\text{Mg}$  the smallest. Absolute values of peak position are deemed accurate to two decimal places. Relative positions of the peaks to one another are considered valid to three decimal places.

The symmetry of this Mg-pair IBE center is not presently known. In the case of the analogous Be isoelectronic pair center, Zeeman and uniaxial stress studies [52] have established it as  $\langle 001 \rangle$  axially symmetric, having the symmetry of the  $D_{2d}$  point group. As detailed by Davies [29], this refers to a configuration in which a stress along  $\langle 001 \rangle$  and equivalent axes produces identical effects on the defects, which are aligned along the  $\langle 111 \rangle$  crystal axis.

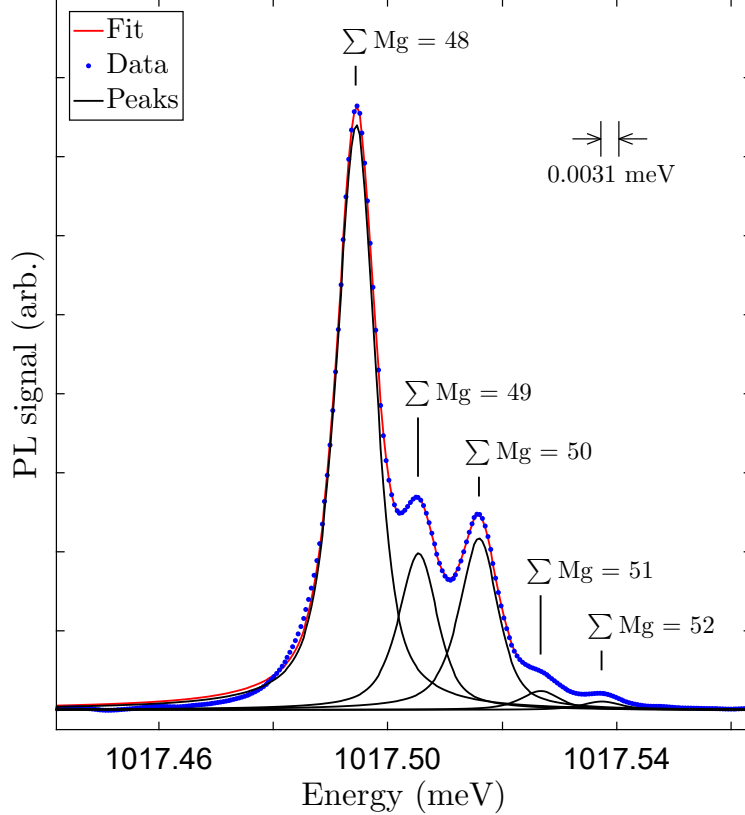


Figure 5.2: Isotopic fingerprint of the magnesium isoelectronic pair center. The mass of the pair center in amu corresponding to each possible combination of naturally occurring isotopes is labelled. Spectra were collected at a temperature of 1.4 K and a resolution of 3.1  $\mu\text{eV}$  with 1031 nm laser excitation. A fit to the fine structure consists of five mixed Gaussian-Lorentzian peaks with an asymmetry parameter of the form discussed by Aaron *et al.* [115], and seen in Eq. 4.5, that is kept constant for all peaks. This parameter  $a = 2.36$  asymmetrically skews the peaks slightly to lower energy. The peak widths  $\gamma = 8.07 \times 10^{-3}$  meV and the fraction  $f = 0.70$  are also constant for all peaks. Positions of all peaks are listed in Tab. 5.1

### 5.3 IBE temperature dependence and PL lifetime

Temperature dependence studies of the isoelectronic Mg pair center above 4.2 K show unusual behaviour as summarized in Fig. 5.3. At liquid He temperatures the  $\text{Mg}_{NP}$  line is strong and very sharp, allowing the isotopic fingerprint to be resolved at both 1.4 K and 4.2 K, and a sharp line which we label  $\text{Mg}_1$  can be observed 0.84 meV below the NP line. As 20 K is approached both the NP line and the  $\text{Mg}_1$  line vanish, only to reappear above 30 K with substantially increased linewidth and intensity, together with a new feature downshifted from the NP line by 3.0 meV, which we label  $\text{Mg}_2$ . There is no sign of the  $\text{Mg}_2$  line in the low temperature spectra. Fig. 5.4 compares the IBE spectrum at three temperatures best illustrating this unusual behaviour. Two weak features labelled with \*'s in the 25.5 K intermediate temperature spectrum shown in Fig. 5.4 are of uncertain origin, given

that the PL spectrum of this sample contain a number of weak, unidentified sharp features which may result from unintentional impurities introduced during the Mg-diffusion, and/or the complexes of such impurities with Mg. The rapid decrease in IBE PL intensity above  $\sim 37$  K, seen most clearly in Fig. 5.3 **b**, is very typical of IBE centers, and results from thermal dissociation of whichever electronic particle, the electron or the hole, that is weakly bound by Coulomb attraction to the oppositely charged more tightly bound particle.

Specific phonon and LVM replicas are very characteristic of different IBE centers, and these have not been reported previously for the Mg-pair IBE. This identification is complicated by the fact that the Mg-pair IBE luminescence in our sample does not dominate the PL spectrum as do many other IBE centers in optimized samples, and the PL spectrum of this Mg-diffused sample contains many unidentified weak but sharp lines. The replicas of the  $Mg_{NP}$  line are shown over a wider energy region in Fig. 5.5. Many unlabelled features, particularly in the intermediate temperature spectrum where the Mg-pair IBE features vanish, likely result from other impurities introduced during the Mg diffusion. These could include transition metals and/or lithium or potentially complexes containing more than two Mg atoms.

However, the unusual temperature dependence of the Mg-pair IBE PL can be used to associate features which are replicas of the  $Mg_{NP}$  line, and reject unknown features which behave differently, as already shown in Fig. 5.4 for the  $Mg_1$  and  $Mg_2$  lines. In Table 5.2 we summarize the energy shifts of these lower-energy features which we believe are associated with the Mg-pair IBE. With a shift of only 0.84 meV, the  $Mg_1$  feature is unlikely to result from a vibronic replica, but may instead originate in another electronic state of the Mg-pair IBE. The  $Mg_2$  feature, which appears only in the high temperature regime, has a shift which is more compatible with LVM replicas seen for other IBE in silicon [118]. The strong  $Mg_{10}$  replica has a shift of 65.28 meV, very close to the 65.03 meV energy of the zone-center optical phonon energy measured using Raman scattering in these  $^{28}\text{Si}$  samples.

The identification of  $Mg_3$  as a replica of the Mg-pair IBE is tentative, as an unknown line, seen in the intermediate temperature spectrum of Fig. 5.5, is superimposed on it. The  $Mg_{11}$  feature, which is observed only in the high temperature spectra, may be a combination of the emission of the modes responsible for  $Mg_2$  and  $Mg_{10}$ .

The integrated intensities of the IBE no-phonon line seen in Fig. 5.3 are re-normalized by the intensity of the zone center optical phonon  $O_\Gamma$  Raman line in which we observe a slight drop-off with increasing temperature. The origin of this small temperature dependence is unknown. The optical phonon mode associated with this feature should remain unchanged in the temperature range studied.

A small rise in intensity at  $\sim 10$  K of the main no-phonon line, seen in Fig.5.3, may be consistent with an increase in free exciton concentration as shallow acceptor/donor species like boron and lithium become thermally dissociated. This is seen most clearly based on the TO-assisted phonon features of these shallow donors and acceptors, which are completely

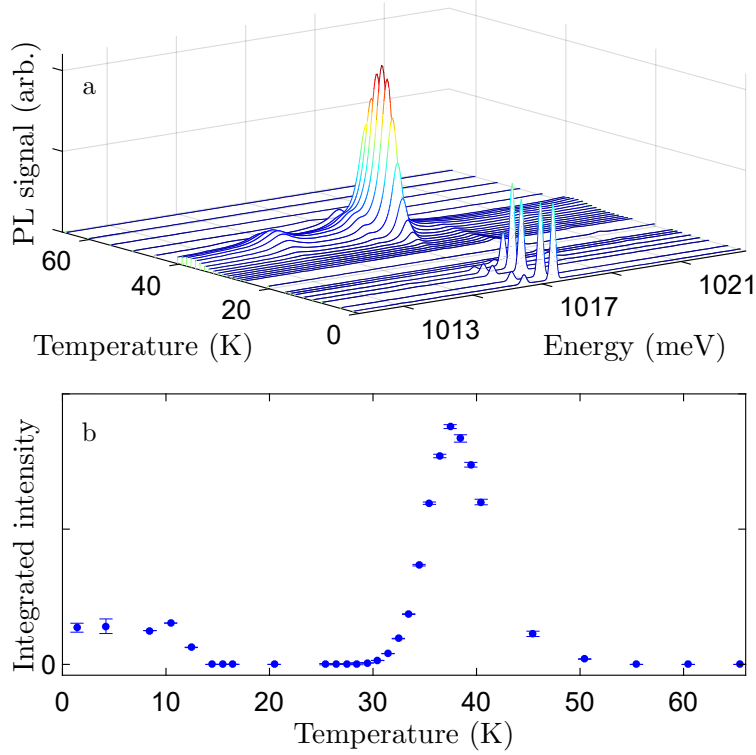


Figure 5.3: **(a)** Waterfall plot showing the temperature dependence of the Mg-Mg IBE line and replicas. Up to  $\sim 10$  K the IBE features are relatively unchanged, but then decrease rapidly with increasing temperature until they disappear completely above  $\sim 17$  K. A resurgence of the IBE PL with increased linewidth and intensity along with a new LVM phonon replica become visible above  $\sim 30$  K. Spectra were collected at a resolution of 0.12 meV. **(b)** Integrated intensity of the  $Mg_{NP}$  line as a function of temperature.

Label	Shift from $Mg_{NP}$ (meV)
Mg <sub>1</sub>	0.84
Mg <sub>2</sub>	3.02
Mg <sub>3</sub>	7.2
Mg <sub>4</sub>	28.4
Mg <sub>5</sub>	31.2
Mg <sub>6</sub>	46.6
Mg <sub>7</sub>	49.0
Mg <sub>8</sub>	59.3
Mg <sub>9</sub>	61.6
Mg <sub>10</sub>	65.28
Mg <sub>11</sub>	68.3

Table 5.2: Energy shifts below the  $Mg_{NP}$  line of luminescence features which are believed to be related to the Mg-pair IBE. The  $Mg_{11}$  replica, which like  $Mg_2$  is only observed in high temperature spectra, likely results from the emission of the modes responsible for the  $Mg_2$  replica plus the mode responsible for the  $Mg_{10}$  replica.

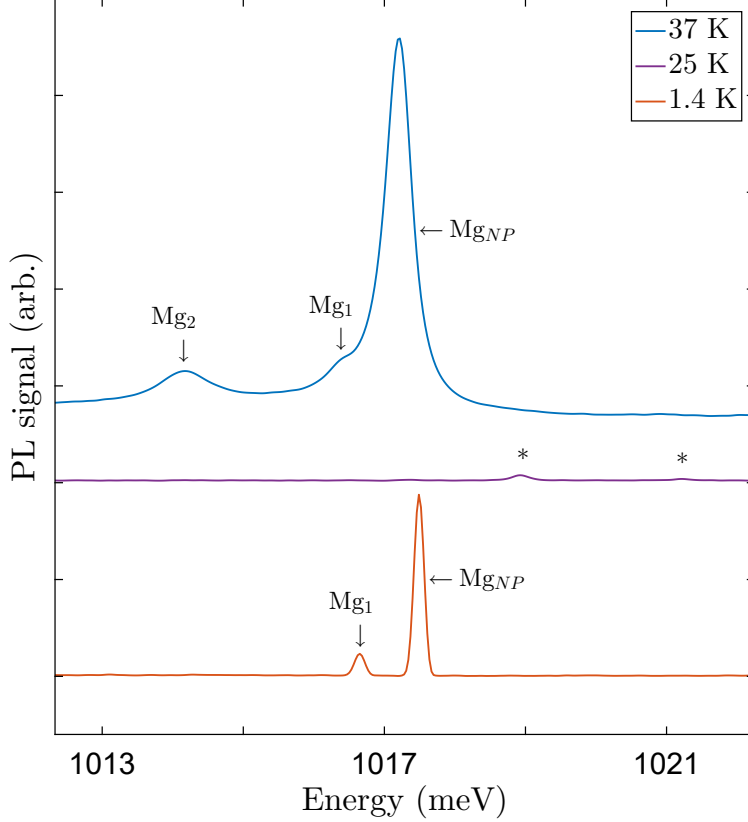


Figure 5.4: Example spectra showing the  $Mg_{NP}$  line and associated features  $Mg_1$  and  $Mg_2$  in the high, intermediate, and low temperature regimes. Spectra were collected at a resolution of 0.12 meV.

gone beyond  $\sim 10$  K, with a corresponding increase in the area of the free exciton feature as seen in Fig. 5.7. The same behaviour is seen in the weaker TA-assisted features and the NP line of boron. Lithium is known to have a small central cell splitting of opposite sign to most donors, resulting in a very shallow center that produces no visible NP transition. Larger error bars on the 4.2 K data point are consistent with bubbling noise in liquid helium at atmospheric pressure. The position of the IBE peak shifts down in energy with increasing temperature as the silicon band-gap shrinks. The shift is slower than the actual reduction of the band-gap since the IBE is a deep center and is not expected to follow these changes precisely.

Model data for bandgap shift as a function of temperature in Fig. 5.6 is given according to the following four parameter model discussed by Pässler [102],

$$E(T) = E(0) - \frac{a\Theta_p}{2} \left[ \sqrt[p]{1 + \left(\frac{2T}{\Theta_p}\right)^p} - 1 \right]. \quad (5.1)$$

Here  $E(0) = 1.170$  eV the size of the Si bandgap at  $T = 0$  K and  $\Theta_p = 406$  K approximately equal to the average phonon temperature. This, as discussed by Pässler, corresponds to

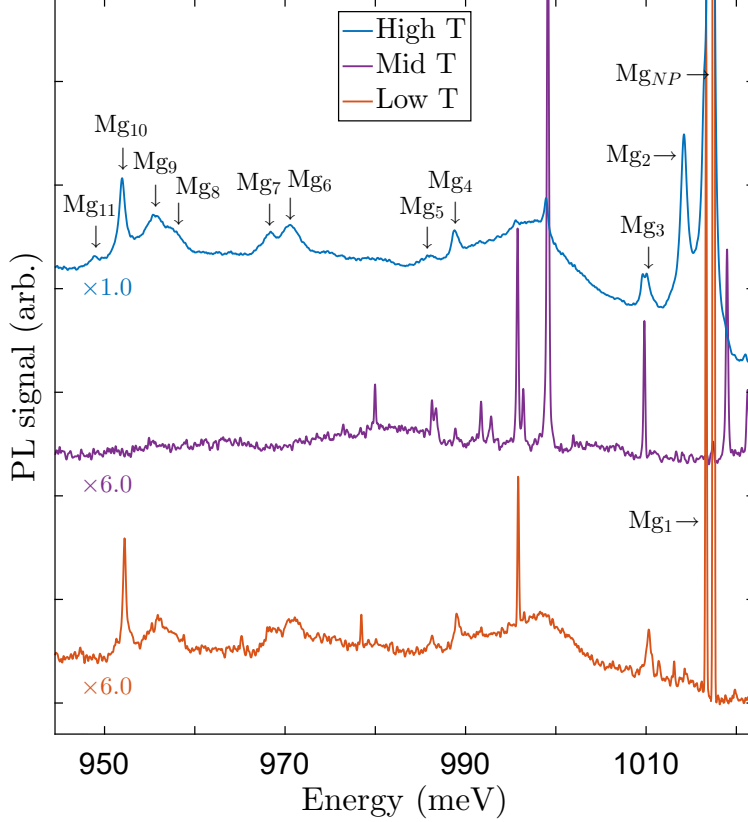


Figure 5.5: PL spectra of the main  $Mg_{NP}$  line and a range of features below it in energy in three temperature regimes. For improved SNR we have averaged spectra at 35, 36 and 37 K to show the high temperature regime. Similarly, spectra at 16, 20, and 25 K are averaged to show the middle regime, and spectra at 1.4 and 4.2 K are averaged to show the low temperature regime. We note a number of features, labelled  $Mg_1$ - $Mg_{11}$  that display a similar temperature dependence to the main NP line that are likely related to the Mg-pair IBE. Many relatively narrow PL features of unknown origin, but with a different temperature dependence, most notable in the mid T regime, are also observed but not labelled. The low and mid temperature spectra have been scaled up by a factor of 6.0 to make the areas of the  $Mg_{NP}$  line in the low and high temperature spectra approximately equal for ease of comparison of the replicas. For the high and low temperature spectra, the peaks of the main  $Mg_{NP}$  line are truncated at the top edge of the plot, and the peak of the  $Mg_1$  line in the low temperature spectrum lies at the top edge of the plot. Spectra were collected at a resolution of 0.12 meV. The temperature dependence of the  $Mg_1$  and  $Mg_2$  features relative to the  $Mg_{NP}$  line is better seen in Fig. 5.4.

an effective phonon energy of approximately 35 meV. The parameter  $p = 2.33$  and  $a = 0.318$  meV/K is the limiting magnitude of the slope of  $E(T)$ . These values are specific to silicon, with a table provided by Pässler for Si-specific parameters along with those for a range of other semiconductors determined through fits to experimental data.

Photoluminescence lifetime measurements were performed to try to understand the unusual temperature dependence of the IBE intensity. However as the results seen in Fig. 5.9

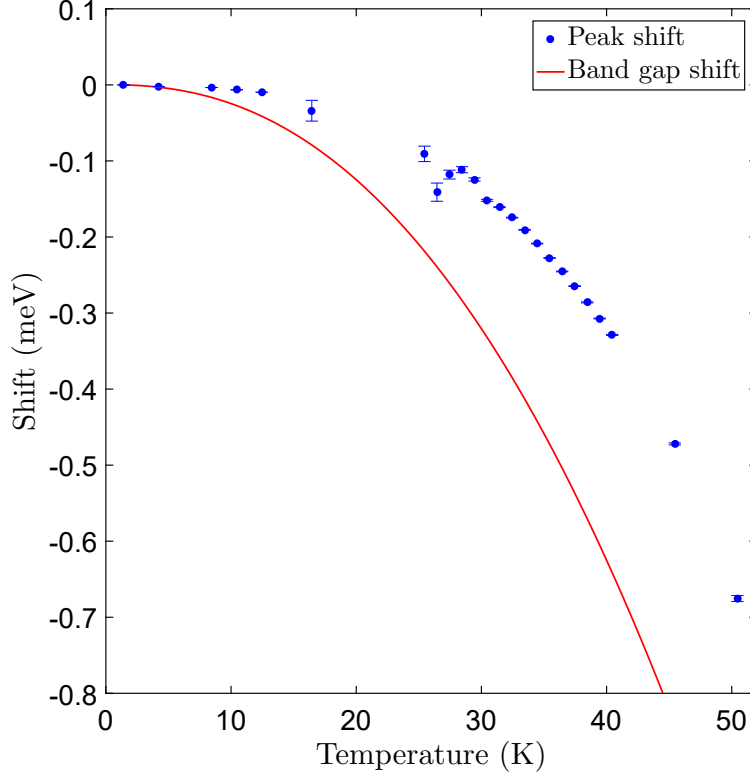


Figure 5.6: Here we see (blue data points) the shift of the IBE peak with temperature. This follows the same path, albeit more slowly as the red curve, which tracks the predicted reduction of the Si band-gap as a function of temperature according to a model discussed by Pässler [102].

reveal, the lifetime seems to scale quite consistently with the IBE peak intensity. If lifetime broadening was a component of its behaviour, we would anticipate decreased PL lifetime in the high-temperature/large linewidth regime, which is the opposite of what we observe. We also note a rise-time that consistently precedes the PL decay of our IBE signal. We first considered that this might be a heating issue with the laser pulse distorting the decay-transient.

Our sample dimensions were  $10\text{ mm} \times 5\text{ mm} \times 2\text{ mm}$  comprising  $\sim 0.008$  mol of silicon. We had  $\sim 1\text{ W}$  of laser power delivered to the sample in a  $1\text{ }\mu\text{s}$  pulse. Based on Si heat capacities listed by Desai [31] for a range of temperatures we determined that this was not likely the primary cause given the continued presence of this feature at higher temperatures/correspondingly larger heat capacities.

At very low temperatures, i.e. sub-lambda, heating from laser power could be significant since below the lambda point the heat capacity of silicon drops sharply. At 1 K we might have expected the temperature to rise as high as  $\sim 2.8\text{ K}$ , but above the helium-lambda point the changes are less significant. For example starting from 5 K we would anticipate a smaller increase to  $\sim 5.1\text{ K}$ . These temperature changes represent a lower bound on what could occur

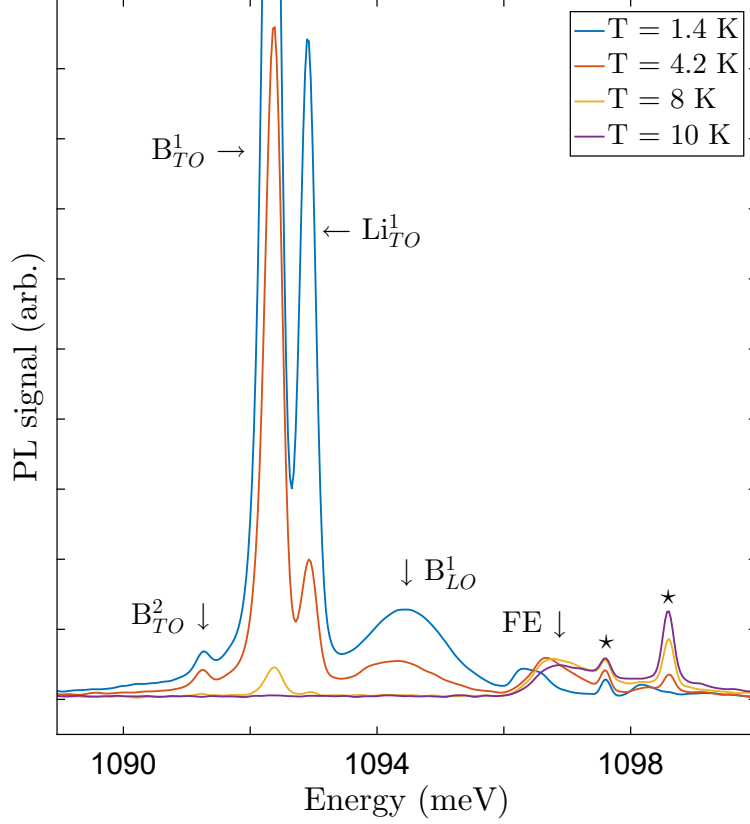


Figure 5.7: Here we show the boron and lithium TO phonon replicas as they vanish with increasing temperature. By 10K they have completely ionized and there is a corresponding increase in the intensity of the free exciton feature. PL features of unknown origin on top of the free-exciton feature (FE) are labelled  $\star$ .

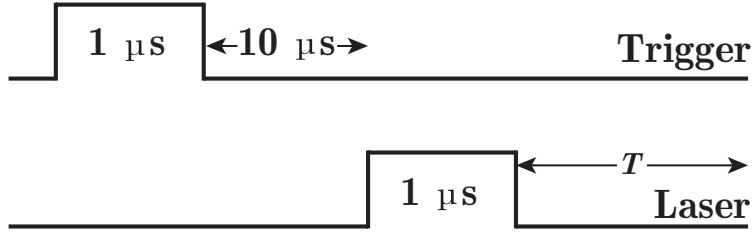


Figure 5.8: Schematic of the pulse/trigger sequence supplied to perform the PL-lifetime measurements. The trigger pulse starts the clock of the multichannel scaler (MCS), which bins photon counts as a function of time after the trigger pulse.

given that the Kapitza resistance  $R_k$  between silicon and helium would also play a role. Data collected by Amrit *et al.* [7] indicates a temperature dependence  $R_k = 38.72T^{-3.41}$  between 0.4 and 2.1 K for the  $\langle 111 \rangle$  silicon-liquid helium interface. It is also possible that at elevated temperatures we are seeing free excitons simply take longer to be captured by and subsequently annihilate at the Mg-pair center. Fits to the two relevant time scales, the rise time and subsequent decay are indicated in Fig. 5.10, with  $t_2$  the rise time constant and  $t_1$

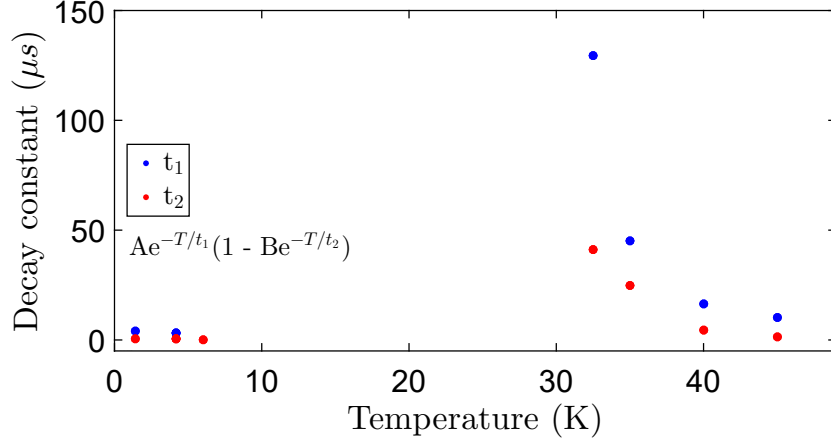


Figure 5.9: Photoluminescence lifetime of the Mg-pair IBE as a function of temperature, with decay time  $t_1$  and rise time  $t_2$ . Temperature and lifetime values plotted here are listed in Tab. 5.3.

the subsequent decay constant. We note that the PL lifetime in the high temperature limit, where the linewidth of the IBE feature is vastly increased is also much higher, and that the rise time has also increased. In the high temperature regime we note a steady drop-off of both decay constant and rise time as a function of temperature.

Temperature (K)	$t_1$ ( $\mu s$ )	$t_2$ ( $\mu s$ )
1.4	3.99	0.41
4.2	3.15	0.32
6	-	0.11
32.5	129.6	41.14
35	45.30	25.01
40	16.44	4.52
45	10.20	1.36

Table 5.3: Values of  $t_1$  and  $t_2$  associated with the photoluminescence lifetime of the Mg-pair IBE, as seen plotted in Fig. 5.9.

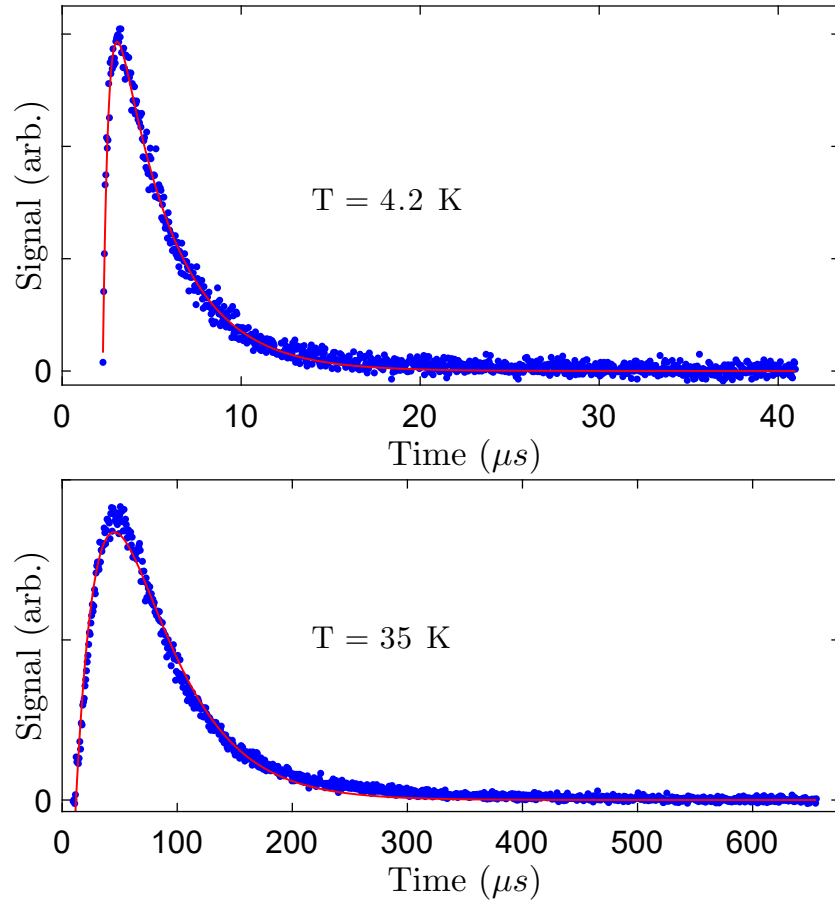


Figure 5.10: Here we see the characteristic decay of the PL signal from the main IBE NP line in the two main temperature regimes where it is visible. The lifetime in the high temperature regime, where the linewidth is much larger than in the low temperature regime, is clearly significantly longer. The Spex grating spectrometer used to collect these data had a resolution of  $\sim 21 \text{ \AA}/\text{mm}$  which, used with the input and exit slits set at 3 mm, gave an effective resolution of  $\sim 5.3 \text{ meV}$  at the wavelength of interest here.

## 5.4 Future work

Magnesium has been found to form a shallow donor complex with boron, and there has been some previous suggestion that it may do the same with other impurities [86]. Experiments to determine whether this behaviour is reproduced in samples containing other group-III acceptors, including aluminium, indium, and gallium will likely follow. If the behaviour is similar, we would anticipate a clear no-phonon transition for each of these potential complexes in PL and the corresponding donor signature in absorption. From the binding energies of the donor ground states and localization energies of the NP BE transitions we would further expect consistency with Hayne's Rule.

Additionally, there has been some suggestion that we might infer the positions of the valley orbit states  $1s(E)$  and  $1s(T_2)$  through temperature dependence measurements. It is likely that if anything, this would only be observable for the neutral species  $Mg_i^0$ , since the much larger transition energies in the singly ionized species would make such thermal activation unlikely. In such measurements we would anticipate thermal activation from  $1s(A_1)$  to  $1s(E)$  and  $1s(T_2)$ . Optical transitions from the thermally populated levels to the next closest excited states, like  $2p_0$  and  $2p_{\pm}$  could then be observed in absorption. From the subsequent temperature vs. integrated intensity relation we could extract activation energies from the slopes of Arrhenius plots such as those constructed in Fig. 4.14. From these spacings/activation energies, and the known binding energy of the  $Mg_i^0$  donor, one could infer the position of  $1s(E)$  and  $1s(T_2)$ .

The photoluminescence spectrum of our Mg samples proved to be very complex, including many features we were ultimately unable to identify. Temperature dependence studies in particular, revealed unusual behaviour of not only the Mg-pair IBE, but of many other features with apparently similar temperature dependence. Some of these we are able to identify as Mg-related as seen in Fig. 5.5. One of these in particular, a likely IBE center that appears as a triplet, is displayed in Fig. 5.11. Unfortunately as components of this feature were either wholly invisible or simply too weak until elevated temperatures, determining its identity through its isotopic fingerprint proved impossible, with the line too broadened by the time it was visible to reveal isotopic fine structure. Unlike the Mg-pair center this feature never disappears entirely, though it shares a similar resurgence in intensity, if not in linewidth after  $\sim 30$  K.

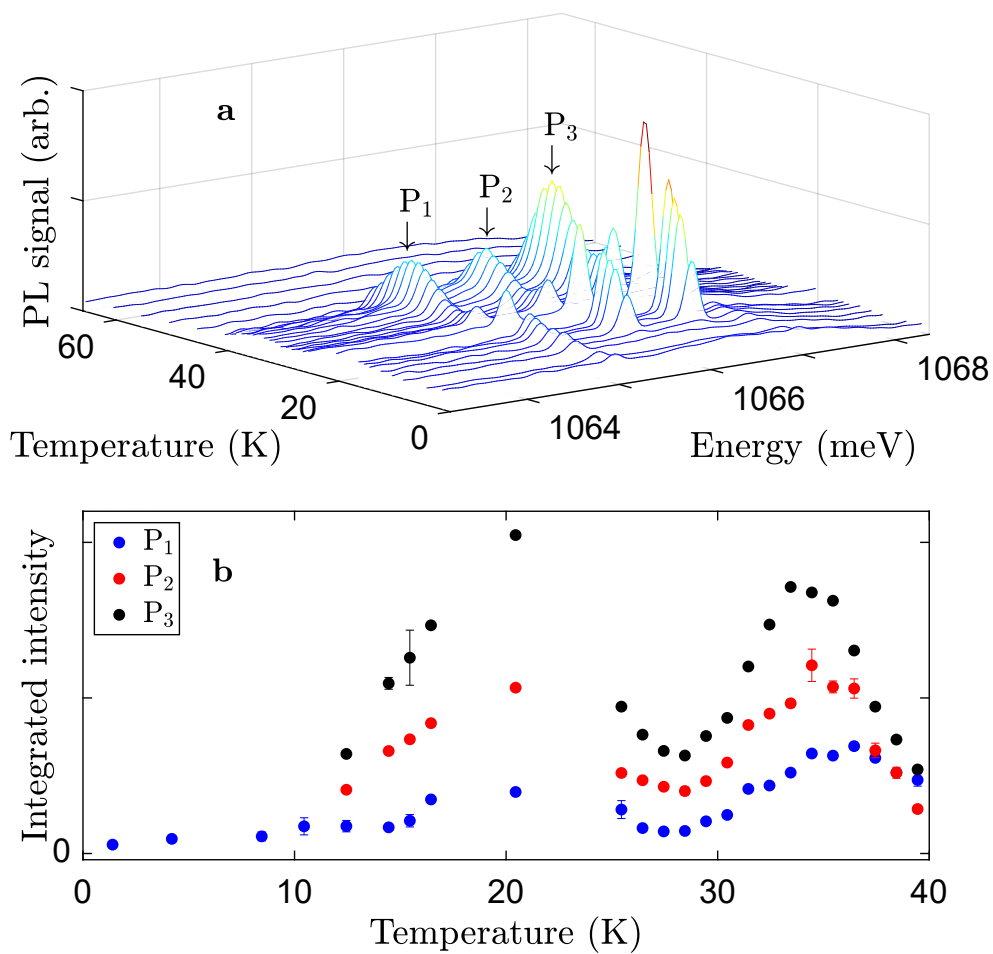


Figure 5.11: (a) Waterfall plot of the triplet center with peaks P<sub>1</sub>-P<sub>3</sub>. This represents a likely isoelectronic center with similar temperature dependence to the Mg IBE feature. (b) Integrated intensities of the triplet IBE feature as a function of temperature. Components P<sub>1</sub>-P<sub>3</sub> of the triplet are listed from lowest to highest energy as indicated in (a).

## Chapter 6

# Conclusions

Our measurements have led to new interpretations for/discovery of a number of new features in magnesium-diffused silicon. A magnesium center previously observed in other work has been interpreted as  $Mg_i$  in a reduced symmetry configuration,  $Mg_{i*}$ , either as a consequence of an alternate interstitial site or complexing with another impurity. Evidence currently lends weight to the latter possibility with an anneal/quench procedure showing signs of breaking up a likely Mg-related complex. Carbon was initially the primary suspect for the  $Mg_{i*}$  complex since  $Mg_{i*}$  appears as a double donor, which implies complexing with a species that is electronically neutral in silicon. Further investigations involving an Mg-diffused sample with relatively high carbon content to examine the impact on  $Mg_{i*}$  centers eliminated this possibility, revealing no enhancement of the  $Mg_{i*}$  features relative to the standard  $Mg_i$ . The exact composition of the complex remains unknown. Another possibility is that  $Mg_{i*}$  represents Mg associated with a neutral damage center of some description, in which case irradiation of Mg-diffused samples in an effort to create more such centers might prove informative. Stress studies to establish the symmetry of this center, allowing for a more quantitative discussion of the anticipated splitting of spectral features, could also follow.

A new shallow donor center, observed for the first time in absorption, is identified as an Mg-B complex. Work to determine the origins of a different Mg-? shallow donor center by studying potential shallow donor complexes formed with other Group III acceptors such as gallium, indium and aluminum is ongoing. The Mg-B complex is also seen in our photoluminescence results, revealing in emission the no-phonon/phonon replica transitions of the Mg-B donor BE.

We were not able to observe any of the  $1s$  to  $1s$  transitions in our current samples either for  $1s(T_2)$  in absorption using FTIR spectroscopy or  $1s(E)$  via Raman measurements. Further attempts to observe the  $1s(T_2)$  transition of  $Mg_i^+$  in absorption could be made in samples with a much higher ratio of boron to magnesium so that all the donors present would be ionized. This would preclude any potential overlap with the neutral species lines allowing observation of what could be a very weak feature. It may also be that the  $1s(E)$

and  $1s(T_2)$  transitions are present but have very short lifetimes and are therefore very broad and difficult to detect.

We have studied the PL spectrum of highly enriched  $^{28}\text{Si}$  diffused with Mg to reexamine a luminescence line near 1017 meV previously observed in the PL spectrum of natural Si doped with Mg by Steinman and Grimmeiss [120] and proposed by them to be an IBE localized on a Mg-pair center. The isotopic fingerprint of this center made possible by the near-elimination of inhomogeneous broadening in  $^{28}\text{Si}$  provides strong confirmation that the binding center of this IBE contains two Mg atoms. A number of lower energy replicas of the main  $\text{Mg}_{NP}$  line were identified.

The behaviour of the PL of this IBE center with changing sample temperature is very unusual, and to the best of our knowledge is unique in Si. From pumped He temperature to  $\sim 10\text{ K}$  there is little change in the spectrum, but from  $\sim 10\text{ K}$  to  $\sim 17\text{ K}$  the intensity of all components decreases and vanishes from  $\sim 20\text{ K}$  to  $\sim 30\text{ K}$ , above which temperature it reappears with increased intensity and NP linewidth, and a new replica downshifted by 3.02 meV which cannot be observed in the low temperature spectrum. Above  $\sim 37\text{ K}$  all components decrease in intensity, and disappear above  $\sim 50\text{ K}$ . This last behaviour is familiar for all IBE, and results from the thermal dissociation of the weakly-bound electronic particle of the IBE.

The disappearance of all IBE PL between  $\sim 20\text{ K}$  and  $\sim 30\text{ K}$ , and its reappearance above  $\sim 30\text{ K}$  with increased intensity and NP linewidth, and with a new LVM replica, at present has no explanation. Any further studies of the Mg-pair IBE would benefit from a careful optimization of the diffusion and annealing conditions which could maximize its intensity. Maximizing the total Mg concentration is known to not be optimal, as such samples have extremely weak PL, likely due to nonradiative recombination at Mg-precipitates as suggested by Steinman and Grimmeiss [120].

# Bibliography

- [1] R. J. S. Abraham, A. DeAbreu, K. J. Morse, V. B. Shuman, L. M. Portsel, A. N. Lodygin, Yu. A. Astrov, N. V. Abrosimov, S. G. Pavlov, H.-W. Hübers, S. Simmons, and M. L. W. Thewalt. Further investigations of the deep double donor magnesium in silicon. *Phys. Rev. B*, 98:045202, Jul 2018.
- [2] R. J. S. Abraham, A. DeAbreu, K. J. Morse, V. B. Shuman, L. M. Portsel, A. N. Lodygin, Yu. A. Astrov, N. V. Abrosimov, S. G. Pavlov, H.-W. Hübers, S. Simmons, and M. L. W. Thewalt. Mg-pair isoelectronic bound exciton identified by its isotopic fingerprint in  $^{28}\text{Si}$ . *Phys. Rev. B*, 98:205203, Nov 2018.
- [3] R. L. Aggarwal, P. Fisher, V. Mourzine, and A. K. Ramdas. Excitation spectra of lithium donors in silicon and germanium. *Phys. Rev.*, 138:A882–A893, May 1965.
- [4] M. Altarelli. Substitutional donors and core excitons in many-valley semiconductors. *Phys. Rev. Lett.*, 46:205–208, Jan 1981.
- [5] M. Altarelli. Excited states of double donors in silicon. *Physica B+C*, 117:122–124, March 1983.
- [6] M. Altarelli, W. Y. Hsu, and R. A. Sabatini. Donor binding energies in multivalley semiconductors. *Journal of Physics C: Solid State Physics*, 10(21):L605, 1977.
- [7] J. Amrit and J. P. Thermeau. Measurements of the kapitza resistance between silicon and helium from 0.4 k to 2.1 k. *Journal of Physics: Conference Series*, 150(3):032002, 2009.
- [8] H. Atzmüller and U. Schröder. Theoretical investigations of haynes’ rule. *physica status solidi (b)*, 89(2):349–356, 1978.
- [9] Leon B. Radiationless recombination in phosphors. *Phys. Rev.*, 111:129–132, Jul 1958.
- [10] N. Baber, L. Montelius, M. Kleverman, K. Bergman, and H. G. Grimmeiss. Evidence for a substitutional mg acceptor level in silicon. *Phys. Rev. B*, 38:10483–10489, Nov 1988.
- [11] J. A. Baker, T. N. Tucker, N. E. Moyer, and R. C. Buschert. Effect of carbon on the lattice parameter of silicon. *Journal of Applied Physics*, 39(9):4365–4368, 1968.
- [12] A. Baldereschi and J. J. Hopfield. Binding to isoelectronic impurities in semiconductors. *Phys. Rev. Lett.*, 28:171–174, Jan 1972.

- [13] Walter Baltensperger. Cxliii. on conduction in impurity bands. *The London, Edinburgh, and Dublin Philosophical Magazine and Journal of Science*, 44(359):1355–1363, 1953.
- [14] Robert Barrie and Kyoji Nishikawa. Phonon broadening of impurity spectral lines: Ii. application to silicon. *Canadian Journal of Physics*, 41(11):1823–1835, 1963.
- [15] J. E. Baxter and G. Ascarelli. A comparative electron-spin-resonance study of the ground state and a photoconverted metastable state of the  $\text{mg}^+$  donor in silicon. *Phys. Rev. B*, 7:2630–2639, Mar 1973.
- [16] R. Car and A. Selloni. Local-field effects in the screening of impurities in silicon. *Phys. Rev. Lett.*, 42:1365–1368, May 1979.
- [17] R. Car, A. Selloni, and M. Altarelli. Local field corrections to binding energies of substitutional and interstitial donors in si and ge. *Solid State Communications*, 39(9):1013 – 1016, 1981.
- [18] M. Cardona and M. L. W. Thewalt. Isotope effects on the optical spectra of semiconductors. *Rev. Mod. Phys.*, 77:1173–1224, Nov 2005.
- [19] R. O. Carlson. Double-acceptor behavior of zinc in silicon. *Phys. Rev.*, 108:1390–1393, Dec 1957.
- [20] T. G. Castner. Orbach spin-lattice relaxation of shallow donors in silicon. *Phys. Rev.*, 155:816–825, Mar 1967.
- [21] D. B. Chase. Phase correction in ft-ir. *Appl. Spectrosc.*, 36(3):240–244, May 1982.
- [22] Marvin L. Cohen and T. K. Bergstresser. Band structures and pseudopotential form factors for fourteen semiconductors of the diamond and zinc-blende structures. *Phys. Rev.*, 141:789–796, Jan 1966.
- [23] Konrad Colbow. Infrared absorption lines in boron-doped silicon. *Canadian Journal of Physics*, 41(11):1801–1822, 1963.
- [24] J. Connes. Spectroscopic studies using fourier transformations. *Rev. Opt.*, 45(40), 1961.
- [25] H. Conzelmann. Photoluminescence of transition metal complexes in silicon. *Applied Physics A*, 42(1):1–18, Jan 1987.
- [26] Alan Corney. *Atomic and Laser Spectroscopy*. Clarendon Press, Oxford, 1977.
- [27] R. K. Crouch, J. B. Robertson, and T. E. Gilmer. Study of beryllium and beryllium-lithium complexes in single-crystal silicon. *Phys. Rev. B*, 5:3111–3119, Apr 1972.
- [28] G. Davies. Approximate widths of zero phonon lines broadened by point defect strain fields. *Journal of Physics D: Applied Physics*, 4(9):1340, 1971.
- [29] G Davies. A simple model for excitons bound to axial isoelectronic defects in silicon. *Journal of Physics C: Solid State Physics*, 17(35):6331, 1984.

- [30] Gordon Davies. The optical properties of luminescence centres in silicon. *Physics Reports*, 176(3):83 – 188, 1989.
- [31] P. D. Desai. Thermodynamic properties of iron and silicon. *Journal of Physical and Chemical Reference Data*, 15(3):967–983, 1986.
- [32] G. G. Devyatykh, A. D. Bulanov, A. V. Gusev, I. D. Kovalev, V. A. Krylov, A. M. Potapov, P. G. Sennikov, S. A. Adamchik, V. A. Gavva, A. P. Kotkov, M. F. Churbanov, E. M. Dianov, A. K. Kaliteevskii, O. N. Godisov, H. J. Pohl, P. Becker, H. Riemann, and N. V. Abrosimov. High-purity single-crystal monoisotopic silicon-28 for precise determination of avogadro’s number. *Doklady Chemistry*, 421(1):157–160, Jul 2008.
- [33] R. N. Dexter, Benjamin Lax, A. F. Kip, and G. Dresselhaus. Effective masses of electrons in silicon. *Phys. Rev.*, 96:222–223, Oct 1954.
- [34] D. W. Ditchburn. *Light*. Academic Press, New York, 3rd edition, 1976.
- [35] Rezgui Béchir Dridi, Veirman Jordi, Dubois Sébastien, and Palais Olivier. Study of donor acceptor pair luminescence in highly doped and compensated cz silicon. *physica status solidi (a)*, 209(10):1917–1920.
- [36] W. C. Dunlap and R. L. Watters. Direct measurement of the dielectric constants of silicon and germanium. *Phys. Rev.*, 92:1396–1397, Dec 1953.
- [37] R. Englman and J. Jortner. The energy gap law for radiationless transitions in large molecules. *Molecular Physics*, 18(2):145–164, 1970.
- [38] M. L. Forman, W. H. Steel, and G. A. Vanasse. Correction of asymmetric interferograms obtained in fourier spectroscopy. *J. Opt. Soc. Am.*, 56(1):59–63, Jan 1966.
- [39] R.K. Franks and J.B. Robertson. Magnesium as a donor impurity in silicon. *Solid State Communications*, 5(6):479 – 481, 1967.
- [40] Sverre Froyen and Alex Zunger. Metastable impurities in semiconductors: Si:mg and si:be. *Phys. Rev. B*, 34:7451–7454, Nov 1986.
- [41] D. J. Griffiths and D. F. Schroeter. *Introduction to Quantum Mechanics*. Cambridge University Press, 3 edition, 2018.
- [42] H. G. Grimmeiss. Deep level impurities in semiconductors. *Annual Review of Materials Science*, 7(1):341–376, 1977.
- [43] H. G. Grimmeiss, E. Janzén, and K. Larsson. Multivalley spin splitting of 1s states for sulfur, selenium, and tellurium donors in silicon. *Phys. Rev. B*, 25:2627–2632, Feb 1982.
- [44] H. G. Grimmeiss, E. Janzén, and K. Larsson. Multivalley spin splitting of 1s states for sulfur, selenium, and tellurium donors in silicon. *Phys. Rev. B*, 25:2627–2632, Feb 1982.
- [45] H. G. Grimmeiss, E. Janzén, and B. Skarstam. Deep sulfur-related centers in silicon. *Journal of Applied Physics*, 51(8):4212–4217, 1980.

- [46] H. G. Grimmeiss, E. JanzÅln, and B. Skarstam. Electronic properties of seleniumÅR-doped silicon. *Journal of Applied Physics*, 51(7):3740–3745, 1980.
- [47] G. Grossmann, K. Bergman, and M. Kleverman. Spectroscopic studies of double donors in silicon. *Physica B+C*, 146(1):30 – 46, 1987.
- [48] Morton Hamermesh. *Group theory and its application to physical problems*. Addison-Wesley, Reading, MA, 1962.
- [49] J. R. Haynes. Experimental proof of the existence of a new electronic complex in silicon. *Phys. Rev. Lett.*, 4:361–363, Apr 1960.
- [50] W. M. Haynes. *CRC Handbook of Chemistry and Physics, 97th Edition*. CRC Press, 2016.
- [51] V. Heine and C. H. Henry. Theory of the isotope shift for zero-phonon optical transitions at traps in semiconductors. *Phys. Rev. B*, 11:3795–3803, May 1975.
- [52] M. O. Henry, E. C. Lightowers, N. Killoran, D. J. Dunstan, and B. C. Cavenett. Bound exciton recombination in beryllium-doped silicon. *Journal of Physics C: Solid State Physics*, 14(10):L255, 1981.
- [53] M. O. Henry, K. G. McGuigan, M. C. do Carmo, M. H. Nazare, and E. C. Lightowers. A photoluminescence investigation of local mode vibrations of the beryllium pair centre in silicon. *Journal of Physics: Condensed Matter*, 2(48):9697, 1990.
- [54] M.O. Henry, D.J. Beckett, A.G. Steele, M.L.W. Thewalt, and K.G. McGuigan. A zinc-related isoelectronic bound exciton in silicon. *Solid State Communications*, 66(7):689 – 694, 1988. 25th Anniversary Year.
- [55] Robert C. Hilborn. Einstein coefficients, cross sections, f values, dipole moments, and all that. *American Journal of Physics*, 50(11):982–986, 1982.
- [56] L. T. Ho. Magnesium oxygen complex impurities in silicon. *physica status solidi (b)*, 210(2):313–316, 1998.
- [57] L. T. Ho. Singly ionized magnesium oxygen complex impurities in silicon. *physica status solidi (c)*, 0(2):721–725, 2003.
- [58] L. T. Ho, F. Y. Lin, and W. J. Lin. Infrared absorption spectrum of singly ionized magnesium donors in silicon. *International Journal of Infrared and Millimeter Waves*, 14(5):1099–1106, May 1993.
- [59] L. T. Ho and A. K. Ramdas. Excitation spectra and piezospectroscopic effects of magnesium donors in silicon. *Phys. Rev. B*, 5:462–474, Jan 1972.
- [60] L.T. Ho. Spectroscopic study of magnesium-related impurities in silicon. In *Defects and Diffusion in Semiconductors, 2003*, volume 221 of *Defect and Diffusion Forum*, pages 41–50. Trans Tech Publications, 11 2003.
- [61] L.T. Ho. Multiple neutral and singly ionized magnesium donors in silicon. *Physica B: Condensed Matter*, 376-377:154 – 156, 2006. Proceedings of the 23rd International Conference on Defects in Semiconductors.

- [62] J. J. Hopfield, D. G. Thomas, and R. T. Lynch. Isoelectronic donors and acceptors. *Phys. Rev. Lett.*, 17:312–315, Aug 1966.
- [63] A. A. Istratov, H. Hieslmair, T. Heiser, C. Flink, and E. R. Weber. The dissociation energy and the charge state of a copper-pair center in silicon. *Applied Physics Letters*, 72(4):474–476, 1998.
- [64] C. Jagannath, Z. W. Grabowski, and A. K. Ramdas. Linewidths of the electronic excitation spectra of donors in silicon. *Phys. Rev. B*, 23:2082–2098, Mar 1981.
- [65] C. Jagannath, Z.W. Grabowski, and A.K. Ramdas. A high resolution study of the excitation spectrum of phosphorus donors introduced in silicon by neutron transmutation. *Solid State Communications*, 29(4):355 – 359, 1979.
- [66] Varun Jain, Mark C. Biesinger, and Matthew R. Linford. The gaussian-lorentzian sum, product, and convolution (voigt) functions in the context of peak fitting x-ray photoelectron spectroscopy (xps) narrow scans. *Applied Surface Science*, 447:548 – 553, 2018.
- [67] L. Jansson, V. Kumar, L. A. Ledebø, and K. Nideborn. A sensitive and inexpensive signal analyser for deep level studies. *Journal of Physics E: Scientific Instruments*, 14(4):464, 1981.
- [68] E. Janzén, R. Stedman, G. Grossmann, and H. G. Grimmeiss. High-resolution studies of sulfur- and selenium-related donor centers in silicon. *Phys. Rev. B*, 29:1907–1918, Feb 1984.
- [69] M. Jaros. A case for large auger recombination cross sections associated with deep centers in semiconductors. *Solid State Communications*, 25(12):1071 – 1074, 1978.
- [70] C. E. Jones, D. Schafer, W. Scott, and R. J. Hager. Carbon acceptor pair centers (x centers) in silicon. *Journal of Applied Physics*, 52(8):5148–5158, 1981.
- [71] A.A. Kal’fa and Sh.M. Kogan. Linewidth of impurity optical absorption in strongly compensated semiconductors. *Soviet Physics Semiconductors*, 6(1839), 1973.
- [72] D. Karaiskaj, G. Kirczenow, M. L. W. Thewalt, R. Buczko, and M. Cardona. Origin of the residual acceptor ground-state splitting in silicon. *Physical review letters*, 90(1), January 2003.
- [73] D. Karaiskaj, M. L. W. Thewalt, T. Ruf, M. Cardona, and M. Konuma. “intrinsic” acceptor ground state splitting in silicon: An isotopic effect. *Phys. Rev. Lett.*, 89:016401, Jun 2002.
- [74] D. Karaiskaj, M. L. W. Thewalt, T. Ruf, M. Cardona, H.-J. Pohl, G. G. Deviatych, P. G. Sennikov, and H. Riemann. Photoluminescence of isotopically purified silicon: How sharp are bound exciton transitions? *Phys. Rev. Lett.*, 86:6010–6013, Jun 2001.
- [75] J. K. Kauppinen, D. J. Moffatt, D. G. Cameron, and H. H. Mantsch. Noise in fourier self-deconvolution. *Appl. Opt.*, 20(10):1866–1879, May 1981.
- [76] Cheol-Seong Kim, Eiji Ohta, and Makoto Sakata. Electrical properties of selenium-diffused silicon. *Japanese Journal of Applied Physics*, 18(5):909, 1979.

- [77] Cheol-Seong Kim and Makoto Sakata. Diffusion coefficient of selenium in silicon by sheet hall coefficient measurements. *Japanese Journal of Applied Physics*, 18(2):247, 1979.
- [78] G. Kirczenow. A new model for bound multiexciton complexes. *Solid State Communications*, 21(8):713 – 715, 1977.
- [79] M. Kleverman, K. Bergman, and H. G. Grimmeiss. Photothermal investigations of magnesium-related donors in silicon. *Semiconductor Science and Technology*, 1(1):49, 1986.
- [80] M. Kleverman, H. G. Grimmeiss, A. Litwin, and E. Janzén. Capture processes at double donors in silicon. *Phys. Rev. B*, 31:3659–3666, Mar 1985.
- [81] W. Kohn and J. M. Luttinger. Theory of donor states in silicon. *Phys. Rev.*, 98:915–922, May 1955.
- [82] L. D. Landau and E. M. Lifshitz. Chapter x - the atom. In L.D. Landau and E.M. Lifshitz, editors, *Quantum Mechanics (Third Edition)*, pages 249 – 297. Pergamon, third edition edition, 1977.
- [83] D. M. Larsen. Inhomogeneous line broadening in donor magneto-optical spectra. *Phys. Rev. B*, 8:535–552, Jul 1973.
- [84] D. M. Larsen. Inhomogeneous broadening of the lyman-series absorption of simple hydrogenic donors. *Phys. Rev. B*, 13:1681–1691, Feb 1976.
- [85] M. Lax. Cascade capture of electrons in solids. *Phys. Rev.*, 119:1502–1523, Sep 1960.
- [86] A. L. Lin. Electrical and optical properties of magnesium diffused silicon. *Journal of Applied Physics*, 53(10):6989–6995, 1982.
- [87] H. J. Mattausch, W. Hanke, and G. Strinati. Impurities in covalent crystals: Exchange-correlation and local-field effects. *Phys. Rev. B*, 27:3735–3747, Mar 1983.
- [88] L. Mertz. Auxiliary computation for fourier spectrometry. *Infrared Physics*, 7(1):17 – 23, 1967.
- [89] N. S. Minaev, A. V. Mudryi, and V. D. Tkachev. Radiative recombination at thermal defects in silicon. *Soviet Physics Semiconductors*, 13(233), 1979.
- [90] Jane van W. Morgan and Thomas N. Morgan. Stress effects on excitons bound to axially symmetric defects in semiconductors. *Phys. Rev. B*, 1:739–749, Jan 1970.
- [91] K. J. Morse, R. J. S. Abraham, A. DeAbreu, C. Bowness, T. S. Richards, H. Riemann, N. V. Abrosimov, P. Becker, H.-J. Pohl, M. L. W. Thewalt, and S. Simmons. A photonic platform for donor spin qubits in silicon. *Science Advances*, 3(7), 2017.
- [92] K. J. Morse, P. Dluhy, J. Huber, J. Z. Salvail, K. Saeedi, H. Riemann, N. V. Abrosimov, P. Becker, H.-J. Pohl, S. Simmons, and M. L. W. Thewalt. Zero-field optical magnetic resonance study of phosphorus donors in 28-silicon. *Phys. Rev. B*, 97:115205, Mar 2018.

- [93] M. Nakamura and S. Murakami. Deep-level transient spectroscopy and photoluminescence studies of formation and depth profiles of copper centers in silicon crystals diffused with dilute copper. *Japanese Journal of Applied Physics*, 49(7R):071302, 2010.
- [94] M. Nakamura and S. Murakami. Depth progression of dissociation reaction of the 1.014-eV photoluminescence copper center in copper-diffused silicon crystal measured by deep-level transient spectroscopy. *Applied Physics Letters*, 98(14):141909, 2011.
- [95] M. Nakamura, S. Murakami, N. J. Kawai, S. Saito, K. Matsukawa, and H. Arie. Compositional transformation between Cu centers by annealing in Cu-diffused silicon crystals studied with deep-level transient spectroscopy and photoluminescence. *Japanese Journal of Applied Physics*, 48(8R):082302, 2009.
- [96] D. F. Nelson, J. D. Cuthbert, P. J. Dean, and D. G. Thomas. Auger recombination of excitons bound to neutral donors in gallium phosphide and silicon. *Phys. Rev. Lett.*, 17:1262–1265, Dec 1966.
- [97] G. F. Neumark. Auger theory at defects - application to states with two bound particles in gap. *Phys. Rev. B*, 7:3802–3810, Apr 1973.
- [98] Kyoji Nishikawa and Robert Barrie. Phonon broadening of impurity spectral lines: I. general theory. *Canadian Journal of Physics*, 41(7):1135–1173, 1963.
- [99] B. Pajot, J. Kauppinen, and R. Anttila. High resolution study of the group V impurities absorption in silicon. *Solid State Communications*, 31(10):759 – 763, 1979.
- [100] B. Pajot, G. Taravella, and J. P. Bouchaud. Use of Mg diffusion in p-type Si to measure the residual p concentration by infrared absorption. *Applied Physics Letters*, 23(4):189–191, 1973.
- [101] Bernard Pajot. *Optical Absorption of Impurities and Defects in Semiconducting Crystals*. Springer Series in Solid-State Sciences, 158. 2010.
- [102] R. Passler. Comparison of different analytical descriptions of the temperature dependence of the indirect energy gap in silicon. *Solid-State Electronics*, 39(9):1311 – 1319, 1996.
- [103] S. G. Pavlov, N. Deßmann, A. Pohl, V. B. Shuman, L. M. Portsel, A. N. Lodygin, Yu. A. Astrov, S. Winnerl, H. Schneider, N. Stavrias, A. F. G. van der Meer, V. V. Tsyplenkov, K. A. Kovalevsky, R. Kh. Zhukavin, V. N. Shastin, N. V. Abrosimov, and H.-W. Hübers. Dynamics of nonequilibrium electrons on neutral center states of interstitial magnesium donors in silicon. *Phys. Rev. B*, 94:075208, Aug 2016.
- [104] C. D. Porter and D. B. Tanner. Correction of phase errors in Fourier spectroscopy. *International Journal of Infrared and Millimeter Waves*, 4(2):273–298, Mar 1983.
- [105] A. K. Ramdas and S. Rodriguez. Spectroscopy of the solid-state analogues of the hydrogen atom: donors and acceptors in semiconductors. *Reports on Progress in Physics*, 44(12):1297, 1981.

- [106] F. A. Riddoch and M. Jaros. Auger recombination cross section associated with deep traps in semiconductors. *Journal of Physics C: Solid State Physics*, 13(33):6181, 1980.
- [107] J.B. Robertson and R.K. Franks. Beryllium as an acceptor in silicon. *Solid State Communications*, 6(11):825 – 826, 1968.
- [108] S. Rodriguez, P. Fisher, and F. Barra. Spectroscopic study of the symmetries and deformation-potential constants of singly ionized zinc in germanium. theory. *Phys. Rev. B*, 5:2219–2233, Mar 1972.
- [109] F. M. Ryan and R. C. Miller. Photoluminescence and pair spectrum in boron phosphide. *Phys. Rev.*, 148:858–862, Aug 1966.
- [110] A. N. Safonov, G. Davies, and E. C. Lightowers. Line shape of the no-phonon luminescence of excitons bound to phosphorus in carbon-doped silicon. *Phys. Rev. B*, 54:4409–4412, Aug 1996.
- [111] K. L. Shaklee and R. E. Nahory. Valley-orbit splitting of free excitons? the absorption edge of si. *Phys. Rev. Lett.*, 24:942–945, Apr 1970.
- [112] K Shirai, H Yamaguchi, A Yanase, and H Katayama-Yoshida. A new structure of cu complex in si and its photoluminescence. *Journal of Physics: Condensed Matter*, 21(6):064249, 2009.
- [113] V. B. Shuman, Yu. A. Astrov, A. N. Lodygin, and L. M. Portsel. High-temperature diffusion of magnesium in dislocation-free silicon. *Semiconductors*, 51(8):1031–1033, Aug 2017.
- [114] V. B. Shuman, A. A. Lavrent’ev, Yu. A. Astrov, A. N. Lodygin, and L. M. Portsel. Diffusion of interstitial magnesium in dislocation-free silicon. *Semiconductors*, 51(1):1–3, Jan 2017.
- [115] Aaron L. Stancik and Eric B. Brauns. A simple asymmetric lineshape for fitting infrared absorption spectra. *Vibrational Spectroscopy*, 47(1):66 – 69, 2008.
- [116] M. Steger, A. Yang, D. Karaiskaj, M. L. W. Thewalt, E. E. Haller, J. W. Ager, M. Cardona, H. Riemann, N. V. Abrosimov, A. V. Gusev, A. D. Bulanov, A. K. Kaliteevskii, O. N. Godisov, P. Becker, H.-J. Pohl, and K. M. Itoh. Shallow impurity absorption spectroscopy in isotopically enriched silicon. *AIP Conference Proceedings*, 893(1):231–232, 2007.
- [117] M. Steger, A. Yang, T. Sekiguchi, K. Saeedi, M. L. W. Thewalt, M. O. Henry, K. Johnston, H. Riemann, N. V. Abrosimov, M. F. Churbanov, A. V. Gusev, A. K. Kaliteevskii, O. N. Godisov, P. Becker, and H.-J. Pohl. Photoluminescence of deep defects involving transition metals in si: New insights from highly enriched  $^{28}\text{Si}$ . *Journal of Applied Physics*, 110(8):081301, 2011.
- [118] M. Steger, A. Yang, N. Stavrias, M. L. W. Thewalt, H. Riemann, N. V. Abrosimov, M. F. Churbanov, A. V. Gusev, A. D. Bulanov, I. D. Kovalev, A. K. Kaliteevskii, O. N. Godisov, P. Becker, and H.-J. Pohl. Reduction of the linewidths of deep luminescence centers in  $^{28}\text{Si}$  reveals fingerprints of the isotope constituents. *Phys. Rev. Lett.*, 100:177402, Apr 2008.

- [119] M. Steger, A. Yang, M. L. W. Thewalt, M. Cardona, H. Riemann, N. V. Abrosimov, M. F. Churbanov, A. V. Gusev, A. D. Bulanov, I. D. Kovalev, A. K. Kaliteevskii, O. N. Godisov, P. Becker, H.-J. Pohl, E. E. Haller, and J. W. Ager. High-resolution absorption spectroscopy of the deep impurities s and se in  $^{28}\text{Si}$  revealing the  $^{77}\text{Se}$  hyperfine splitting. *Phys. Rev. B*, 80:115204, Sep 2009.
- [120] E. A. Steinman and H. G. Grimmeiss. Magnesium-related luminescence in silicon. *Semiconductor Science and Technology*, 13(3):329, 1998.
- [121] A. M. Stoneham. Shapes of inhomogeneously broadened resonance lines in solids. *Rev. Mod. Phys.*, 41:82–108, Jan 1969.
- [122] J.C. Swartz, D.H. Lemmon, and R.N. Thomas. Optical excitation spectra of selenium-doped silicon. *Solid State Communications*, 36(4):331 – 334, 1980.
- [123] T. Taguchi, J. Shirafuji, and Y. Inuishi. Edge and donor-acceptor pair emissions in cadmium telluride. *Japanese Journal of Applied Physics*, 12(10):1558, 1973.
- [124] Michio Tajima, Takaaki Iwai, Hiroyuki Toyota, Simona Binetti, and Daniel Macdonald. Fine structure due to donor acceptor pair luminescence in compensated si. *Applied Physics Express*, 3(7):071301, 2010.
- [125] Y. Takano and M. Malei. *Semiconductor Silicon 1973*. 1973.
- [126] E. Tarnow, S. B. Zhang, K. J. Chang, and D. J. Chadi. Theory of be-induced defects in si. *Phys. Rev. B*, 42:11252–11260, Dec 1990.
- [127] M. L. W. Thewalt, G. Kirczenow, R. R. Parsons, and R. Barrie. Phonon broadening of bound exciton luminescence in silicon. *Canadian Journal of Physics*, 54(16):1728–1740, 1976.
- [128] M.L.W. Thewalt, M. Steger, A. Yang, N. Stavrias, M. Cardona, H. Riemann, N.V. Abrosimov, M.F. Churbanov, A.V. Gusev, A.D. Bulanov, I.D. Kovalev, A.K. Kaliteevskii, O.N. Godisov, P. Becker, H.-J. Pohl, J.W. Ager, and E.E. Haller. Can highly enriched  $^{28}\text{Si}$  reveal new things about old defects? *Physica B: Condensed Matter*, 401-402:587 – 592, 2007.
- [129] A. Thilderkvist, M. Kleverman, and H. G. Grimmeiss. Interstitial magnesium double donor in silicon. *Phys. Rev. B*, 49:16338–16348, Jun 1994.
- [130] Michael Tinkham. *Group theory and quantum mechanics*. N.Y. : McGraw-Hill, 1964. Includes bibliographies.
- [131] Dragica Vasileska. Empirical pseudopotential method: Theory and implementation, May 2010.
- [132] M A Vouk and E C Lightowlers. Two-phonon assisted free exciton recombination radiation from intrinsic silicon. *Journal of Physics C: Solid State Physics*, 10(18):3689, 1977.
- [133] Schmid W. Auger lifetimes for excitons bound to neutral donors and acceptors in si. *physica status solidi (b)*, 84(2):529–540.

- [134] G. D. Watkins and F. S. Ham. Electron paramagnetic resonance studies of a system with orbital degeneracy: The lithium donor in silicon. *Phys. Rev. B*, 1:4071–4098, May 1970.
- [135] J. Weber, H. Bauch, and R. Sauer. Optical properties of copper in silicon: Excitons bound to isoelectronic copper pairs. *Phys. Rev. B*, 25:7688–7699, Jun 1982.
- [136] H. Weiler, N. Meskini, W. Hanke, and M. Altarelli. Binding energies of substitutional and interstitial donors in si: Many-electron effects. *Phys. Rev. B*, 30:2266–2269, Aug 1984.
- [137] K. Weiser. Theory of diffusion and equilibrium position of interstitial impurities in the diamond lattice. *Phys. Rev.*, 126:1427–1436, May 1962.
- [138] J. D. Wiley and J. A. Seman. The enumeration of neighbors on cubic and hexagonal-based lattices. *The Bell System Technical Journal*, 49(3):355–378, March 1970.
- [139] A. Yang, M. Steger, T. Sekiguchi, D. Karauskaj, M. L. W. Thewalt, M. Cardona, K. M. Itoh, H. Riemann, N. V. Abrosimov, M. F. Churbanov, A. V. Gusev, A. D. Bulanov, I. D. Kovalev, A. K. Kaliteevskii, O. N. Godisov, P. Becker, H.-J. Pohl, J. W. Ager, and E. E. Haller. Single-frequency laser spectroscopy of the boron bound exciton in  $^{28}\text{Si}$ . *Phys. Rev. B*, 80:195203, Nov 2009.
- [140] O. Zelaya-Angel, M. Garcia-Rocha, J. G. Mendoza-Alvarez, M. Cardenas, and J. Aguilar-Hernandez. Donor acceptor pair photoluminescence spectra analysis in cdte:ag. *Journal of Applied Physics*, 94(4):2284–2288, 2003.
- [141] U. O. Ziemelis and R. R. Parsons. Sharp line donor acceptor pair luminescence in silicon. *Canadian Journal of Physics*, 59(6):784–801, 1981.

# Appendix A

## Relevant group theory

### A.1 Background

As detailed in the results section, below the known  $\text{Mg}_i^+$  and  $\text{Mg}_i^0$  lines we observe the  $2p_0$  and  $2p_{\pm}$  states of a center visible in both high and low boron content samples. We believe this to be a perturbed magnesium center with symmetry lower than the regular  $T_d$  of the lattice. This suggested two possibilities, either an alternate interstitial site, as that discussed by Baxter and Ascarelli [15], or a complex magnesium forms with some other defect. The results of an anneal/quench procedure ultimately suggested the latter is more likely.

The  $2p_{\pm}$  transition of  $\text{Mg}_i^+$  reveals a doublet while  $2p_{\pm}$  in  $\text{Mg}_{i^*}^+$  shows an unresolved quartet. Splitting of  $p_{\pm}$  states into doublets in the un-perturbed centers has been suggested to arise from some non-zero wavefunction overlap of those states with the central cell potential. The additional fine structure in the perturbed species can potentially be understood in group theory terms by considering a symmetry that is a subgroup of  $T_d$ . For instance, another interstitial site known to exist in silicon belongs to the  $C_{3v}$  point group. The character tables describing the symmetries of  $T_d$  and  $C_{3v}$  are included in Tabs. A.1 and A.2.

$T_d$	E	$8C_3$	$3C_2$	$6\sigma_d$	$6S_4$	
$A_1$	1	1	1	1	1	$x^2+y^2+z^2$
$A_2$	1	1	1	-1	-1	
E	2	-1	2	0	0	$(2z^2-x^2-y^2, x^2-y^2)$
$T_1$	3	0	-1	-1	1	$(R_x, R_y, R_z)$
$T_2$	3	0	-1	1	-1	$(x, y, z)$ <span style="margin-left: 2em;"><math>(xy, xz, yz)</math></span>

Table A.1: Character table for  $T_d$  (tetrahedral) symmetry group. This is the symmetry seen by all substitutional impurities in silicon and by many interstitials.

The top row labels are called the ‘classes’ of the symmetry group and indicate the symmetry operations that occur in each point group. The label ‘E’ represents the identity,  $C_n$  rotations through  $2\pi/n$  and  $\sigma_v$  reflections in a ‘vertical’ plane, i.e. one passing through the axis of highest symmetry.  $\sigma_d$  are reflections in a ‘diagonal’ plane, i.e. one containing the axis of highest symmetry bisecting the angle between the twofold axes perpendicular to the

$C_{3v}$	E	$2C_3$	$3\sigma_v$		
A <sub>1</sub>	1	1	1	$z$	$x^2+y^2, z^2$
A <sub>2</sub>	1	1	-1	$R_z$	
E	2	-1	0	$(x, y)$ $(R_x, R_y)$	$(x^2-y^2, xy)$ $(xz, yz)$

Table A.2: Character table for  $C_{3v}$  symmetry group. In silicon one way to attain this symmetry would be to have a defect positioned in an interstitial site along the  $\langle 111 \rangle$  axis.

symmetry axis as discussed by Tinkham [130]. The label  $S_n$  corresponds to ‘improper’ rotations, meaning a rotation through  $2\pi/n$  and a reflection in a plane perpendicular to the axis of rotation. The vertical labels are called the ‘irreducible representations’ of the group, where the criterion for reducibility is the capacity to reduce a matrix of all elements of the group to the same block form with the same similarity transformation. The entries in these tables, called ‘characters’ are the traces of the matrix representations of group elements. The final column in each table lists coordinates and rotations to indicate which irreducible representation they transform as. Arguably the most important relation when discussing point groups is the so-called ‘great orthogonality relation’, which for the full set of irreducible, unitary, and unique representations of a group is stated as [130],

$$\sum_R \chi^{(i)}(R)_{\mu\nu}^* \chi^{(j)}(R)_{\alpha\beta} = \frac{h}{l_i} \delta_{ij} \delta_{\mu\alpha} \delta_{\nu\beta}, \quad (\text{A.1})$$

here the summation runs over all irreducible representations of the group. From this there are five useful properties to keep in mind when working with and manipulating character tables.

1. The number of rows irreducible representations is equal to the number of classes.
2. The characters belonging to the same class are equal.
3. The sum of the squares of the dimensions of the irreducible representations is equal to the order of the group.
4. The sum of the squares of the characters in any irreducible representations is equal to the order of the group.
5. Those vectors whose components are the characters of two different irreducible representations are orthogonal.

To determine how the degeneracy of levels in the unperturbed group ( $T_d$ ) is lifted on moving to a subgroup with lower symmetry, such as  $C_{3v}$ , we begin by writing down the part of the character table of  $T_d$  that refers to the operations of its  $C_{3v}$  subgroup. In particular, to better understand the  $p_{\pm}$  level splitting, we are interested in how the triplet levels split. Thus we have,

$T_d$	E	$C_3$	$C_3^2$	$\sigma_v$	$\sigma'_v$	$\sigma''_v$	
$T_1$	3	0	0	-1	-1	-1	$(R_x, R_y, R_z)$
$T_2$	3	0	0	1	1	1	$(x, y, z)$ $(xy, xz, yz)$

Table A.3: Subset of the character table for  $T_d$  symmetry group corresponding to those symmetry operations that are found in  $C_{3v}$ .

Here we have written out all symmetry operations of the group, including those with the same characters in a given class. Now we may apply a decomposition relation between this and the corresponding characters of  $C_{3v}$  to determine the number of times a given representation will appear in the degeneracy lifted levels of each triplet state. If we group together elements of each class that have the same character  $\chi(R)$ , this is given according to,

$$a_j = \frac{1}{h} \sum_k N_k \chi^{(j)}(C_k)^* \chi(C_k). \quad (\text{A.2})$$

Here  $h$  is the order of the group given by the sum of the squares of the dimensionalities of the irreducible representations,  $N_k$  the number of elements in a class  $C_k$  and  $\chi(C_k)$  the characters of the representations. For example when looking for the contribution of  $E$ ,  $A_1$  and  $A_2$  to the  $T_2$  triplet we find:

$$\begin{aligned}
a_E &= \frac{1}{6}(3(2) + 0(-1) + 0(-1) + 1(0) + 1(0) + 1(0)) = 1 \\
a_{A_1} &= \frac{1}{6}(1(3) + 0(1) + 0(1) + 1(-1) + 1(-1) + 1(-1)) = 1 \\
a_{A_2} &= \frac{1}{6}(1(3) + 0(-1) + 0(-1) + 1(-1) + 1(-1) + 1(-1)) = 0.
\end{aligned} \quad (\text{A.3})$$

This means that the  $T_2$  level will be comprised of one doubly degenerate level ( $E$ ) and a singlet ( $A_1$ ) on moving to  $C_{3v}$ . Following the same procedure for the  $T_1$  triplet, we find that  $T_1$  and  $T_2$  split as  $T_1 = A_2 + E$  and  $T_2 = A_1 + E$  under a  $C_{3v}$  perturbation. From here we may apply the findings of Kohn and Luttinger seen in Tab. A.4, who have previously determined the reducible representations for donor levels in silicon ( $T_d$  symmetry). These are written as [81],

$ m $	E	$8C_3$	$3C_2$	$6\sigma_d$	$6S_4$
0	6	0	2	2	0
even, $\neq 0$	12	0	4	0	0
odd	12	0	-4	0	0

Table A.4: Character table for reducible representations of the  $T_d$  symmetry group for different values of magnetic quantum number  $m$ .

Here as usual the characters are related to traces of the matrix forms of symmetry operators of the group. However in this case the characters of these *reducible* representations are sums of traces of matrix representations (i.e. characters) of the *irreducible* representations of which they are comprised. The first row, for instance gives us the familiar splitting of the ‘1s’ valley-orbit states, i.e.  $A_1 + E + T_2$  by use of the decomposition relation and/or direct comparison with the table of irreducible  $T_d$  representations. By the same process we see that the last row,  $m = \text{odd}$ , i.e. for the  $p_{\pm}$  transitions will have the representation  $2T_1 + 2T_2$ . The further splitting of  $T_1$  and  $T_2$  having been determined above by looking at a  $C_{3v}$  perturbation, it now remains to determine which transitions are dipole allowed. Allowed transitions will be those for which the matrix element  $\int \Psi_i \hat{O} \Psi_j \neq 0$ . Where  $\Psi_i$  and  $\Psi_j$  are the initial and final states of a transition and the operator  $\hat{O}$  is the electric dipole operator given as:  $\mu = \sum_i e_i x_i + \sum_i e_i y_i + \sum_i e_i z_i$ . With  $e_i$  the charge on the  $i$ -th particle and  $x_i, y_i, z_i$  its coordinates. Thus the electric dipole operator belongs to representations which transform as the translations  $x, y, z$ . By looking at the product of symmetry representations corresponding to the product of wavefunctions  $\Psi_i$  and  $\Psi_j$  and the operator  $\hat{O}$  we may determine which are dipole allowed. If the result of the product contains  $A_1$ , i.e. the totally symmetric representation, some part of the matrix element integral must be non-zero. We note that this says nothing about how large the matrix element is, which is to say, how strongly allowed.

It is first instructive to look at a product table for the  $T_d$  point group to see what it says about transitions with the symmetry of  $p_{\pm}$  in the regular tetrahedral site. Here as mentioned previously we have the reducible representation  $2T_1 + 2T_2$ . Our initial state has representation  $A_1$  and in our final state we look at  $T_1$  or  $T_2$ . The dipole operator transforms as  $T_2$  ( $x, y, z$  symmetry). So we have:

$T_d$	$A_1$	$A_2$	$E$	$T_1$	$T_2$
$A_1$	$A_1$	$A_2$	$E$	$T_1$	$T_2$
$A_2$	$A_2$	$A_1$	$E$	$T_2$	$T_1$
$E$	$E$	$E$	$A_1+A_2+E$	$T_1+T_2$	$T_1+T_2$
$T_1$	$T_1$	$T_2$	$T_1+T_2$	$A_1+E+T_1+T_2$	$A_2+E+T_1+T_2$
$T_2$	$T_2$	$T_1$	$T_1+T_2$	$A_2+E+T_1+T_2$	$A_1+E+T_1+T_2$

Table A.5: Multiplication table showing products of the irreducible representations of the  $T_d$  symmetry group.

1.  $\Gamma_{A_1} \otimes \Gamma_{T_2} \otimes \Gamma_{T_1} = A_2 + E + T_1 + T_2$
2.  $\Gamma_{A_1} \otimes \Gamma_{T_2} \otimes \Gamma_{T_2} = A_1 + E + T_1 + T_2$

This indicates that of the available levels in  $2T_1 + 2T_2$  only the two degenerate triplet transitions  $2T_2$  are allowed. The doublets seen for many  $p_{\pm}$  levels in Mg and other donors, are consistent with degeneracy between these two triplet levels being lifted by some non-zero wavefunction overlap with the central cell potential.

Now we follow the same analysis for the  $T_d$  subgroup  $C_{3v}$ . Again the initial state has symmetry  $A_1$  and for our final state we wish to see which levels among  $A_1, A_2$  and  $E$  will

be allowed. Under  $C_{3v}$  symmetry, the dipole operator goes as  $A_1 + E$ , with  $A_1$  transforming as  $z$ , and  $E$  as  $x$  and  $y$ . From this we find the following:

$C_{3v}$	$A_1$	$A_2$	$E$
$A_1$	$A_1$	$A_2$	$E$
$A_2$	$A_2$	$A_1$	$E$
$E$	$E$	$E$	$A_1+A_2+E$

Table A.6: Multiplication table showing products of the irreducible representations of the  $C_{3v}$  symmetry group.

1.  $\Gamma_{A_1} \otimes \Gamma_{A_1+E} \otimes \Gamma_{A_1} = A_1 + E$
2.  $\Gamma_{A_1} \otimes \Gamma_{A_1+E} \otimes \Gamma_{A_2} = A_2 + E$
3.  $\Gamma_{A_1} \otimes \Gamma_{A_1+E} \otimes \Gamma_E = 2A_1 + A_2 + E$

This indicates that transitions to states with  $A_1$  and/or  $E$  symmetry are both allowed, while those with  $A_2$  are forbidden. In this case, from the previously discussed splitting  $2(A_1 + E) + 2(A_2 + E)$  we are left with  $2(A_1 + E) + 2(E)$ . This indicates three allowed transitions (note that the doublets  $E$  in separate bracketed terms are not necessarily degenerate). The fine structure we observe in the  $2p_{\pm}$  transition of  $Mg_{i*}^+$  may be accounted for by degeneracy being lifted between the doublets and singlets via wavefunction overlap with the central cell potential. This implies a total of six possible peaks, of which we observe up to four. This does not conclusively tell us that  $C_{3v}$  is the symmetry of the perturbed center, but it does offer enough extra splitting to be consistent with the observed fine structure.

## A.2 Matrix representations

It can be helpful to write the symmetry operators of a point group as matrices  $\Gamma(R)$  for each symmetry element  $R$ . The characters of a point group are given as the traces these matrix representations according to,

$$\chi^{(j)}(R) = Tr(\Gamma^{(j)}(R)). \quad (A.4)$$

To see this for  $C_{3v}$  for example, which governs the symmetry of the equilateral triangle, we begin by considering such a geometry where we label indices  $a, b, c$ , and  $d$  as the vertices and center of the triangle. The transformation properties of the  $C_{3v}$  group transform those indices as seen in A.5,

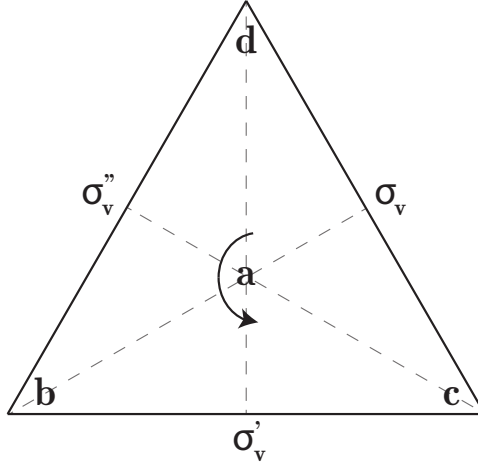


Figure A.1: Here we show an equilateral triangle with labelled vertices and center a-d. Planes of reflection  $\sigma_v$ ,  $\sigma'_v$ , and  $\sigma''_v$  are indicated as dashed lines passing through the three main symmetry axes.

$$\begin{aligned}
 (E) &\rightarrow (a, b, c, d) \begin{pmatrix} 1 & 0 & 0 & 0 \\ 0 & 1 & 0 & 0 \\ 0 & 0 & 1 & 0 \\ 0 & 0 & 0 & 1 \end{pmatrix} = (a, b, c, d) \\
 (C_3) &\rightarrow (a, b, c, d) \begin{pmatrix} 1 & 0 & 0 & 0 \\ 0 & 0 & 0 & 1 \\ 0 & 1 & 0 & 0 \\ 0 & 0 & 1 & 0 \end{pmatrix} = (a, c, d, b) \\
 (C_3^2) &\rightarrow (a, b, c, d) \begin{pmatrix} 1 & 0 & 0 & 0 \\ 0 & 0 & 0 & 1 \\ 0 & 1 & 0 & 0 \\ 0 & 0 & 1 & 0 \end{pmatrix} = (a, d, b, c) \\
 (\sigma_v) &\rightarrow (a, b, c, d) \begin{pmatrix} 1 & 0 & 0 & 0 \\ 0 & 1 & 0 & 0 \\ 0 & 0 & 0 & 1 \\ 0 & 0 & 1 & 0 \end{pmatrix} = (a, b, d, c) \\
 (\sigma'_v) &\rightarrow (a, b, c, d) \begin{pmatrix} 1 & 0 & 0 & 0 \\ 0 & 0 & 1 & 0 \\ 0 & 1 & 0 & 0 \\ 0 & 0 & 0 & 1 \end{pmatrix} = (a, c, b, d) \\
 (\sigma''_v) &\rightarrow (a, b, c, d) \begin{pmatrix} 1 & 0 & 0 & 0 \\ 0 & 0 & 0 & 1 \\ 0 & 0 & 1 & 0 \\ 0 & 1 & 0 & 0 \end{pmatrix} = (a, d, c, b)
 \end{aligned} \tag{A.5}$$

This is a set of block-diagonal matrices, one  $1 \times 1$  and a  $3 \times 3$ , such that  $\Gamma^{(4)}(R) = \Gamma^{(1)}(R) \oplus \Gamma^{(3)}(R)$ . The  $1 \times 1$  sub-matrices are all simply equal to 1 and so by default have the same block diagonal representation. The  $3 \times 3$  sub-matrices on the other hand do not all have the same block-diagonal form. This by definition means that they cannot form an irreducible representation. This is rectified by a new set of basis functions written as,

$$b' = \frac{1}{\sqrt{3}}(b + c + d) \quad c' = \frac{1}{\sqrt{3}}(2b - c - d) \quad d' = \frac{1}{\sqrt{2}}(c - d) \quad (\text{A.6})$$

This gives the overall transformation,

$$(b, c, d)M = (b', c', d'), \quad (\text{A.7})$$

with the transformation matrix  $M$  is given as  $M = \begin{pmatrix} 1/\sqrt{3} & 2/\sqrt{6} & 0 \\ 1/\sqrt{3} & -1/\sqrt{6} & 1/\sqrt{2} \\ 1/\sqrt{3} & -1/\sqrt{6} & -1/\sqrt{2} \end{pmatrix}$ . This transformation matrix can then be applied to give block diagonal matrices of the same form via the change of basis  $\Gamma'(R) = M^{-1}\Gamma(R)M$ . The block diagonal matrices for each of the symmetry operations of  $C_{3v}$  then become,

$$E : \begin{bmatrix} 1 & 0 & 0 \\ 0 & 1 & 0 \\ 0 & 0 & 1 \end{bmatrix} \quad C_3 : \begin{bmatrix} 1 & 0 & 0 \\ 0 & -1/2 & \sqrt{3}/2 \\ 0 & -\sqrt{3}/2 & -1/2 \end{bmatrix} \quad C_3^2 : \begin{bmatrix} 1 & 0 & 0 \\ 0 & -1/2 & -\sqrt{3}/2 \\ 0 & \sqrt{3}/2 & -1/2 \end{bmatrix}$$

$$\sigma_v : \begin{bmatrix} 1 & 0 & 0 \\ 0 & 1 & 0 \\ 0 & 0 & -1 \end{bmatrix} \quad \sigma'_v : \begin{bmatrix} 1 & 0 & 0 \\ 0 & -1/2 & \sqrt{3}/2 \\ 0 & \sqrt{3}/2 & 1/2 \end{bmatrix} \quad \sigma''_v : \begin{bmatrix} 1 & 0 & 0 \\ 0 & -1/2 & -\sqrt{3}/2 \\ 0 & -\sqrt{3}/2 & 1/2 \end{bmatrix}.$$

At this point we can see that all the matrices have the same block-diagonal form, with  $\Gamma^{(3)}(R) = \Gamma^{(1)}(R) \oplus \Gamma^{(2)}(R)$ . From the traces of these matrices we obtain the characters of the singlet  $A_1$  ( $1 \times 1$  block diagonal sub-matrices) and doublet E ( $2 \times 2$  block diagonal sub-matrices) as seen in the  $C_{3v}$  character table included above. The  $A_2$  representation can then be determined through the relations between rows and columns of the table discussed in the previous section. Likewise it can easily be verified that these matrices satisfy the multiplication table for the  $C_{3v}$  group included above.

### A.3 Dipole allowed/forbidden transitions in $T_d$

Here we show all dipole allowed and forbidden transitions from each symmetry element in the  $T_d$  group. For  $T_d$  we know that the dipole operator  $\hat{O}$  transforms with the symmetry of the x, y, z axes, which according to the character table for  $T_d$  corresponds to the  $T_2$  representation. For any given transition to be allowed we evaluate the product of symmetry

representations corresponding to each of  $\Psi_i$ ,  $\hat{O}$ , and  $\Psi_j$  in the integrand of  $\int \Psi_i \hat{O} \Psi_j$  and find:

### A.3.1 From $A_1$

1.  $\Gamma_{A_1} \otimes \Gamma_{T_2} \otimes \Gamma_{A_1} \rightarrow \text{no } A_1$
2.  $\Gamma_{A_1} \otimes \Gamma_{T_2} \otimes \Gamma_{A_2} \rightarrow \text{no } A_1$
3.  $\Gamma_{A_1} \otimes \Gamma_{T_2} \otimes \Gamma_E \rightarrow \text{no } A_1$
4.  $\Gamma_{A_1} \otimes \Gamma_{T_2} \otimes \Gamma_{T_1} \rightarrow \text{no } A_1$
5.  $\Gamma_{A_1} \otimes \Gamma_{T_2} \otimes \Gamma_{T_2} \rightarrow \text{contains } A_1$

### A.3.3 From $E$

1.  $\Gamma_E \otimes \Gamma_{T_2} \otimes \Gamma_{A_1} \rightarrow \text{no } A_1$
2.  $\Gamma_E \otimes \Gamma_{T_2} \otimes \Gamma_{A_2} \rightarrow \text{no } A_1$
3.  $\Gamma_E \otimes \Gamma_{T_2} \otimes \Gamma_E \rightarrow \text{no } A_1$
4.  $\Gamma_E \otimes \Gamma_{T_2} \otimes \Gamma_{T_1} \rightarrow \text{contains } A_1$
5.  $\Gamma_E \otimes \Gamma_{T_2} \otimes \Gamma_{T_2} \rightarrow \text{contains } A_1$

### A.3.5 From $T_2$

1.  $\Gamma_{T_2} \otimes \Gamma_{T_2} \otimes \Gamma_{A_1} \rightarrow \text{contains } A_1$
2.  $\Gamma_{T_2} \otimes \Gamma_{T_2} \otimes \Gamma_{A_2} \rightarrow \text{no } A_1$
3.  $\Gamma_{T_2} \otimes \Gamma_{T_2} \otimes \Gamma_E \rightarrow \text{contains } A_1$
4.  $\Gamma_{T_2} \otimes \Gamma_{T_2} \otimes \Gamma_{T_1} \rightarrow \text{contains } A_1$
5.  $\Gamma_{T_2} \otimes \Gamma_{T_2} \otimes \Gamma_{T_2} \rightarrow \text{contains } A_1$

### A.3.2 From $A_2$

1.  $\Gamma_{A_2} \otimes \Gamma_{T_2} \otimes \Gamma_{A_1} \rightarrow \text{no } A_1$
2.  $\Gamma_{A_2} \otimes \Gamma_{T_2} \otimes \Gamma_{A_2} \rightarrow \text{no } A_1$
3.  $\Gamma_{A_2} \otimes \Gamma_{T_2} \otimes \Gamma_E \rightarrow \text{no } A_1$
4.  $\Gamma_{A_2} \otimes \Gamma_{T_2} \otimes \Gamma_{T_1} \rightarrow \text{contains } A_1$
5.  $\Gamma_{A_2} \otimes \Gamma_{T_2} \otimes \Gamma_{T_2} \rightarrow \text{no } A_1$

### A.3.4 From $T_1$

1.  $\Gamma_{T_1} \otimes \Gamma_{T_2} \otimes \Gamma_{A_1} \rightarrow \text{no } A_1$
2.  $\Gamma_{T_1} \otimes \Gamma_{T_2} \otimes \Gamma_{A_2} \rightarrow \text{contains } A_1$
3.  $\Gamma_{T_2} \otimes \Gamma_{T_2} \otimes \Gamma_E \rightarrow \text{contains } A_1$
4.  $\Gamma_{T_1} \otimes \Gamma_{T_2} \otimes \Gamma_{T_1} \rightarrow \text{contains } A_1$
5.  $\Gamma_{T_1} \otimes \Gamma_{T_2} \otimes \Gamma_{T_2} \rightarrow \text{contains } A_1$

From this we see that from  $A_1$ , only transitions to  $T_2$  are dipole allowed, from  $A_2$  only transitions to  $T_1$ , and from  $E$  transitions to  $T_1$  and  $T_2$ . From  $T_1$  transitions to  $A_2$ ,  $E$ ,  $T_1$ , and  $T_2$  are allowed, and from  $T_2$  transitions to  $A_1$ ,  $E$ ,  $T_1$ , and  $T_2$  are allowed.

## A.4 Raman allowed/forbidden transitions in $\mathbf{T}_d$

As in absorption, we aim to evaluate the triple product of symmetry representations corresponding to the terms in  $\int \Psi_i \alpha \Psi_j$ . Here  $\alpha$  replaces the dipole moment vector  $\mu$  relevant to dipole allowed/forbidden transitions.  $\alpha$  is a  $3 \times 3$  tensor that represents polarizability. This is described as the ratio of induced dipole moment  $P$  to the electric field  $E$  that produces it, i.e.

$$\begin{bmatrix} P_x \\ P_y \\ P_z \end{bmatrix} = \begin{bmatrix} \alpha_{xx} & \alpha_{xy} & \alpha_{xz} \\ \alpha_{yx} & \alpha_{yy} & \alpha_{yz} \\ \alpha_{zx} & \alpha_{zy} & \alpha_{zz} \end{bmatrix} \begin{bmatrix} E_x \\ E_y \\ E_z \end{bmatrix} \quad (\text{A.8})$$

For Raman transitions  $\alpha_{ij} = \alpha_{ji}$  so there are six components of the nine possible that need to be considered. These components are  $\alpha_{xx}$ ,  $\alpha_{yy}$ ,  $\alpha_{zz}$ ,  $\alpha_{xy} = \alpha_{yx}$ ,  $\alpha_{yz} = \alpha_{zy}$  and  $\alpha_{xz} = \alpha_{zx}$ . The symmetries of these elements are the same as the product functions  $xx = x^2$ ,  $yy = y^2$ ,  $zz = z^2$ ,  $xy = yx$ ,  $yz = zy$  and  $xz = zx$ . For the  $T_d$  symmetry group this means that  $\alpha$  corresponds to the combination of irreducible representations  $\Gamma_\alpha = A_1 + E + T_2$ . Raman allowed and forbidden transitions from each symmetry element of  $T_d$  can then be represented as follows:

#### A.4.1 From $A_1$

1.  $\Gamma_{A_1} \otimes \Gamma_\alpha \otimes \Gamma_{A_1} \rightarrow$  contains  $A_1$
2.  $\Gamma_{A_1} \otimes \Gamma_\alpha \otimes \Gamma_{A_2} \rightarrow$  no  $A_1$
3.  $\Gamma_{A_1} \otimes \Gamma_\alpha \otimes \Gamma_E \rightarrow$  contains  $A_1$
4.  $\Gamma_{A_1} \otimes \Gamma_\alpha \otimes \Gamma_{T_1} \rightarrow$  no  $A_1$
5.  $\Gamma_{A_1} \otimes \Gamma_\alpha \otimes \Gamma_{T_2} \rightarrow$  contains  $A_1$

#### A.4.2 From $A_2$

1.  $\Gamma_{A_2} \otimes \Gamma_\alpha \otimes \Gamma_{A_1} \rightarrow$  no  $A_1$
2.  $\Gamma_{A_2} \otimes \Gamma_\alpha \otimes \Gamma_{A_2} \rightarrow$  contains  $A_1$
3.  $\Gamma_{A_2} \otimes \Gamma_\alpha \otimes \Gamma_E \rightarrow$  contains  $A_1$
4.  $\Gamma_{A_2} \otimes \Gamma_\alpha \otimes \Gamma_{T_1} \rightarrow$  contains  $A_1$
5.  $\Gamma_{A_2} \otimes \Gamma_\alpha \otimes \Gamma_{T_2} \rightarrow$  no  $A_1$

#### A.4.3 From $E$

1.  $\Gamma_E \otimes \Gamma_\alpha \otimes \Gamma_{A_1} \rightarrow$  contains  $A_1$
2.  $\Gamma_E \otimes \Gamma_\alpha \otimes \Gamma_{A_2} \rightarrow$  contains  $A_1$
3.  $\Gamma_E \otimes \Gamma_\alpha \otimes \Gamma_E \rightarrow$  contains  $A_1$
4.  $\Gamma_E \otimes \Gamma_\alpha \otimes \Gamma_{T_1} \rightarrow$  contains  $A_1$
5.  $\Gamma_E \otimes \Gamma_\alpha \otimes \Gamma_{T_2} \rightarrow$  contains  $A_1$

#### A.4.4 From $T_1$

1.  $\Gamma_{T_1} \otimes \Gamma_\alpha \otimes \Gamma_{A_1} \rightarrow$  no  $A_1$
2.  $\Gamma_{T_1} \otimes \Gamma_\alpha \otimes \Gamma_{A_2} \rightarrow$  no  $A_1$
3.  $\Gamma_{T_1} \otimes \Gamma_\alpha \otimes \Gamma_E \rightarrow$  contains  $A_1$
4.  $\Gamma_{T_1} \otimes \Gamma_\alpha \otimes \Gamma_{T_1} \rightarrow$  contains  $A_1$
5.  $\Gamma_{T_1} \otimes \Gamma_\alpha \otimes \Gamma_{T_2} \rightarrow$  contains  $A_1$

#### A.4.5 From $T_2$

1.  $\Gamma_{T_2} \otimes \Gamma_\alpha \otimes \Gamma_{A_1} \rightarrow$  no  $A_1$
2.  $\Gamma_{T_2} \otimes \Gamma_\alpha \otimes \Gamma_{A_2} \rightarrow$  no  $A_1$
3.  $\Gamma_{T_2} \otimes \Gamma_\alpha \otimes \Gamma_E \rightarrow$  contains  $A_1$
4.  $\Gamma_{T_2} \otimes \Gamma_\alpha \otimes \Gamma_{T_1} \rightarrow$  contains  $A_1$
5.  $\Gamma_{T_2} \otimes \Gamma_\alpha \otimes \Gamma_{T_2} \rightarrow$  contains  $A_1$

From this we see that from  $A_1$ , transitions to  $A_1$ ,  $E$ , and  $T_2$  are Raman allowed, from  $A_2$  transitions to  $A_2$ ,  $E$ , and  $T_1$ , and from  $E$  transitions to  $A_1$ ,  $A_2$ ,  $E$ ,  $T_1$ , and  $T_2$ . From  $T_1$

transitions to  $E$ ,  $T_1$ , and  $T_2$  are allowed, and from  $T_2$  transitions to  $A_1$ ,  $E$ ,  $T_1$ , and  $T_2$  are allowed.

## Appendix B

# Structure of hydrogenic orbitals

Donor spectra are of course only analogous, rather than precisely equivalent to the electronic levels of a hydrogen atom. It remains helpful however, when describing such phenomena as the splitting of  $p_{\pm}$  levels in donor spectra, to look for qualitative explanations in the structure of hydrogen atom wavefunctions. The structure of hydrogenic orbitals is well understood, with solutions separable into angular and radial components such that [41],

$$\Psi_{nlm} = R_{nl}(r)Y_{lm}(\theta, \phi). \quad (\text{B.1})$$

Here the radial component  $R_{nl}(r)$  is expressed as,

$$R_{nl}(r) = \sqrt{\left(\frac{2Z}{na_{\mu}}\right)^3 \frac{(n-l-1)!}{2n[(n+l)!]}} e^{-Zr/na_{\mu}} \left(\frac{2Zr}{na_{\mu}}\right)^l L_{n-l-1}^{2l+1}\left(\frac{2Zr}{na_{\mu}}\right), \quad (\text{B.2})$$

with principle, angular, and magnetic quantum numbers  $n$ ,  $l$  and  $m$ . Here  $L_{n-l-1}^{2l+1}$  are the associated Laguerre polynomials,  $Z$  is the nuclear charge, and  $a_{\mu} = m_e/\mu$  for electron mass  $m_e$  and reduced mass of the electron-nucleus  $\mu$ . The angular component  $Y_{lm}(\theta, \phi)$  are spherical harmonics given as,

$$Y_{lm}(\theta, \phi) = (-1)^m \sqrt{\frac{(2l+1)(l-m)!}{4\pi(l+m)!}} P_{lm}(\cos\theta) e^{im\phi}. \quad (\text{B.3})$$

Here  $P_{lm}$  are Legendre polynomials. It is instructive to examine the ground state and excited state behaviour near the origin in order to qualitatively understand the likelihood of overlap or lack thereof with the central cell.

As seen in Fig. B.1 it is clear that the ground state 1s will have a high degree of overlap with the central cell. The p-states, with examples shown for 2p and 3p levels in Fig. B.1, have a probability density that goes identically to zero at the origin. Since the central cell potential is not a point potential but has a volume associated with it, these states have some possibility of overlap, leading to the splitting we observe in many  $p_{\pm}$  transitions.

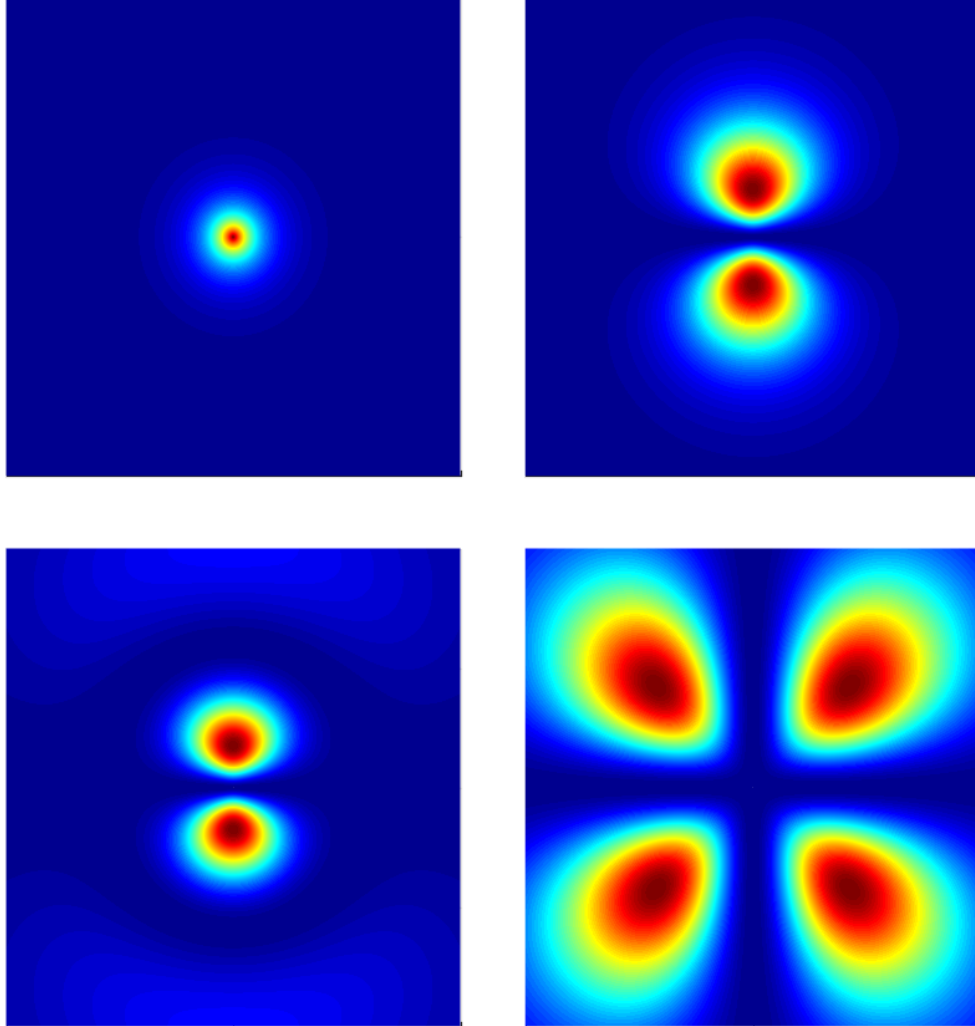


Figure B.1: Here we show 2D plots that display the square of the radial component of the hydrogen atom wavefunctions for a variety of energy levels. From top to bottom/left to right, these include the 1s ground state, as well as examples of 2p, 3p and 3d excited states.

Higher  $l$  states such as the d-levels, an example of which is seen for 3d in Fig. B.1, possess a larger near-zero region about the origin. This implies a lower probability for overlap with the central cell potential.

To see why we anticipate decreasing overlap with the central cell with increasing  $n$  for  $np_{\pm}$  transitions, it is instructive to examine the radial distribution functions displayed in Fig. B.2. These show the probability density across a spherical shell of radius  $r$ . From this it is clear that the probability of finding an electron near the nucleus decreases as we reach higher excited states. Behaviour near the origin remains qualitatively consistent albeit decreasing in magnitude. This leads to the steady decrease in splitting we observe in  $Mg_i^+$  for  $p_{\pm}$  transitions as high as  $6p_{\pm}$ , which has been attributed to central cell splitting in past investigations [129].

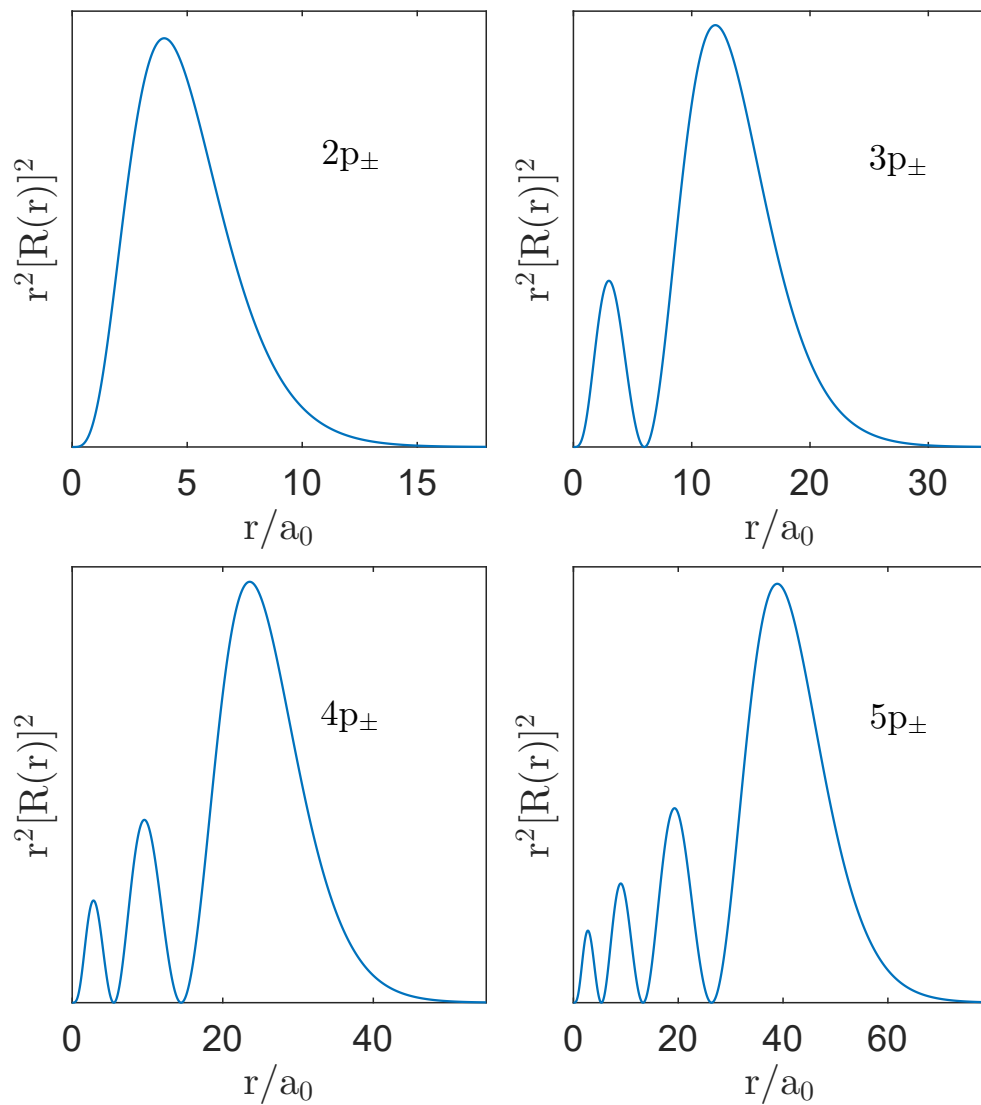


Figure B.2: Here we show plots of the radial distribution function for the hydrogenic levels  $2p_{\pm}$ ,  $3p_{\pm}$ ,  $4p_{\pm}$ , and  $5p_{\pm}$  which illustrate the steadily decreasing magnitude of the probability density near the origin.